Time Resolved Photoelectron Spectroscopy of Electron Accommodation Dynamics for Iodide-Thiouracil and Iodide-Thymine Clusters

By

Megan Patricia Asplund

A dissertation submitted in partial satisfaction of the

requirements for the degree of

Doctor of Philosophy

in

Chemistry

in the

Graduate Division

of the

University of California, Berkeley

Committee in charge:

Professor Daniel M. Neumark, Chair

Professor Holger Mueller

Professor Evan Williams

Spring 2024

Time Resolved Photoelectron Spectroscopy of Electron Accommodation Dynamics for Iodide-Thiouracil and Iodide-Thymine Clusters

Abstract

Time Resolved Photoelectron Spectroscopy of Electron Accommodation Dynamics

for Iodide-Thiouracil and Iodide-Thymine Clusters

By Megan Patricia Asplund

Doctor of Philosophy in Chemistry

University of California, Berkeley

Professor Daniel M. Neumark, Chair

Interactions between low energy electrons (LEEs) and biological chromophores are fundamental in many processes which take place in living organisms. UV irradiation of a cell, for example, can lead to LEE attachment to DNA and RNA, inducing single and double strand breakages. Transient nucleobase anions generated by electron attachment have been implicated as being key to damage mechanisms.

The process of LEE attachment to nucleobases may be modeled by time resolved photoelectron spectroscopy (TRPES) of a cluster containing the nucleobase of interest and an electron donor species. The iodide acts as a controllable source of LEEs when excited by a UV pulse. A UV or IR probe pulse can detach an excess electron from a transient anion or photofragment, tracing the dynamics of electron transfer and accommodation.

Small modifications to nucleobase structures can have a profound impact on electron dynamics. An excess electron can be accommodated as either a valence bound (VB) ion, in which a molecular valence orbital is populated, or a dipole bound (DB) ion, in which the electron is stabilized by interaction with the molecular dipole. Single atom replacements or addition of a methyl group can significantly change the binding energy associated with these anions. In this thesis, we employ TRPES to examine the electron dynamics for iodide-2-thiouracil (I^-·2TU), iodide-4-thiouracil (I^-·4TU), and iodide-thymine (I^-·T).

Thiobases like 2-thiouracil and 4-thiouracil have an increased reactivity compared to the canonical nucleobases, leading to their potential application as sensitizers for phototherapies. Their properties can also clarify fundamental principles of nucleobases photophysics. The thiouracils have larger dipolar moments than uracil, but no evidence for thiouracil DB ions has been observed by single photon photoelectron spectroscopy. TRPES measurements of the corresponding iodide clusters enable us to determine whether these ions are fundamentally unstable or simply short-lived. The singly substituted thiouracils also have VB ions with significantly different properties than the VB ions of uracil or thymine. Thiouracil VB ions have much higher binding energies, facilitating rapid and complete DB to VB interconversion. 2-thiouracil has a pair of nearly degenerate $\pi\pi^*$ transitions which other groups have associated with faster relaxation rates of the neutral species; 4-thiouracil has a particularly low energy $\pi\pi^*$ transition that is accessible below the I^-·4TU VDE. Their study can therefore give us significant insight into the properties that are

most important in electron accommodation of the canonical nucleobases by comparing changes in dynamics due to changes in these properties.

Excitation of I^-·2TU near its vertical detachment energy (VDE) gives rise to DB and VB ion signals, with the DB signal appearing and decaying on ultrafast timescales (within the instrument response time) and bi-exponential decay of the VB signal. At 4.73 eV excitation, no DB signal is seen, but two signals are attributed to distinct but energetically similar VB anions arising from the nearly degenerate $\pi\pi^*$ excitations. Utilizing a UV probe pulse, we find that the major decay product I^- appears quite rapidly. Rice–Ramsperger–Kassel–Marcus (RRKM) theory predicts a cluster dissociation time in reasonable agreement with the measured I^- rise time, indicating that iodide reforms rapidly by back electron transfer.

TRPES of I^-·4TU was performed with excitation energies below the cluster VDE and near the cluster VDE. We find that 3.88 eV excitation, which is resonant with a 4TU $\pi\pi^*$ transition but below the cluster VDE, facilitates the formation of valence bound anions without the mediation of a dipole bound state. This provides empirical evidence for a previously proposed mechanism wherein nucleobase localized excitation is key to VB ion formation. Near-VDE excitation of the cluster gives rise to DB and VB anion signal, with two distinct time regimes for VB anion formation. The first is ultra-fast formation associated with $\pi\pi^*$ excitation and the second is a slower rise corresponding to DB to VB interconversion.

Electron accommodation dynamics of I^-·T were previously measured with an IR (1.55 eV) probe energy. In light of results for the thiouracils, these dynamics with a UV proper energy merit analysis. The higher energy probe reveals an ion signal bound by 1–2 eV in addition to the canonical T VB ion. The VDE of this new ion signal is in reasonable agreement with the calculated VDE of a thymine tautomer anion. The UV probe pulse also enables us to measure the iodide dissociation time, which is found to be much slower than that of the other iodide nucleobase clusters we have measured but is similar to the decay time of the tautomer ion signal. This suggests that because the VB signal from the canonical tautomer of thymine is depleted rapidly and efficiently by electron autodetachment, reformation of iodide comes from decay of the thymine rare tautomer's VB anion. The rise of the tautomer anion signal gives an approximate tautomerization time constant of 8 ps.

Table of Contents

Abstract 1

Introduction ***1***

1.1 Overview 2
1.2 Motivation 2
1.3 Nucleobase Anions 3
1.4 TRPES of iodide-chromophore clusters 5
1.5 TRPES derivation 7
1.6 Dissociation and RRKM Modeling 10
1.7 Computational Methods 12
1.8 Systems Studied 13
I–·2-thiouracil 13
I⁻·4-thiouracil 13
I⁻·thymine 14

Experimental Methods ***18***

2.1 Overview 19
2.2 Cluster Formation and Optimization 19
2.2.1 Cluster Generation 19
2.2.2 Ion Packet Manipulation 21
2.2.3 Timing 22
2.3 Laser Pulse Generation and Manipulation 23
2.3.1 Oscillator 23
2.3.2 Stretcher 23
2.3.3 Pockels Cell 24
2.3.4 Amplifier 25
2.3.5 Compressor 26
2.3.6 Pulse Characterization 27
2.3.6 Generation of experimental laser energies 27
2.3.7 Cross-correlation 29
2.4 Electron Detection by Velocity Map Imaging 29

Electron transfer dynamics of iodide-2-thiouracil clusters ***33***

3.1 Abstract 34
3.2 Introduction 34
3.3 Methods 37
3.4 Results 37
3.4.1 TRPES with the 1.59-eV probe 38
3.4.2 TRPES with the 3.18-eV probe 39
3.5 Analysis 40
3.6 Discussion 44
3.6.1 Excitation at 4.16 eV 45
3.6.2 Excitation at 4.73 eV 46

3.6.3 Comparison with I^-·U 48
3.7 Conclusions 48
3.8 Supporting Information 49
3.8.1 Theoretical estimation of the rate constant of the iodide dissociation 49
3.8.2. Fitting results in 4.16 eV excitation under the convolved triple-exponential function 50
Electron Transfer Dynamics of Iodide-4-Thiouracil Cluster 54
4.1 Abstract 55
4.2 Introduction 55
4.3 Methods 57
4.4 Results 59
4.5 Analysis 61
4.6 Discussion 65
4.6.1 VB formation by 3.88 eV excitation 66
4.6.2 VB and DB dynamics with 4.16 eV excitation 66
4.6.3 Autodetachment dynamics 68
4.6.4 Decay products 68
4.7 Conclusion 70
UV Probe Measurements of Nucleobase Excited Iodide-Thymine Clusters 74
5.1 Abstract 75
5.2 Introduction 75
5.3 Methods 76
5.4 Results 77
5.5 Analysis 79
5.6 Discussion 82
5.7 Conclusion 85

Table of Figures

Introduction

Figure 1.1: Structures of uracil, 2-thiouracil, 4-thiouracil, and thymine 2
Figure 1.2: Valence bound and dipole bound anions of I^-·4-thiouracil 4
Figure 1.3: Schematic representing time-resolved photoelectron spectroscopy 6
Figure 1.4: Potential energy curve of I^-·2-thiouracil at set I–N1 distances 11

Experimental Methods

Figure 2.1: Schematic of the TRPES apparatus..... 20
Figure 2.2: Schematic of the triggering scheme 22
Figure 2.3: Schematic of the stretcher for the KM Dragon 24
Figure 2.4: Schematic of the muti-pass amplification ring of the KM Dragon 25
Figure 2.5: Schematic of the KM Dragon compressor 26
Figure 2.6: Schematic of the major beam lines of the TOPAS-C 28
Figure 2.7: Cross-correlation of 1.55 eV and 4.35 eV pulses by SFG intensity.....29
Figure 2.8: Schematic of the VMI apparatus and phosphor screen detector 30

Electron Transfer Dynamics of Iodide-2-thiouracil Clusters

Figure 3.1: Ground-state structure of the iodide-2TU cluster.....35
Figure 3.2: Schematic of singly occupied orbitals of (a) DB state and (b) VB state of 2TU anion in I⁻·2TU.....36
Figure 3.3: One photon photoelectron spectra of I^-·2TU with the photon energies of 4.73 eV and 4.16 eV 39
Figure 3.4: Contour plot of TRPE spectra of I^-·2TU with excitation and probe pulses of 4.16 eV and 1.59 eV, respectively..... 40
Figure 3.5: Contour plot of TRPE spectra of I^-·2TU at excitation and probe energies of 4.73 eV and 1.59 eV 41
Figure 3.6: Contour plots of TRPE spectra of I^-·2TU photodetached by 3.18 eV with excitation energies of 4.16 eV and 4.73 eV 41
Figure 3.7: Time evolution of the DB and VB ions of I^-·2TU at excitations and probe energies of 4.16 eV and 1.59 eV 42
Figure 3.8: Time evolution of the two VB signals of I^-·2TU at excitation and probe energies of 4.73 eV and 1.59 eV 43
Figure 3.9:Time evolution of the features obtained with 3.16 eV probe and 4.16 eV and 4.73 eV excitation 44
Figure 3.10: Schematic diagram of the energy levels of the neutral, dipole bound anion, and valence bound anion for 2TU and U.....46
Figure 3.S1: Potential energy curve calculated by geometric optimization of I^-·2TU at fixed I–N1 distances.....51
Figure 3.S2: Time evolution of the DB and VB ions of I^-·2TU at excitations and probe energies of 4.16 eV and 1.59 eV fitted with bi-exponential and tri-exponential functions ...52

Electron Transfer Dynamics of Iodide-4-thiouracil Cluster

Figure 4.1: Key TRPES and photodepletion spectra related to the I^-·4TU cluster 57
Figure 4.2: One color spectra of I–·4TU collected with 4.92eV and 3.88eV excitation 59
Figure 4.3: Plot of I–·4TU TRPE spectra with 3.88eV pump and 1.55eV probe pulses.....60

Figure 4.4: Contour plot of I–·4TU TRPE spectra with 4.16 eV pump and 1.55 eV probe pulses....61
Figure 4.5: Contour plot of I–·4TU TRPE spectra with 3.14 eV probe and 3.88eV or 4.16 eV pump pulses....61
Figure 4.6: Time evolution of VB ion and AD signals for 3.88eV excitation, 1.55eV probe TRPES of I–·4TU....63
Figure 4.7: Time evolution of integrated feature DB ion, VB ion, and AD signals for 4.16eV excitation, 1.55eV probe TRPES of I–·4TU....64
Figure 4.8: Vertical detachment energies and normalized signal intensity for DB ion peak up to 2.5 ps....65
Figure 4.9: Time evolution of I^- signal from3.14 eV probe and 4.16eV or 3.88 eV excitation TRPE spectra....66
Figure 4.10: RRKM calculated dissociation time vs dissociation potential well depth for 3.88 eV and 4.16 eV excitation....70

UV Probe Measurements of Nucleobase Excited Iodide-Thymine Cluster

Figure 5.1: Contour plots of I^-·T cluster excited with 4.7 eV and probed with 3.16 eV....79
Figure 5.2: TRPE spectra of I^-·T cluster excited at 4.7 eV and probed at 1.56 eV....79
Figure 5.3: Integrated signal intensity from bare I^- signal of I^-·T excited at 4.74 eV....80
Figure 5.4: Time evolution of VB canonical and VB tautomer signals for I^-·T cluster excited at 4.7 eV and probed at 3.16 eV....81
Figure 5.5: Time evolution of VB canonical and VB tautomer signals for I^-·T cluster excited at 4.7 eV and probed at 3.16 eV....82
Figure 5.6: Time evolution of VB canonical ion and AD signal for I^-·T cluster excited with 4.7 eV and probed with 3.16 eV....82
Figure 5.7: Time evolution of VB canonical ion and VB tautomer ion signals of I^-·T excited with 4.7 eV and probed with 1.56 eV....83
Figure 5.8: Structures of canonical thymine and the R15 rare tautomer....84
Figure 5.S1: Time evolution of VB canonical ion, VB tautomer ion, and AD signals of I^-·T compared to fluctuations of the direct detachment signal....86

Acknowledgements

I am incredibly grateful for the many people who have made this thesis possible.

Firstly, to Dan. Thank you so much for the opportunity I have had to learn and grow as a scientist in this group. I was very conscious of the trust you put in me to figure things out as a young graduate student; I will forever be grateful for the confidence you have had (or at least kindly pretended to have) in my ability to make things work, as well as your willingness to intervene when I realized I was in over my head. Time and time again you have pushed me to understand these systems more deeply and it has made an incredible difference in the quality of the work I've done. I have learned so much these last years and you have done so much to facilitate that.

Second, to the wonderful members of the Neumark group who I've worked with over the years. Thank you especially to Masa Koga and Jenny Wu, who were with me through both successes and misadventures in lab. You worked with me and celebrated with me and gave me the persistence to keep going when things were at their worst. Thank you to Katharine Lunny and Alice Kunin, who got me started on this project and taught me so much about vacuum and laser systems. You are brilliant women who set the standard for me for FPES scientists. I gained so much, even in my limited time working with you. Thank you also to the other group members who have been there for advise and to chat. There are so many lovely people who have been there for me. The group is in good hands, and I look forward to see where Marty, Korina, Masa, Do, Neal, Walt, Madison, Patrick, Nicki, Zach, Eric and Jenny end up.

Third, to the third floor Benson building gang. To Wendy Williams, Kylie Lytle, Erika Jackson, Alex Farnsworth, and Brigham Pope, you are such wonderful friends. Even though we aren't able to spend much in-person time commiserating and working through problem sets any more, your energy and passion is inspiring. It has been so exciting seeing your research, especially as I've gotten to watch some of your thesis defenses. We've come a long way, and I look forward for the thesis defenses still to come. I'm certain that there are wonderful things to come for each one of you.

Fourth, to my parents. Your consistent love and support makes all the difference in my life.

Finally, to Larry. You make my life immeasurably better. You are so incredibly kind and smart and giving. Thank you so much for everything you have done to support me in the final stage of thesis writing, as well as the joy you've added to my life these last several years. Thank you for believing in me when I had trouble believing in myself, for making dinner, for doing dishes, and for a million other things. You are a wonderful partner and friend and I love you so much.

Chapter 1

Introduction

1.1 Overview

The attachment of low energy electrons to chromophore species comprises a key mechanistic step in a variety of biologically relevant processes, including UV induced photolesions of DNA and RNA genetic materials.[1] It has been shown that these electron attachment events may be profitably studied by a variety of experimental methods, including time-resolved photoelectron spectroscopy (TRPES). In particular, we have applied TRPES to iodide nucleobase clusters, where the iodide acts as controllable method of low energy electron donation to the nucleobase chromophore.[2-13]

This thesis explores the profound implications that small modifications to nucleobase structure can have on the electron accommodation dynamics. The first two chapters provide the background for the main body of the thesis. Chapter 1 covers the basic principles and context of electron attachment to nucleobases, time-resolved photoelectron spectroscopy, and the mechanisms for nucleobase anion decay. Chapter 2 explains the experimental details of the time-resolved photoelectron imaging setup, as well as the fundamentals of data analysis. Each of the main body chapters discusses the impact of a different modification to uracil. Chapter 3 discusses the impact of sulfur substitution at the C2 position (Figure 1.1 B) by probing the transient negative ions of the iodide 2-thiouracil cluster. This cluster exhibits accelerated decay of several of the transient anions as well as iodide dissociation that can be treated well by a simple transition state theory model. Chapter 4 covers the dynamics of I^-·4-thiouracil (Figure 1.1 C) upon excitation near cluster vertical detachment energy (VDE) and significantly below the VDE. The evolution of valence bound ion signal even at low excitation energy reveals the key role of nucleobase localized $\pi\pi^*$ excitation for valence bound ion formation without dipole bound ion mediation. Two mechanisms contribute to valence bound ion signal when the cluster is excited near the cluster VDE. Chapter 5 details the dynamics of the I^-·thymine cluster excited at 4.74 eV and probed with a 3.16 eV pulse. The slow rise time of dissociated I^- and rapid decay of the valence bound ion signal implicates the valence bound ion of a stable tautomer of thymine, with measurable signal at a binding energy of 1–2 eV.

1.2 Motivation

DNA and RNA, the fundamental data storage devices for biological information, are highly susceptible to degradation following interaction with ionizing radiation. There are many mechanisms by which this damage can take place, including direct and indirect interactions

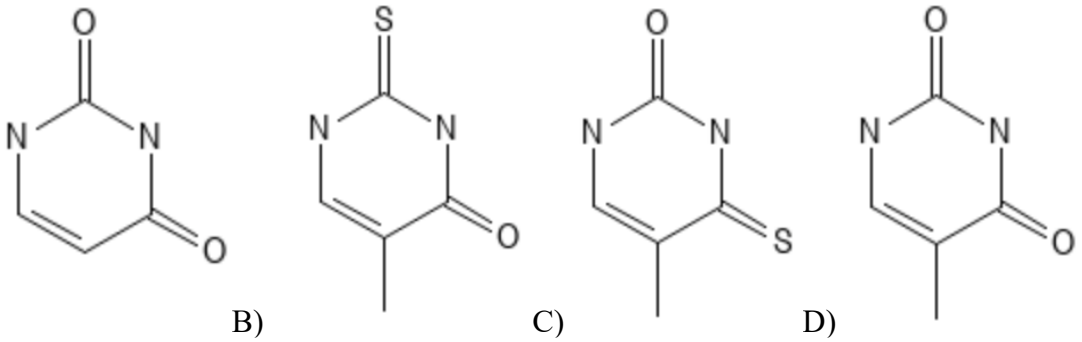

Figure 1.1: Structures of uracil (A) and the modified uracil structures considered herein: 2-thiouracil (B), 4-thiouracil (C), and thymine (D)

between the radiation and the nucleic acid strand.[14, 15] It is estimated that indirect interactions likely account for more than 60% of strand damage,[15] as DNA's intrinsic photostability and low concentration in vivo limit the probability of damage by direct interaction. DNA's photostability is largely attributable to a number of rapid, non-adiabatic processes that facilitate relaxation following UV excitation.[16-22] Indirect interactions take place as the radiation impinges on the cellular matrix, which is mostly composed of water, generating charged species including electrons and OH and H radicals.[14, 15]

These low energy electrons are shown by Boudaiffa et al. to be a major source of DNA damage, even when the electron energy is well below the strand's ionization energy.[23] Furthermore, strand damage is maximized at specific electron kinetic energies, suggesting the importance of some form of resonance in the breakage mechanism. These breakage maxima have since been associated, via experimental and computational work, with dissociative attachment to nucleobases.[24-26] Attachment via shape resonances populates anti-bonding orbitals, leading to the rupture of one or more covalent bonds.

As understanding of the canonical nucleobases increases, interest has expanded to include modified nucleobases called thiobases. In these species, one or both carbonyl oxygens is replaced by sulfur, with dramatic impact on chromophore photophysics. Unlike natural nucleobases, thiobases are prone to intersystem crossing upon UV excitation, making them comparatively reactive.[27-34] This, along with their affinity to bind to DNA, gives them potential for applications such as phototherapeutic agents and immunosuppressants.[35-38] Furthermore, their fundamental photophysical properties provide a crucial point of comparison to canonical nucleobases that can illuminate the mechanisms at work for both modified and canonical nucleobase species.

1.3 Nucleobase Anions

Electron accommodation on a nucleobase gives rise to two distinct anion signals in measurements by photoelectron spectroscopy and dissociative electron attachment (Figure 1.2).[39-42] Valence bound anions are formed as electron transfer causes population of the lowest unoccupied molecular orbital (LUMO) of the molecule. For nucleobases, these are typically π^* anti-bonding orbitals.[3, 25] Computational results, supported by experimental measurements, suggest that populating the LUMO causes a puckering-type distortion of the ring, which is planar in the neutral.[3, 43] Our measurements have found these anions to be typically bound by a few hundred meV;[3] however signal from the VB anions of the canonical nucleobases may not be observed depending on the ionization and vaporization processes utilized.[41]

A molecule with a sufficiently large dipolar moment (>2.4 D) may also form an anion as the excess electron interacts with the molecular dipole.[44, 45] This results in a dipole bound anion which is loosely bound at the positive end of the dipole. Compared to a valence bound anion, a dipole bound anion leaves the nuclear core unperturbed, with a molecular geometry similar to the neutral. The DB anion signal dominates photoelectron spectra of the bare nucleobases in gas phase[40] and is also present in clusters with a small number of water molecules.[11] In solution, the DB state is destabilized relative to the VB state, so that DB signal is not observed.[46] It has been shown that

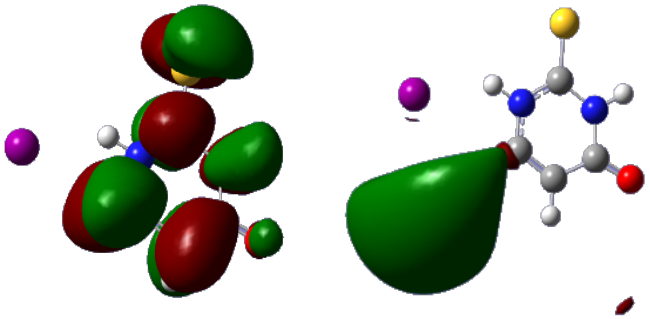

Figure 1.2: Valence bound and dipole bound anions of I^-·4-thiouracil

dipole bound anions play important roles in charge transfer processes, the formation of valance bound species, and explaining diffuse interstellar bands.[46]

The binding energy of a dipole bound state can be estimated as

$$E \propto -\frac{\mu e \cos\theta^2}{r} \qquad \text{Eq. 0.1}$$

where μ is the dipole moment of the molecule and r is the radius from the point dipole.[44] This approximation neglects electron correlation and orbital relaxation effect, as it treats the system with the Koopmans' theorem approach.[46] It also fails to account for rotational states, which have have significant impact on the observability of the dipole bound state.[47, 48] This approximation is generally sufficient for our purposes but should be used cautiously. For instance, this approximation would predict that the binding energies of dipole bound anions of uracil and thymine would be proportional to their molecular dipole moments, which are roughly equivalent. However, previous TRPES measurements of I^-·U and I^-·T clusters show that the centers of the dipole bound features at long times are 95 meV and 75 meV respectively, or a difference of about 25%.[10] This difference may attributed to differences in the electron correlation term due to the electron donating nature of the thymine methyl group, though this is somewhat speculative.

The longevity of nucleobases anions, particularly dipole bound ions, varies significantly for the set of species considered herein. Some nucleobase anions are stable over several ns, but many are short-lived states that rapidly decay by electron autodetachment and H abstraction. These states may be generally thought of as nonstationary states of the time-dependent Schrödinger equation.

Compared to the canonical nucleobases uracil and thymine, thiouracils have stabilized valence bound states, as reflected in the lower energy $\pi\pi^*$ transitions for these molecules. Bai and Barbatti attribute this stabilization to the weakness of a C=S bond compared to a C=O bond. The result is a red shift in $\pi\pi^*$ transitions of 263 nm to 290 nm to 330 nm in thymine, 2-thiothymine, and 4-thiothymine respectively.[49] This effect is particularly important in the case of 4-thiouracil as discussed in chapter 4, as it allows us to isolate the effects of nucleobase localized excitation on the formation of the valence bound anion. Dipole bound anions of the thiouracils appear to have binding energies higher than their canonical counterparts. Both 2-thiouracil and 4-thiouracil have higher dipole moments than canonical uracil,[50, 51] enabling them to better stabilize an excess charge via electrostatic interactions. This does not necessarily correspond to a longer lived dipole bound

state, as the complete dynamics depend on many factors, including the relative energies of the valence bound and dipole bound states.

1.4 TRPES of iodide-chromophore clusters

Given the metastable nature of many nucleobase anions, a time-resolved technique is required to measure these states just after their formation, as well as the ways in which they interconvert. In a halide nucleobase cluster, the iodide can act as an electron donor and the nucleobase as a charge acceptor following excitation. These clusters can be characterized by their vertical detachment energies (VDE), the energy difference between the anion and neutral potential energy surfaces at the anion equilibrium geometry. Photofragment action spectroscopy and previous photoelectron spectroscopy demonstrate that near VDE excitation of a halide-associated cluster causes the excess electron initially localized on the iodine to undergo charge transfer to solvent, potentially forming transient anions. Thus time-resolved charge transfer can be readily measured using a pump-probe technique on an iodide-chromophore cluster.

By initiating charge transfer, the pump excitation acts as a preparation step for the transient chromophore anion. The probe pulse acts to detach the excess electron in cases where the probe pulse energy is greater than the electron binding energy.

$$eKE = h\nu_{probe} - eBE \qquad \text{Eq. 0.2}$$

By measuring the kinetic energy of the detached electron by time of flight or a charged particle imaging technique, the electron binding energy can be determined for a known probe photon energy.

$$I^- \cdot N \rightarrow [I \cdot N]^{-*} \rightarrow I \cdot N + e^- \qquad \text{Eq. 0.3}$$

The use of ultrafast laser pulses allows us to track transient formation and decay on the femtosecond to picosecond timescale. A schematic representation of the potential surfaces involved are included as Figure 1.3. The pump pulse excites the cluster from the ground state anion surface to the excited anion state, which can evolve in time. As the probe pulse interacts with the excited anion, different portions of potential energy surface of the neutral are accessed.

Photoelectron spectroscopy is particularly useful in studies of nucleobase anion transients, as dipole bound and valence bound anions may be readily discriminated by this technique. The intensity of the photoelectron signal for any given transition between the anion and neutral is determined by the Frank-Condon overlap between the two states. The ring deformation of valence bound nucleobase anions causes VB signals to be relatively diffuse and broad.[22, 52] By comparison, the DB anion has a much narrower spectral fingerprint as a result of a geometry relatively unperturbed relative to the neutral.[40, 52] Thus the anions can be discriminated not only by binding energy but also by spectral shape

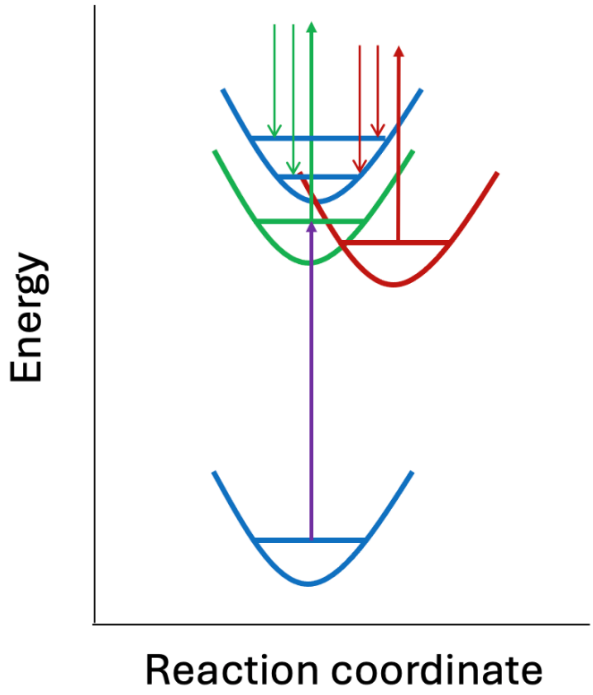

Figure 1.3: Schematic representing time-resolved photoelectron spectroscopy. The lowest lying blue surface is representative of the anion ground state. The purple arrow represents the initial excitation of the anion to form the transient anion, which is capable of evolving in time. The pulse detaching from the green transient surface to the neutral surface (green arrow) results in a strong transition probability to the neutral ground state and the pulse detaching from the red transient surface results in multiple low intensity transitions due to the offset of this transient compared to the neutral along the reaction coordinate. The downward facing arrows are representative of the kinetic energy of the electrons detached by each transition.

Previous work has thoroughly analyzed the dynamics of iodide-uracil and iodide-uracil water clusters upon UV radiation.[2-4, 6, 8, 11, 53] Excitation near the VDE results in signal from both dipole bound and valence bound anions, with signal from the dipole bound ion consistently preceding signal from the valence bound state. This pattern, in combination with experimental and computational work in other groups,[54-56] suggests that the DB anion acts as an intermediate state between the ground state cluster, where the excess electron is localized on the iodide, and the VB state.

As the excitation energy increases to well above the VDE, the relative intensity of the DB decreases relative to the VB state, until the DB state disappears completely as seen at 4.6 eV excitation. The VB state is still present with a reasonable degree of strength, and appears very rapidly. The precise mechanism behind VB formation without DB state contribution has remained unclear, with potential explanations including electron scattering caused by excitation well above the VDE or nucleobase localized excitation facilitating π vacancy filling.

1.5 TRPES derivation

Experimentally, the signals in TRPE spectra come from the kinetic energy of electrons detached from anionic clusters. The following, which draws on work by Bill Miller and co-workers,[57] derives the transition probability between states with energy E_i and E_f. At time t_f, the transition probability is given by

$$P_{E_i \to E_f}(t_f) = \left|\langle \Psi_f | \Psi_i \rangle\right|^2 \qquad \text{Eq. 0.4}$$

Where Ψ is the molecular wavefunction. We can also express Ψ as a linear sum of eigenstates.

$$\Psi = \sum_n c_n |n\rangle \qquad \text{Eq. 0.5}$$

Next consider the time dependent Schrödinger equation.

$$i\frac{\partial}{\partial t}|\Psi(\mathrm{t})\rangle = \hat{H}|\Psi(t)\rangle \qquad \text{Eq. 0.6}$$

Here $\hat{H}$ is the time independent Hamiltonian operator. The time-dependent wavefunction can be expressed in terms of the Hamiltonian and the initial wavefunction. Combining this with Eq 1.2, we get

$$|\Psi(\mathrm{t})\rangle = e^{-\frac{i\hat{H}(t-t_0)}{\hbar}}|\Psi(t_0)\rangle = \sum_n c_n\, e^{-\frac{iE_n(t-t_0)}{\hbar}}|n\rangle \qquad \text{Eq. 0.7}$$

This is more accessible using the Taylor series expansion for the exponential term.

$$|\Psi(\mathrm{t})\rangle = \left(I + \left(\frac{-i}{\hbar}\right)\int_{t_0}^{t_f} dt\hat{H} + \left(\frac{-i}{\hbar}\right)^2 \int_{t_0}^{t} dt\hat{H}(t)dt'\hat{H}(t') + \cdots\right)|\Psi(t_0) \qquad \text{Eq. 0.8}$$

The Hamiltonian contains both time independent and time dependent components, which we will here call H_0 and $H_1(t)$ (Eq 1.9). Because of this separability, we can rewrite the expression above as a Dyson series.

$$H = H_0 + H_1(t) \qquad \text{Eq. 0.9}$$

$$\begin{aligned} &|\Psi(t_f)\rangle \qquad \text{Eq. 0.10}\\ &= \left(I + \left(\frac{-i}{\hbar}\right)\int_{t_0}^{t_f} dt e^{\frac{iH_0(t_f-t)}{\hbar}}\hat{H}_1 e^{\frac{-iH_0(t-t_0)}{\hbar}}\right.\\ &+ \left(\frac{-i}{\hbar}\right)^2 \int_{t_0}^{t} dt \int_{t}^{t_f} dt' e^{\frac{iH_0(t_f-t)}{\hbar}}\hat{H}_1(t) e^{\frac{-iH_0(t-t')}{\hbar}}\hat{H}_1(t') e^{\frac{iH_0(t'-t_0)}{\hbar}}\\ &\left.+ \cdots\right)|\Psi(t_0)\rangle \end{aligned}$$

For one photon anion PES, the first order expansion of this series is sufficient; however, our time resolved measurements require the second order term. In the weak-field electric dipole approximation, the perturbation term of the Hamiltonian is given by

$$H_1(t) = -\hat{\boldsymbol{\mu}} \cdot \varepsilon(t) \qquad \text{Eq. 0.11}$$

where $\hat{\boldsymbol{\mu}}$ is the electron dipole matrix element. Because we are operating using the Condon approximation, the nuclear wavefunction is separable from the transition dipole moment. Under this approximation, the following expressions are equivalent.

$$\left|\langle \Psi_f | \, \hat{\boldsymbol{\mu}} \cdot \varepsilon(t) | \Psi_i \rangle\right|^2 = \left|\langle \chi_F | \chi_g \rangle\right|^2 \left|\langle \phi_F | \, \hat{\boldsymbol{\mu}} \cdot \varepsilon(t) | \phi_g \rangle\right|^2 \qquad \text{Eq. 0.12}$$

In this expression, χ represents the nuclear component of the relevant wavefunction and ϕ the electronic component. The term $\left|\langle \chi_F | \chi_g \rangle\right|^2$ is called the Franck-Condon factor, and we can replace the expression $\langle \phi_F | \, \hat{\boldsymbol{\mu}} \cdot \varepsilon(t) | \phi_g \rangle$ by $\hat{\boldsymbol{\mu}}_{F,g}$ for convenience.

Substituting the first order term for the wavefunction derived above into the expression for the transition probability, we obtain

$$P = \left(\frac{i}{\hbar}\right)^2 \left| \int_{t_0}^{t_f} dt \, e^{-\frac{iE_f(t_f - t)}{\hbar}} \left(\mu_{f,i} \cdot \varepsilon(t)\right) e^{-\frac{iE_i(t - t_0)}{\hbar}} \right|^2 \qquad \text{Eq. 0.13}$$

$$= \left(\frac{-i}{\hbar}\right)^2 \left| \int_{t_0}^{t_f} dt \, e^{\frac{i(E_f - E_i)t}{\hbar}} \left(\mu_{f,i} \cdot \varepsilon(t)\right) \right|^2$$

Note that if we chose a different perturbation, $\hat{H}_1 = ke^{-i\omega t}$, we would recover a transition probability

$$P_{i \to f}(t) = \left(\frac{i}{\hbar}\right)^2 \left| \int_0^t dt' e^{i\omega_{fi}t'} e^{-i\omega t'} \langle \Phi_f | \varepsilon_0 | \Phi_i \rangle \right|^2 \qquad \text{Eq. 0.14}$$

The transition rate is related to the transition probability by

$$\Gamma_{i \to f} = \frac{dP_{E_i \to E_f}}{dt} \qquad \text{Eq. 0.15}$$

The expression for the transition rate would be

$$\Gamma_{i \to f} = \frac{2\pi}{\hbar^2} \left|\langle \Phi_f | \varepsilon_0 | \Phi_i \rangle\right|^2 \delta(\omega_{fi} - \omega) \qquad \text{Eq. 0.16}$$

which recovers Fermi's Golden Rule for a harmonic perturbation.

In photoelectron spectroscopy, the total final energy of the system will be the sum of the energy of the neutral species and the detached electron, which we will label as E_F and ϵ respectively. the transition probability can therefore be expressed as

$$P_{E_i \to E_f}(t_f) = P(E_F, \epsilon) \propto \left|\langle \chi_{E_F} | \chi_g \rangle\right|^2 \left| \int_{t_0}^{t_f} dt \left(\mu_{F,g} \cdot \varepsilon(t)\right) e^{\frac{(E_F + \epsilon - E_g)t}{\hbar}} \right|^2 \qquad \text{Eq. 0.17}$$

As indicated previously, our experiment measures only the electron kinetic energy directly, so the transition probability we are most interested in is $P(\epsilon)$, not $P(E_F,\epsilon)$. In order to recover $P(\epsilon)$, we must integrate over E_F. The final expression for will be $P(\epsilon)$ will be proportional to the following integral

$$\int_{t_0}^{t} dt \int_{t}^{t_f} dt' \varepsilon(t)\varepsilon(t') e^{i(E_g-\epsilon)(t-t_0)/\hbar} \langle \chi_g \left| e^{-\frac{i\hat{H}_F(t-t_0)}{\hbar}} \right| \chi_g \rangle \qquad \text{Eq. 0.18}$$

where $\hat{H}_F$ is the nuclear Hamiltonian for the final state.

This derivation accounts for a one photon photoelectron spectroscopy experiment, but we are conducting a two photon experiment. In this case, the initial photon prepares the intermediate state A, then the second photon detaches to produce the final state

$$M^-(E_g) + \hbar\omega_1 \rightarrow M^-(E_g) + \hbar\omega_2 \rightarrow M(E_f) + e^-(\epsilon) \qquad \text{Eq. 0.19}$$

The electric field may be considered as the sum of two fields

$$\varepsilon(t) = \varepsilon_{01} E_1(t) e^{-i\omega_1 t} + \varepsilon_{02} E_2(t) e^{-i\omega_2(t-\Delta t)} \qquad \text{Eq. 0.20}$$

Where ε_{0N} are the time independent components, E_N is the temporal shape of the pulse, and Δt is the time between the pulses. In this case we require the second-order expression for the final wave function.

The transition probability for this process would be given by

$$P_{E_i \rightarrow E_f} = \left| -\frac{i}{\hbar} \int_{t_0}^{t_f} dt \int_{t_0}^{t} dt'\, e^{-\frac{i(E_f)t}{\hbar}} \left(\mu_{f,A} \cdot \varepsilon(t)\right) e^{-\frac{iE_A(t-t')}{\hbar}} \left(\mu_{A,i} \cdot \varepsilon(t')\right) e^{-\frac{iE_i t'}{\hbar}} \right|^2 \qquad \text{Eq. 0.21}$$

Substituting our expressions for $\varepsilon(t)$ and the separable expression for the transition dipole moment and integrating over E_F, we eventually obtain the following expression, where H_A is the nuclear Hamiltonian for the intermediate state.

$$P(\epsilon,\Delta t) \propto \int_{t_0}^{t_f} dt \int_{t_0}^{t} dt' \int_{t_0}^{t_f} dt'' \int_{t_0}^{t''} dt'''\, E_2(t-\Delta t) E_2(t''-\Delta t) E_1(t') E_1(t''') \cdot e^{\frac{iE_g(t')}{\hbar}} \times e^{-i\omega_2(t-\Delta t)} \cdot e^{-i\omega_2(t''-\Delta t)} \cdot e^{-i\omega_1(t')} \cdot e^{-i\omega_1(t''')} \cdot e^{\frac{i\epsilon(t-t'')}{\hbar}} e^{\frac{iE_g(t'''-t')}{\hbar}} \times \langle \chi_g \left| e^{-\frac{iH_A(t'''-t'')}{\hbar}} e^{-\frac{iH_F(t''-t)}{\hbar}} \right| \chi_g \rangle \qquad \text{Eq. 0.23}$$

As t_f goes to infinity, this simplifies to

$$P(\epsilon,\Delta t) \propto \int_{t_0}^{t_f} dt \int_{t_0}^{t} dt' \int_{t_0}^{t_f} dt'' \int_{t_0}^{t''} dt''' \, E_2(t-\Delta t)E_2(t''-\Delta t)E_1(t')E_1(t''') \cdot e^{\frac{iE_g(t')}{\hbar}} \times e^{-i\omega_2(t-\Delta t)} \cdot e^{-i\omega_2(t''-\Delta t)} \cdot e^{-i\omega_1(t')} \cdot e^{-i\omega_1(t''')} \cdot e^{\frac{i\epsilon(t-t'')}{\hbar}} e^{\frac{iE_g(t'''-t')}{\hbar}} \times \langle \chi_g \left| e^{-\frac{iH_A(t'''-t'')}{\hbar}} e^{-\frac{iH_F(t''-t)}{\hbar}} \right| \chi_g \rangle \quad \text{Eq. 0.24}$$

1.6 Dissociation and RRKM Modeling

Following excitation of the cluster and formation of the chromophore transients, the cluster may relax in any of several ways, including electron autodetachment and internal conversion.[58] Photofragmentation studies suggest that the abstraction of H from the nucleobase may also yield a stable species for some thiobases.[50]

Autodetachment is a spontaneous process wherein an electron is emitted from a metastable ion. For transients with energies that fall within the vibration manifold of the neutral, non adiabatic coupling can enable the emission of the excess electron.[44, 59] The autodetached electrons are emitted isotropically with low kinetic energy. Where possible, we have analyzed the autodetachment dynamics of these clusters. However this analysis can be complex and occasionally unintuitive, as autodetachment is able to proceed without interaction with the probe pulse. In the time resolved spectra, we are particularly interested in the time scales on which autodetachment signal is depleted or exceeds the level observed with strictly one color excitation of the cluster.

Photodissociation studies have shown that dissociated I^- is a major decay product following excitation of iodide-chromophore clusters by wavelengths throughout the UV range.[50, 58] Transient nucleobase anion populations are depleted as back electron transfer reforms I^-, and cluster is left in a vibrationally hot ground electronic state, which can go on to dissociate leaving free I^-.

$$I \cdot N_{TNI}^- \rightarrow I^- \cdot N \rightarrow I^- + N \quad \text{Eq. 0.25}$$

The rate of this reaction can be approximated using the unimolecular dissociation transition state method Rice-Ramsperger-Kassel-Marcus (RRKM) theory.[60, 61] RRKM modeling makes a number of assumptions that are key to evaluating the accuracy of calculated dissociation rates. Firstly, it assumes that a system passing through the transition state exactly once. Secondly, it assumes a statistical dissociation of the complex, wherein all internal states of the molecule at some energy E are accessible. Thirdly, it assumes the energy exchange between vibrational modes, called intramolecular vibrational relaxation or IVR, occurs much faster than the dissociation itself. A large disagreement between experimental and RRKM modeled reaction rate constants may indicate a breakdown of any of these assumptions.

RRKM treats the system as a set of coupled harmonic oscillators with characteristic frequencies. Following excitation with energy E, the cluster reforms the initial anion $I^- \cdot N$. The cluster is vibrationally excited at this point, with some number of energy quanta in each mode of the cluster.

The transition state is higher in energy than the reactant by the zero-point corrected energy E_0, with $E^{\ddagger}=E-E_0$ representing available energy at the transition state. The rate at which a cluster can pass through the transition state will be related to the ratio between the sum of states G for the transition state at energy $E^{\ddagger}$ and the density of states ρ for the reactant with energy E, or

$$k(E) = \frac{G(E^{\ddagger})}{h\,\rho(E)} \qquad \text{Eq. 0.26}$$

In $I^{-}\cdot N$ clusters, the critical coordinate in reaching the transition state is the I to N_1 bond length. Calculations have shown that these transitions are barrierless, as shown in Figure 1.4. In the absence of clear transition state, the rate constant k(E) can treated variationally with the transition state is chosen so that k is at its minimum. This method leaves a degree of uncertainty in the calculated rate constant, so that agreement between experimental and calculated dissociation rates is considered reasonable if the values are within 2 or 3 times of one another.

The sum and density of states used to calculate the RRKM value of k(E) are easily calculated using the Beyer-Swinehard direct count method.[62] Treating the cluster vibrations as harmonic oscillators, the frequency of each mode is determined e.g. by MP2 calculation in Gaussian. An empty matrix is filled using the assumption that if a state exists at energy E, there must also be a state at E+ω, where ω is the frequency of a vibration. The total number of states at an energy is the sum of the multiples of the various harmonic oscillator frequencies, with the orders of magnitude for the sum and density of states increasing drastically with even moderate excitation. In systems with significant anharmonic characteristics, the density of states can be estimated more accurately by

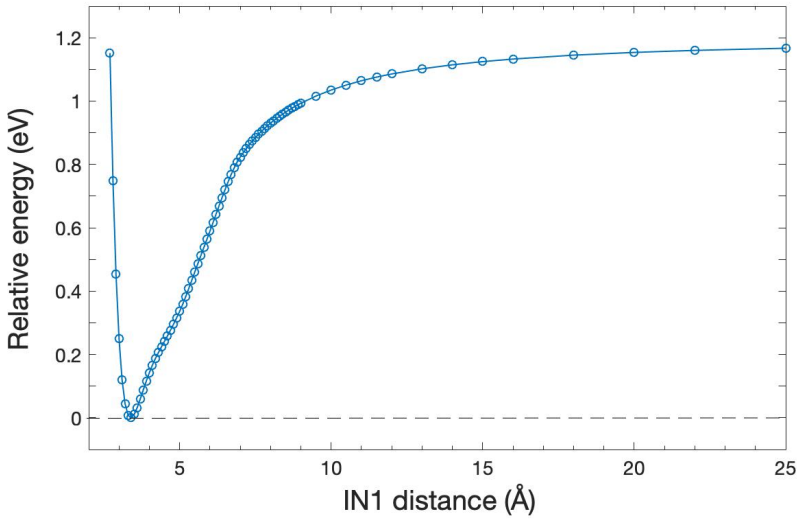

Figure 1.4: Potential energy curve calculated by geometric optimization of the $I^{-}\cdot$2-thiouracil at fixed I–N1 distances. Energies are calculated at MP2/aug-cc-pVDZ-(pp) level of theory.

convolving the matrix resulting from the harmonic modes with a matrix treating the anharmonic modes. This is known as the Stein-Rabinovitch modification.[63]

RRKM is highly sensitive to $E^{\ddagger}$ and therefore to the calculated energy of the transition state, as will be seen in chapter 4. It is also sensitive to low frequency modes, often overestimating their

impact on the total rate. Low-frequency modes can sometimes be better treated as free or hindered rotors than as harmonic oscillators. For example, one of the low energy frequency modes of I^-·2TU can be considered as a twist of the nucleobase ring relative to the iodide, i.e. a hindered rotor interacting with the potential surface arising from interactions between the two bodies.

The partition function of an N dimensional rotor can be expressed as

$$Q = \frac{1}{\sigma h^N} \int_0^\infty d\Gamma e^{-\frac{H}{k_B T}} \quad \text{Eq. 0.27}$$

with the Hamiltonian for a one-dimensional rotor given by

$$H = \frac{p_\theta^2}{2I} \quad \text{Eq. 0.28}$$

and the Hamiltonian for a two-dimensional rotor given by

$$H = \frac{1}{2I}\left(p_\theta^2 + \frac{p_\phi^2}{\sin^2\theta}\right) + V(\theta, \phi) \quad \text{Eq. 0.29}$$

where $d\Gamma$ is an integration over the full space, σ is the symmetry number for the rotation, I is the moment of inertia, and p_θ and p_ϕ are the angular momenta corresponding to the Euler angles spanning three dimensional space ($0 < \theta < \pi, 0 < \phi < 2\phi$). The potential $V(\theta, \phi)$ is angle dependent and, in the case of I^-·N dissociation, can be determined by varying the angle between the nucleobase and iodide and fitting the resultant energies to

$$V(\theta) = \frac{V_0}{2}\cos(1 - \sigma\theta) \quad \text{Eq. 0.30}$$

The density of states can be determined by taking the inverse Laplace transform of the appropriate partition function, and the total density of states is the convolution of the inverse Laplace transform with the harmonic density of states. In the RRKM modeling presented within this and past theses, the hindered rotor correction decreases the predicted reaction rate by >10%.[2, 5, 8, 9]

1.7 Computational Methods

Interpretation of the experimental results often necessitates the use of computational modeling. Treatment of a I^-·N cluster presents a few challenges in these calculations, particularly because of the presence of iodine and the importance of the dipole bound anion.

Diffuse, long range interactions are key to accurate approximation of cluster properties, as interactions between the nucleobase and iodine are key in understanding the overall dynamics of the cluster, but are mediated through relatively long-range ion dipole interactions. Additionally, the stability of dipole bound anions is significantly impacted by correlation effects,[45] even though the main electron density is relatively far from the nucleobase ring. Due to these constraints, a post-HartreeFock level of theory, such as second order Moller-Plesset theory (MP2) or CCSD is necessary.

Basis set must also be selected with a view toward the diffuse dipole bound state. We have had success using the augmented correlation-consistent Dunning basis sets (aug-cc-pVDZ or -pVTZ).[8, 9, 11, 53] Alternatively, Takayanagi and coworkers have used long-range corrected density functional theory (LC-DFT) with CAM-B3LYP and ωB97XD functionals to accurately calculate both VB and DB anions of iodide pyrimidine clusters.[10, 12] Given the considerable size of iodine, it is advantageous to treat its core electrons as a static pseudo-potential. Although this may introduce some small inaccuracies, it is necessary for calculations to be completed in an acceptable length of time.

Substantially less computational work has been carried out for thiouracils than the canonical pyrimidines. Ortiz and coworkers have calculated the vertical and adiabatic electron affinities for the VB anions of all three thiouracils, using a 6-311++G(2df,2p) basis set with MP2, CCSD, and CCSD(T), although the energies of the dipole bound anions was not reported.[64] Uleanya et al. have calculated excitation spectra by time dependent DFT (TD-DFT) calculations with a B3LYP/6-311++G(2d,2p) basis set.[50] The TD-DFT calculations were found to approximate the excitations of the thiobases accurately, but failed to predict dipole bound anion with any strength despite the presence of these species in experiment. This may be caused because of this approach's neglect of long-range correlation effects.

1.8 Systems Studied

I–·2-thiouracil

Electron accommodation dynamics of the iodide 2-thiouracil cluster are studied following excitation at 4.16 eV (near VDE) and 4.72 eV (high energy), and are measured by 1.58 eV and 3.16 eV probe pulse energies. Near VDE excitation gives rise to DB and VB signal, with the DB signal appearing and decaying on ultrafast timescales (within the instrument response time). At 4.73 eV excitation, no DB signal is seen, but two signals are attributed to distinct but energetically similar VB anions. The appearance of this second VB anion signal is likely due to the two nearly degenerate $\pi\pi^*$ excitations of 2-thiouracil. A higher probe energy (3.16 eV) reveals rapid dissociation of the cluster compared to I^-·U, with a rate in reasonable agreement with what is predicted by RRKM. Based on this result, we propose that initial decay of the VB anion is by back electron transfer to reform I^-, leaving a vibrationally excited cluster that undergoes statistical dissociation.

I⁻·4-thiouracil

Whereas clusters of iodide with the canonical nucleobases have $\pi\pi^*$ transitions accessible by excitation with 4.62 eV pump pulse, the stabilization of the LUMO of 4 thiouracil is sufficient that the lowest energy $\pi\pi^*$ transition lies well below the VDE for the cluster. As a result, the role of nucleobase-localized excitation on transient formation may be isolated from other high energy electron scattering processes. In this study, we show that low energy $\pi\pi^*$ excitation facilitates the formation of valence bound anions without the mediation of a dipole bound state, providing empirical evidence for a previously proposed mechanism.

Near-VDE excitation of the cluster gives rise to DB and VB anion signal, with two distinct time regimes for VB anion formation. The first is ultra-fast formation associated with $\pi\pi^*$ excitation and the second is a slower rise corresponding to depletion of the DB signal. The decay dynamics of this VB state reveal the role of neutral iodine in VB decay, as VB longevity is greatly increased after iodine is predicted to have dissociated from the cluster.

I^-·thymine

We have previously published TRPES studies for the iodide thymine cluster probed with a 1.55 eV pulse, determining the transient ion dynamics of the cluster. However, dynamics measured by near UV probe energy (3.16 eV), which has been useful in determining dissociation dynamics for other clusters, had not been reported for iodide-thymine. Here we publish the dynamics for I^-·T excited at 4.67 eV and measured by 3.16 eV probe. We find that signal from dissociated iodide rises with an anomalously slow rate compared to other iodide nucleobase clusters, despite short-lived nucleobase anions.

In addition to facilitating measurement of iodide dissociation, the higher energy probe makes apparent a secondary ion signal bound by 1–2 eV, in agreement with the calculated vertical detachment energy of a thymine tautomer anion. This suggests that because the VB signal from the canonical tautomer of thymine is depleted rapidly and efficiently by electron autodetachment, reformation of iodide comes from decay of the thymine rare tautomer's VB anion. The rise of the tautomer anion signal gives an approximate tautomerization rate, with a time constant of 8 ps. A possible tautomerization mechanism is discussed in connection with the known processes occurring following cluster excitation at 4.67 eV.

References

1. S. B. Nielsen and J. A. Wyer, *Photophysics of ionic biochromophores*. (Springer, 2013).
2. M. A. Yandell, S. B. King and D. M. Neumark, J. Am. Chem. Soc. **135** (6), 2128–2131 (2013).
3. A. Kunin and D. M. Neumark, Phys. Chem. Chem. Phys. **21** (14), 7239–7255 (2019).
4. S. B. King, M. A. Yandell, A. B. Stephansen and D. M. Neumark, J. Chem. Phys. **141** (22), 224310 (2014).
5. M. Asplund, M. Koga, Y. J. Wu and D. M. Neumark, J. Chem. Phys. **160** (5) (2024).
6. S. B. King, M. A. Yandell and D. M. Neumark, Faraday Discuss. **163**, 59–72 (2013).
7. A. Kunin, W.-L. Li and D. M. Neumark, Phys. Chem. Chem. Phys. **18**, 33226 (2016).
8. W.-L. Li, A. Kunin, E. Matthews, N. Yoshikawa, C. E. Dessent and D. M. Neumark, J. Chem. Phys. **145** (4), 044319 (2016).
9. M. Koga, M. Asplund and D. M. Neumark, J. Chem. Phys. **156**, 24302 (2022).
10. S. B. King, A. B. Stephansen, Y. Yokoi, M. A. Yandell, A. Kunin, Y. Takayanagi and D. M. Neumark, J. Chem. Phys. **143** (2), 024312 (2015).
11. A. Kunin, W.-L. Li and D. M. Neumark, J. Chem. Phys. **149** (8), 084301 (2018).
12. A. B. Stephansen, S. B. King, Y. Yokoi, Y. Minoshima, W.-L. Li, K. A., T. Takayanagi and D. N. Neumark, J. Chem. Phys. **143** (10), 104308 (2015).
13. M. A. Yandell, S. B. King and D. M. Neumark, J. Chem. Phys. **140** (18), 184317 (2014).
14. J. Narayanan S J, D. Tripathi, P. Verma, A. Adhikary and A. K. Dutta, ACS Omega **8** (12), 10669-10689 (2023).
15. E. Alizadeh and L. Sanche, Chem. Rev. **112** (11), 5553–6214 (2012).
16. S. Matsika, J. Phys. Chem. A **108**, 7584–7590 (2004).
17. C. E. Crespo-Hernández, B. Cohen, P. M. Hare and B. Kohler, Chem. Rev. **104**, 1977–2020 (2004).
18. P. J. Hare, C. E. Crespo-Hernández and B. Kohler, Proc. Natl. Acad. Sci. U.S.A. **104** (2), 435–440 (2007).
19. H. Yu, J. A. Sánchez-Rodríguez, M. Pollum, E. Crespo-Hernandez, S. Mai, P. Marquetand, L. Gonzalez and S. Ullrich, Phys. Chem. Chem. Phys. **18**, 20168–20176 (2016).
20. C. T. Middleton, K. de La Harpe, C. Su, Y. K. Law, C. E. Crespo-Hernández and B. Kohler, Annu. Rev. Phys. Chem. **60**, 217–239 (2009).
21. R. Improta, F. Santoro and L. Blancafor, Chem. Rev. **116** (6), 3540–3593 (2016).
22. A. Stolow, A. E. Bragg and D. M. Neumark, Chem. Rev. **104** (4), 1719–1758 (2004).
23. B. Boudaïffa, P. Cloutier, D. Hunting, M. A. Huels and L. Sanche, Science **287**, 1658–1660 (1998).
24. R. Barrios, P. Skurski and J. Simons, J. Phys. Chem. B **106**, 7991–7994 (2002).
25. J. Simons, Acc. Chem. Res. **39**, 772–779 (2006).
26. J. Berdys, I. Anuseiwicz, P. Skurski and J. Simons, J. Am. Chem. Soc **126**, 6441º6447 (2004).
27. M. S. Robinson, M. Niebuhr and M. Gühr, Molecules **28**, 2354 (2023).
28. S. Mai, P. Marquetand and L. González, J. Phys. Chem. Lett. **7** (11), 1978–1983 (2016).
29. A. Mohamadzade, S. Bai, M. Barbatti and S. Ullrich, Chem. Phys. **515**, 572–579 (2018).
30. J. Kopyra, K. K. Kopyra, H. Abdoul-Carime and D. Branowska, J. Chem. Phys. **148** (23), 234301 (2018).
31. J. Kopyra, H. Abdoul-Carime, F. Kossoski and M. d. N. Varella, Phys. Chem. Chem. Phys. **16** (45), 25054–25061 (2014).

32. S. Ullrich, Y. Qu, A. Mohamadzade and S. Shrestha, J. Phys. Chem. A **126** (44), 8211–8217 (2022).
33. M. Pollum and C. E. Crespo-Hernández, J. Chem. Phys. **140**, 071101 (2014).
34. J. A. Sánchez-Rodríguez, A. Mohamadzada, S. Mai, B. Ashwood, M. Pollum, P. Marquetand, L. González, C. E. Crespo-Hernández and S. Ullrich, Phys. Chem. Chem. Phys. **19** (30), 19756–19766 (2017).
35. L. A. Ortiz-Rodrìguez and C. E. Crespo-Hernàndez, Chem. Sci. **11**, 11113–11123 (2020).
36. G. W. Anderson, I. Halverstadt, W. H. Miller and R. O. Roblin Jr, J. Am. Chem. Soc. **67** (12), 2197–2200 (1945).
37. M. Pollum, S. Jockusch and C. E. Crespo-Hernandez, J. Am. Chem. Soc. **136**, 17930–17933 (2014).
38. M. Pollum, S. Jucusch and C. E. Crespo-Hernandez, J. Am. Chem. Soc. **136** (52), 17930–17933 (2014).
39. J. Schiedt, R. Weinkauf, D. M. Neumark and E. W. Schlag, Chem. Phys. **239**, 511–524 (1998).
40. J. H. Hendricks, S. A. Lyapustina, H. L. d. Clercq, J. T. Snodgrass and K. H. Bowen, The Journal of Chemical Physics **104** (19), 7788-7791 (1996).
41. X. Li, K. H. Bowen, M. Haranczyk, R. A. Bachorz, K. Mazurkiewicz, J. Rak and M. Gutowski, J. Chem. Phys. **127** (17), 174309 (2007).
42. P. Burrow, G. A. Gallup, A. M. Scheer, S. Denifl, S. Ptasinska, T. Mark and P. Scheier, J. Chem. Phys. **125** (12), 124310 (2006).
43. R. A. Bachorz, W. Klopper, M. Gutowski, X. Li and K. H. Bowen, J. Chem. Phys. **129** (5), 054309 (2008).
44. J. Simons, J. Phys. Chem. A **112** (29), 6401–6511 (2008).
45. O. H. Crawford, Mol. Phys. **20** (4), 585–591 (1971).
46. K. D. Jordan and F. Wang, Annu. Rev. Phys. Chem. **54**, 367–396 (2003).
47. S. Ard, W. R. Garrett, R. N. Compton, L. Adamowicz and S. G. Stepanian, Chemical Physics Letters **473** (4), 223-226 (2009).
48. D. A. Walthall, J. M. Karty and J. I. Brauman, The Journal of Physical Chemistry A **109** (39), 8794-8799 (2005).
49. S. Bai and M. Barbatti, The Journal of Physical Chemistry A **120** (32), 6342-6350 (2016).
50. K. O. Uleanya and C. E. Dessent, Phys. Chem. Chem. Phys. **23** (2), 1021–1030 (2021).
51. W. C. Schneider and I. F. Halverstadt, Journal of the American Chemical Society **70** (8), 2626-2631 (1948).
52. J. H. Hendricks, S. A. Lyapustina, H. L. de Clercq and K. H. Bowen, J. Chem. Phys. **108**, 8–11 (1998).
53. A. Kunin, V. S. McGraw, K. G. Lunny and D. M. Neumark, J. Chem. Phys. **151** (15), 154304 (2019).
54. R. N. Compton, H. S. Carman, Jr., C. Desfrançois, H. Abdoul‐Carime, J. P. Schermann, J. H. Hendricks, S. A. Lyapustina and K. H. Bowen, The Journal of Chemical Physics **105** (9), 3472-3478 (1996).
55. Sommerfeld, J. Phys. Chem. A. **108** (42), 9150–9154 (2004).
56. P. Mikulski, T. Klahn and P. Krebs, Physical Review A **55** (1), 369-377 (1997).
57. V. S. Batista, M. T. Zanni, B. J. Greenblatt, D. M. Neumark and W. H. Miller, The Journal of chemical physics **110** (8), 3736-3747 (1999).

58. W.-L. Li, A. Kunin, E. Matthews, N. Yoshikawa, C. E. Dessent and D. M. Nuemark, J. Chem. Phys. **145** (4), 044319 (2016).
59. J. Simons, J. Am. Chem. Soc. **103** (14), 3971–3976 (1981).
60. R. G. Gilbert and S. C. Smith, *Theory of unimolecular and recomination reactions*. (Publishers' Business Services, 1990).
61. T. Baer, W. L. Hase and L. William, *Unimolecular reaction dynamics: theory and experiments*. (Oxford University Press on Demand, 1996).
62. T. Beyer and D. Swinehard, Communications of the ACM **16** (6), 379 (1973).
63. S. E. Stein and B. Rabinovitch, J. Chem. Phys. **58** (6), 2438–2445 (1973).
64. O. Dolgounitcheva, V. Zakrzewski and J. Ortiz, J. Chem. Phys. **134** (7), 074305 (2011).

Chapter 2

Experimental Methods

2.1 Overview

The TRPEI setup is described in detail in the theses of Marty Zanni[1] and Jeff Greenblatt[2] with the change from magnetic bottle to VMI detection in the theses of Allison Davis[3] and Arthur Bragg.[4] Various publications also provide information on the experimental setup.[5, 6] This chapter will provide a broad description of the experimental apparatus, as well as information on its day-to-day usage, modifications made in the last five years, and details on the experimental parameters used to generate the data in the following chapters.

Briefly summarized, the TRPEI apparatus generates $I^-{\cdot}N$ clusters by a pulsed supersonic expansion of nucleobase sample, argon buffer gas, and methyl iodide through an ionizing filament. The anionic clusters are extracted perpendicularly to a Wiley McLaren time-of-flight mass spectrometer before the mass of interest is isolated into the interaction region by timed voltage pulsing of the re-referencing tube. In the interaction region, the ion clusters' path intersects with excitation and probe laser pulses, detaching the excess electron. The kinetic energy of the photoelectron is measured by velocity map imaging projection onto multi-channel plates coupled to a phosphor screen, which is imaged by a CCD camera. The apparatus can be generally considered as being comprised of two parts: the high vacuum system used to generate and guide charged species, and the ultrafast laser system used to generate the pump and probe pulses. Each subsystem will be considered in turn.

2.2 Cluster Formation and Optimization

2.2.1 Cluster Generation

Figure 2.1 shows a schematic of the TRPES experimental apparatus. Clusters are formed from a gaseous mixture of argon buffer gas and volatilized sample, in this case methyl iodide and the nucleobase of interest. The vapor pressure of methyl iodide is sufficient to produce the clusters by running the buffer gas over a reservoir of the liquid. This argon/ methyl iodide mixture continues to an Even Lavie (EL) pulsed solenoid valve containing a sample cartridge with the solid nucleobase. At room temperature the nucleobases have minimal vapor pressure, so the valve body is heated to 200-220 °C by a resistive heating unit built into the valve. The sample-containing cartridge is capped by a fine mesh filter.

The pulsed valve itself is sealed by a stainless steel tube, a plunger, a spring, and two ruby pieces that guide the plunger's path.[7] Each end of the tube rests against a polyamide gasket. Regular maintenance of the valve includes replacing the gaskets, which wear down during use. Degradation of the seal along the gaskets is accelerated when the valve is heated frequently, and may be compromised entirely when the valve is heated beyond ~250 °C. For this reason, a moderate valve heat is recommended, even for robust solid samples.

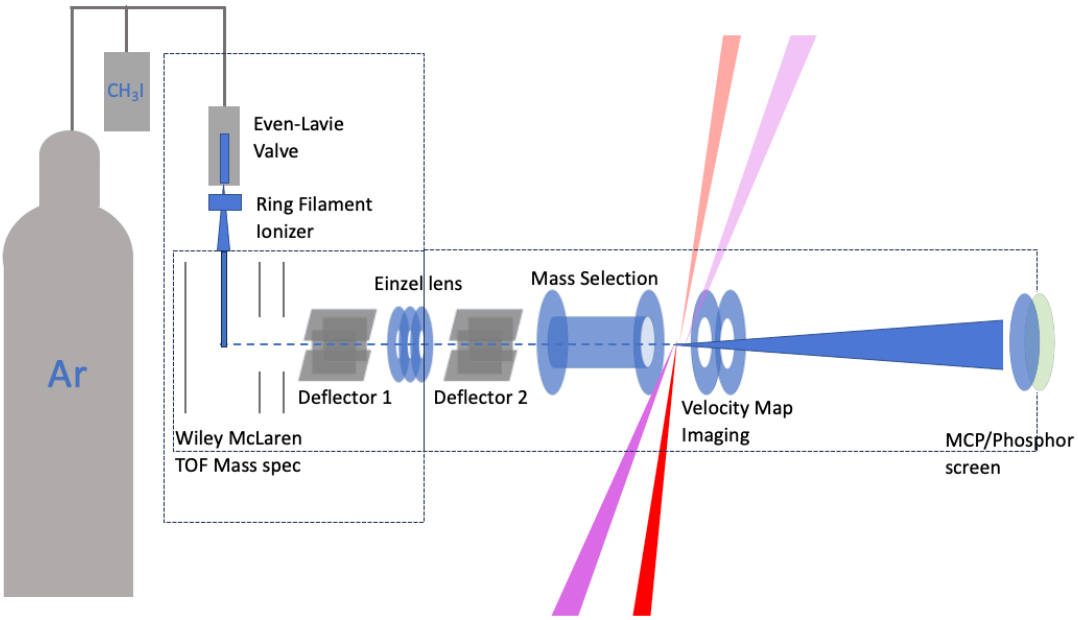

Figure 2.1: Schematic of the TRPES apparatus

As current is applied to the inner valve assembly, a magnetic field is formed which causes the plunger to recoil. This temporarily breaks the seal, allowing gas to flow from the valve through a cone-shaped aperture. At the end of the applied current pulse, the plunger rests back against the front gasket, re-sealing the valve. Over long periods of use, the tip of the plunger may be worn down or deformed such that an adequate seal cannot be achieved despite repeated replacement of the gaskets. Under these circumstances, the plunger must be replaced.

The EL valve has a theoretical maximum repetition rate of 1 kHz; however, we have found that operation at this frequency leads to an unstable ion signal, so the assembly is instead run at 500 Hz.

Cluster formation is facilitated as the gas mixture adiabatically expands from the high pressure gas line ($2.5 \cdot 10^3$ torr) into the low pressure ($\sim 10^{-5}$ torr) source chamber, with collision-induced cooling inducing cluster formation as internal energy of the molecules is converted to translational energy.[8-10] These clusters can be ionized as the cone of expanded gas passes through a ring shaped ionizer placed 7 mm from the valve aperture. Current of ~5A is applied across a thoriated tungsten filament, causing electrons to boil off. A negative pulsed bias of 200-300 V is applied on the outer ring, accelerating the electrons toward the inner mesh, which is at ground. Electron impact with the buffer gas generates lower kinetic energy secondary electrons, as in Equation 1.

$$\mathrm{Ar} + \mathrm{e}^- \rightarrow Ar^+ + 2e^- \qquad \text{Eq. 2.1}$$

These secondary electrons may then attach to the neutral cluster, generating vibrationally cooled anionic clusters. The center of the beam, containing the coolest clusters, passes through a skimmer to the 1D differentially pumped region containing a Wiley McLaren time-of-flight mass spectrometer.

The ionizer filament must be replaced periodically as the thoriated tungsten wire may fracture. If ion signal is very low, we have found that the most common problem is low resistance between the ionizer and ground. In particular, the ceramic insulators in the ionizer body may be jostled out of place, coated in a conductive material, or cracked.

It is worth noting that the ionizer generates a significant amount of heat. Under typical operating conditions, the valve body will often reach 160 °C within an hour or less of turning on the system. If a sample with a low melting point is being measured, a water cooled jacked must be used to maintain a lower sample temperature and prevent sample from clogging the valve mechanism.

2.2.2 Ion Packet Manipulation

Cold clusters pass on to the Wiley McLaren time-of-flight mass spectrometer[11] comprising three plates: the repeller, extractor, and ground. The repeller and extractor are pulsed from 0V to -2 kV

and ~1.5kV respectively. The extractor voltage may be adjusted to optimize ion steering but is generally most effective in the range -1.5kV-1.7kV. Ions of the same charge will separate by mass over a sufficiently long flight path when accelerated homogeneously. Ion arrival time can be calibrated to mass using ions known to form in the source region, e.g. I^- (mass 126.9 amu, arrival time ~32.5 μs relative to the Wiley McLaren pulse) or $I^- \cdot ICH_3$ (mass 268.9 amu, arrival time ~47 us). For the singly thionated uracils, the mass of the iodide nucleobase cluster is quite close to that of I_2^- making cluster selection somewhat challenging. Because the iodide nucleobase cluster is slightly higher in mass, the desired cluster arrives just slower to the detector; however, it may take multiple attempts to correctly isolate the species of interest. The two are readily differentiated by their photoelectron spectra once the UV pump pulse is introduced.

The cluster path is steered by two sets of deflector plate: one in the 1D pumped region, and one in the 2D region. The relative voltages of top/bottom and left/right plates are fine-tuned by maximizing ion signal at retractable multichannel plate (MCP) ion detector. Signal levels are particularly dependent on the voltages on the 2D deflector plates. Between the two sets of plates, a Einzel lens is used to improve the radial focusing of the ion packet, with a typical operating voltage of 450-700 V. After passing through the 2D deflector plates, the ion packet enters a re-referencing tube which also serves as a mass gate for cluster selection.[12] During initial ion optimization, the re-referencing tube is held at constant ground, allowing all ions to experience field free flight to the retractable ion detector. After the initial ion alignment, the mass gate will be turned on, with a voltage of -4kV pulsing to ground only at the correct time for the cluster of interest to pass through to the interaction region. When the voltage is at -4kV, anions are repelled, preventing them from entering the detection region. Proper ion alignment and mass gate timing should allow the species of interest to be cleanly isolated.

2.2.3 Timing

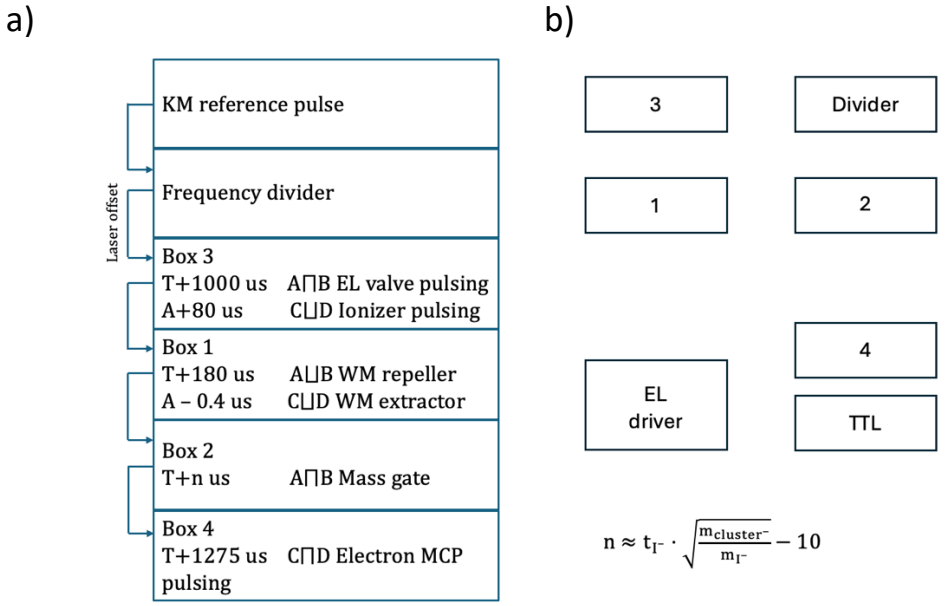

Figure 2.2: Schematic of the triggering scheme, including the outputs and delays associated with each timing box (a) and the relative positioning of the boxes in the electrical rack (b).

The apparatus requires that many pulsed voltage events occur at precise intervals relative to each other and that the ion packet arrives at the interaction region at the same time as the appropriate laser pulses. In order to achieve this, a 1kHz pulse generated by the laser is used to trigger all subsequent events, as shown in the timing diagram Figure 2.2.

EL valve cluster formation is most stable and efficient operating at 500 Hz, so the frequency of the trigger pulse must halved. The "reference" BNC output from the KM laser is passed to a Stanford Research Systems Model DG535 timing box, generating a TTL pulse at 2 V. A DEI PDG-2510 pulse divider/generator box is used for the frequency reduction, and the output used to trigger the first in a series of Stanford timing boxes controlling the timing of various pulsed events in ion cluster generation. The triggering of this box can be switched to internal for ion alignment but must be set to external to see photoelectron signal.

External triggering of the Stanford boxes may be disrupted for several reasons. First, the KM Griffin oscillator is not modelocked. Second, the oscillator is modelocked, but the photodiode used to monitor the oscillator is misaligned. This can be recognized by the KM software displaying an "Actual PRF" value other than 1.0. Third, the trigger or output voltage of the TTL generating Stanford box may be set incorrectly.

Ion alignment and optimization can be achieved with box 3 set to internal triggering at 500 Hz. Timing parameters for ionization and acceleration should be determined first with the mass gate voltage at 0 V. The timing on box 2 (mass gating) can be optimized as this voltage is turned

up. The correct mass peak should be isolated cleanly, with the temporal position of the peak shifting down slightly as the voltage is turned up. The timing between the cluster generation and laser pulses is found last by changing the triggering of box 3 from internal to external and varying the offset value A (laser offset). Correct timing between ions and pulses should result in an additional peak on the oscilloscope corresponding to the photoelectrons.

2.3 Laser Pulse Generation and Manipulation

Laser pulses are generated by a KM Griffin oscillator and KM Dragon amplifier. The output of the KM laser system can be manipulated to obtain desired pulse energies by non-linear crystal or optical parametric amplifier system. The laser system requires careful maintenance for its optimized output. More complete system and alignment details are available in the maintenance binder for the laser, but theoretical underpinnings and practical advice will be included here.

2.3.1 Oscillator

The KM Griffin oscillator is pumped by a Coherent Verdi 5 W diode pumped Nd:YVO4 outputting 4.3 W of continuous wave light at 532 nm. The pump light is periscoped up to the Griffin setup, rotating the polarization of the light from S to P polarized and leveling the beam to the requisite 84 mm beam height. The height of the beam is extremely sensitive, and the first steering mirror should NOT be adjusted except by a laser technician. From here the beam is steered into a Titanium:Sapphire (Ti:Sapph) crystal and through glass prisms to generate ~30 fs pulses at 80-90 MHz. Proper alignment of the retroreflector and output coupler should result in 800 mW of CW light when the translation of the back cavity mirror is set to CW mode (5.0 mm on the micrometer). As the back mirror is translated in, the CW power will drop and the beam profile will elongate. The power will often fluctuate by tens of mW as the proper cavity length is reached. It is possible to modelock the system using the KM software or by physically jostling the second prism. The modelocked spectrum should have a width of 50nm or greater and be centered at 790-800nm. The prisms can be adjusted using the software program to optimize the modelocked spectrum. The modelocked power should be noticeably higher than the CW power, with a differential of 50 mW or more being desirable for long-term modelocking stability. Adjustment of the second cavity mirror is generally the most important parameter in adjusting this power difference.

2.3.2 Stretcher

In the previous layout of the stretcher, a back reflection from the amplifier would occasionally counterpropagate to the oscillator, breaking modelocking and triggering an interlock that turned the laser off. A Faraday isolator and polarizer have been added to the beam line between the oscillator and stretcher to ensure that the beam can only pass in one direction.

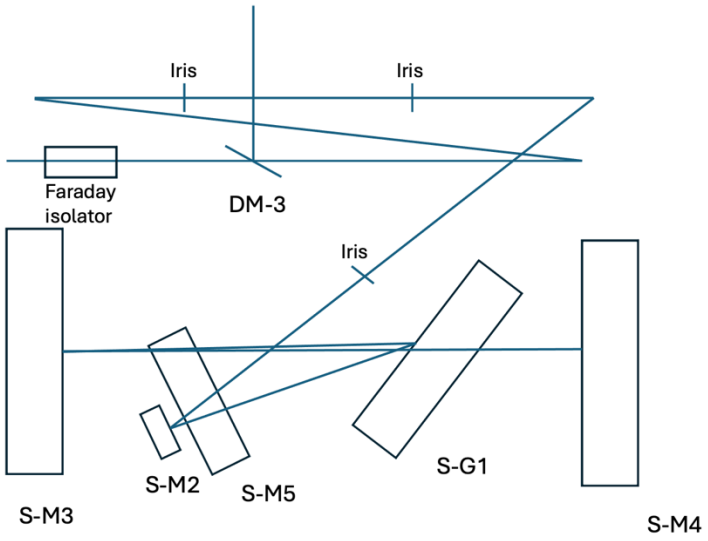

Figure 2.3: Schematic of the stretcher for the KM Dragon

The pulse train from the oscillator cannot be sent directly to the amplifier; the pulses must be stretched temporally to prevent damage to the amplifier optics, and the repetition must be cut down to a usable frequency. The stretcher (Figure 2.3) accomplishes the first of these by applying a positive temporal chirp. The beam is directed onto a diffraction grading, providing spatial separation of pulse wavelengths such that such that the redder frequencies have a shorter path length than the bluer frequencies as the pulse is reflected by an angled surface. S-M4 is a fold mirror, so the stretching is accomplished with a single grating and a single focusing optic (curved mirror S-M3), rather than the two grating and lenses required in the traditional stretcher layout. The output of the stretcher is several orders of magnitude longer than the input (estimated hundreds of ps vs tens of fs). The power efficiency through the stretcher should be above 40%.

Typical alignment can be accomplished by adjusting the peripheral mirrors without adjusting the optics in the stretcher itself. The beam should be aligned into the stretcher so that the beam passes through the series of irises along this path. The stretched beam will return along the same path, offset vertically by a few millimeters. It should be possible to align the stretched beam to pass through the irises when they are fully open and onto mirror D-M3 without clipping only by iterating adjustment of the mirrors directing the beam into the stretcher.

2.3.3 Pockels Cell

Pulse picking is accomplished via polarization manipulation. The pulse train going into the Pockels cell is horizontally polarized, and a vertical polarizer is placed afterward to filter out light with unmanipulated polarization. When the Pockels cell is on, it rotates the polarization by 90 degrees, effectively acting as a halfwave plate for certain pulses. The Pockels cell can be set to the desired repetition rate (in this case 1 kHz) to achieve a seed pulse train with vertical polarization.

During alignment, a removable waveplate may be inserted to the beam, “defeating” the Pockels cell.

2.3.4 Amplifier

Amplification by the KM Dragon is accomplished by a multi-pass amplification ring (Figure 2.4). The beam is directed through a cryogenically cooled Ti:Sapph crystal kept under low pressure by an ion pump. If the multi-pass is properly aligned, all 12 passes will be overlapped on the TiSapph crystal and pass through the holes of a mask. It should generally be possible to achieve this by iterative adjustment of half-moon mirror A-M7 and the large mirror A-M8. The 13th pass is picked off by the micrometer-stage-mounted mirror A-M9, then telescoped up in size before entering the compressor. The seed pulse power should be >10 mW at the Dragon output with the Pockels Cell defeated.

The Ti:Sapph amplification is driven by a 532 or 534 nm pulsed pump laser. Until 2020, the pump laser was a Lee Laser Nd:YAG 2nd harmonic laser. However, failure of the diode necessitated replacement of the pump laser. An Evolution 30 Nd:YLF 2nd harmonic laser was swapped in, necessitating reworking of the telescoping and focusing optics of the pump laser line. The laser output is expanded to the largest size that will fit on the 1” periscoping mirrors with a -75mm lens, then collimated with a 300 mm lens. A series of mirrors direct the beam onto the Dragon’s Ti:Sapph crystal, and the pump beam is focused nearly onto the crystal by a 400mm lens on a translatable stage. The focus of the pump beam onto the amplification crystal is extremely important and very sensitive. Optimal focusing may place the tightest focal spot just before the

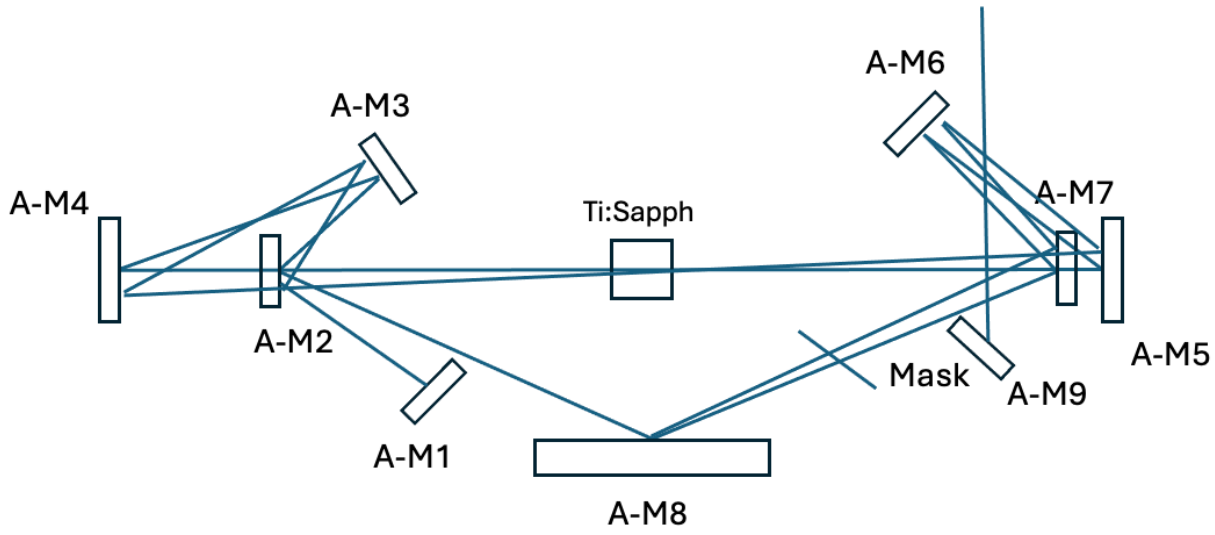

Figure 2.4: Schematic of the muti-pass amplification ring of the KM Dragon

crystal, so the positioning of the final focusing optic must be done by the translation stage's micrometer while monitoring the amplified power. The Evolution output power has since dropped due to a burn on the LBO crystal, so the pump laser would need to be replaced again for the KM laser setup to obtain the output power needed for the TRPES experiment.

2.3.5 Compressor

The compressor applies a negative temporal chirp to the beam using a parallel gratings C-G1 and C-G2 and should have a power efficiency of ~60%. A visible defect is visible on C-G2 which has lowered this efficiency in the past. This defect has previously been mostly deposited debris, as opposed to permanent damage to the grating. When the power output drops, it is possible to wash the grating with high purity water and methanol. To do so, one removes the grating from its mount and runs a gentle stream of each solvent in turn DOWN the face of the grating. The grating should be held at an angle of ~10° offset from normal during this process, and great care should be taken to stream the solvent parallel to the grating ridges (vertical when the grating is in place in the compressor) and to rapidly dry the grating with a gentle stream of clean N_2. The grating positioning can be reoptimized without total realignment of the compressor by carefully noting the position of the KM output before removing the grating and adjusting the compressor angle so the beam path matches with the grating is replaced. Minor compressor adjustments (on the level typical for the compressor) may be necessary. This process will only restore compressor efficiency a few times before grating damage becomes severe enough to necessitate replacing the grating entirely; however, the cleaning process can significantly increase the lifetime of the gratings.

The final output of the KM Dragon should be 1.6–1.9 mJ, 35 fs pulses at 1kHz repetition rate centered at 790-800 nm. Compressor grating C-G1, labeled in Figure 2.5, can be translated by a micrometer on the bottom of the mount to optimize the pulse duration.

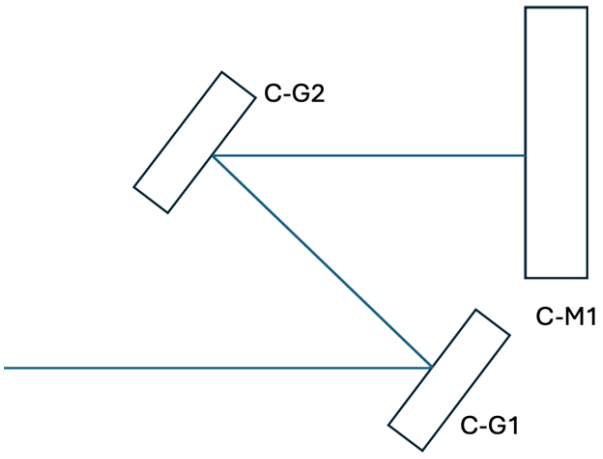

Figure 2.5: Schematic of the KM Dragon compressor

2.3.6 Pulse Characterization

The output of the KM Dragon can be characterized using a Swamp Optics Near-IR 8-20-USB GRENOUILLE (GRating-Eliminated No-nonsense Observation of Ultrafast Incident Laser Light E-fields). The Grenoille[13] utilizes a Frequency-Resolved Optical Grating (FROG) technique as opposed to autocorrelation. In both FROG and autocorrelation measurements, the beam is split and focused onto a second harmonic generation crystal. By varying the relative path lengths of split beams and measuring the intensity of the second harmonic at different delays, a temporal profile of the laser output can be obtained. FROG measurements add a second dimension to this measurement by spectrally resolving the second harmonic light, enabling the unambiguous determination of pulse duration by matching the measured 2D intensity plot with a retrieved plot corresponding to particular pulse frequency and duration. The Grenoille is a variant of a FROG which uses a Fresnel bi-prism in place of the beam splitter and delay state, and a thicker SHG crystal to achieve spectral resolution without a standard spectrometer.[13, 14]

When using the Grenoille to characterize the KM output, it is necessary to use a beam splitter, window wedge, and/or ND filters to decrease the beam intensity, as the full intensity of the KM Dragon output is sufficient to damage the optics of the Grenoille. The software associated with the Grenoille, QuickFrog by Femtosoft Technologies, displays the saturation of the camera and can be used to adjust the ND filter. The intensity should be at the higher end of the permissible intensity, represented by three green bars in the software. The beam must be carefully aligned into the Grenoille using the spatial mode, which is selected in the software and by the output connection used. The beam should be well centered on the input iris and on the camera as shown in the software. The iris should not be closed to a small diameter during pulse characterization, as this can impact the accuracy of the retrieved pulse width. With the beam centered, the output cable can be moved to the temporal output port and the software can be switched into temporal mode. The software will return the temporal and spectral characteristics associated with the retrieved 2D plot.

2.3.6 Generation of experimental laser energies

A 50/50 beam splitter sends half the beam intensity to form the pump pulse and half for the probe pulse. For many pump energies, the beam is steered to a TOPAS-C optical parametric amplifier to generate tunable visible light which is subsequently frequency doubled to generate UV wavelengths. Alternatively, UV light of approximately 4.7 eV can be generated by frequency tripling of the fundamental by a series of β-barium borate (BBO) crystals.

The TOPAS-C optical parametric amplifier uses a portion of the KM output beam to generate a tunable visible light output. The major paths in OPA setup are shown superimposed on an image of the TOPAS-C in Figure 2.6. Within the TOPAS, 97.5% of the beam is diverted to form a pump beam (red path E), and 2.5% to the low power seed arm used to generate the signal frequency (paths A–D). 20% of the low power arm is passed through a variable filter to a motorized stage (B), then through a sapphire plate to generate a white-light continuum. The white light continuum can be optimized using a variable filter placed just before the stage, but adjustment of iris 2 is

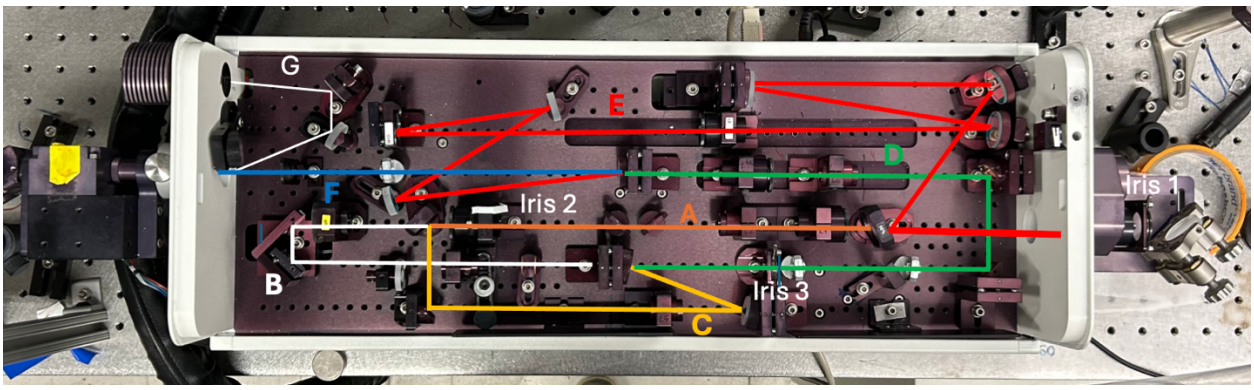

Figure 2.6: Schematic of the major beam lines of the TOPAS-C. Line A (orange) is the Line B (white) is the portion of the beam used for white light generation. Line C (yellow) is the portion of the signal line used to amplify the appropriate portion of the white light spectrum. Line D (green) is the combination of lines B and C, resulting in the signal frequency. Line E (red) is the pump line which overlaps with the signal line to form line F (blue) going into a nonlinear crystal. When excess pump light is not needed for final frequency generation, a dichroic mirror is flipped in front of the TOPAS-C output and the dump beam follows path G (white).

generally more effective in achieving a nice final beam profile. The white light is focused into a BBO non-linear crystal, where it is combined non-colinearly with the 80% power from arm C. This results in an IR signal frequency and excess pump frequency separated angularly, as well as second order frequencies when the first motorized stage and BBO angle are at their initial optimized position.

The pump beam, arm E, is reflected in a z pattern to match the lengths of the other arms. The pump beam is telescoped down to combine with the seed line in a second BBO crystal for parametric amplification. Near-VDE excitation of the iodide nucleobase clusters is best achieved using the idler and pump sum frequency (SFI) mode. However, the low energy excitation pulses used to measure I^-·4TU fall outside of the energy range accessible with SFI. The TOPAS must instead be run in second harmonic of the signal (SHS), which results in an output polarization rotated 90 degrees compared to SFI output. This rotation can be corrected with a half-wave plate or by adding an extra mirror to the periscope. The optimized telescoping of the pump beam is slightly different for SFI and SHS operation, so the second telescoping lens along path E will need to be repositioned to optimize output power when switching operating mode. The mixer module on the output must also be rotated by 90°.

In order to achieve the final tunable UV pump, the TOPAS-C output passes through a BBO crystal to double the beam frequency. Given the range of pump energies used (3.8 eV-4.7 eV or 350 nm-260 nm), it may sometimes be necessary to replace the high reflectivity mirrors of the periscope to be appropriate with the particular pump energy in use.

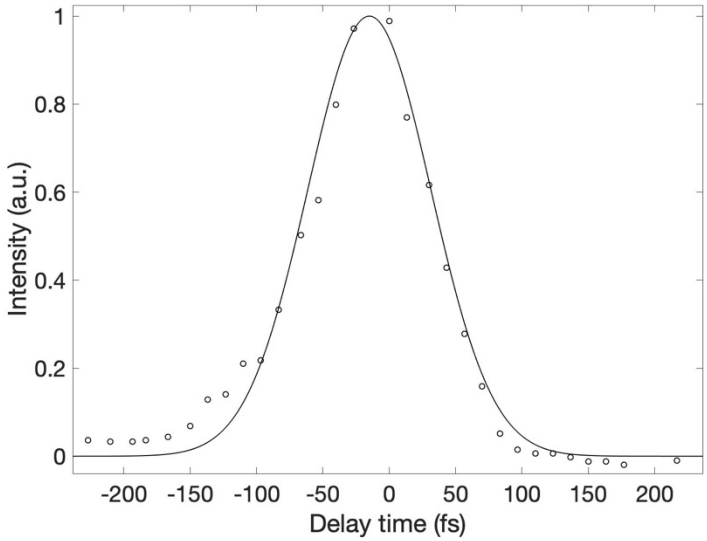

Figure 2.7: Intensity of SFG pulse from 1.55 eV and 4.35 eV pulses. The value of σ from this Gaussian fit (65 fs) corresponds to a FWHM of 150 fs in vacuum**.**

2.3.7 Cross-correlation

Cross correlation may be used to determine the temporal resolution of the experiment. The pump and probe pulse are overlapped spatially in an appropriate sum frequency generation (SFG) BBO crystal. A wedge is used to separate the summed and input frequencies, and the intensity of the summed signal measured as the time delay between pump and probe is changed. The plot of the intensity should have an essentially Gaussian shape, and fitting of this data enables one to retrieve the pulse width σ for the experimental setup. Data from a sample cross-correlation measurement are included as Figure 2.7.

2.4 Electron Detection by Velocity Map Imaging

The electron kinetic energy spectra are collected by velocity map imaging (VMI) apparatus. The VMI, first developed by Parker and coworkers,[15, 16] applies a constant, inhomogeneous electric field within the detection region to map the velocity vectors of negatively charged particles to distinct positions on a 2-dimensional detector. In instruments utilizing gridded electrodes, this image can be "blurred" due to variation in the initial position of charged particles relative to the ion lens axis. Correct operation of a VMI apparatus significantly improves the quality of the raw image, as all charged particles with the same velocity vector are imaged to the same position on the detector regardless of position in the x-y plane.

The apparatus consists of three open ring ion lenses set to repeller, extractor, and ground voltages (similar to the Wiley McLaren, see Figure 2.8). The resolution of the VMI image is optimized with a ratio of repeller and extractor voltages of approximately 0.70. Within our setup,

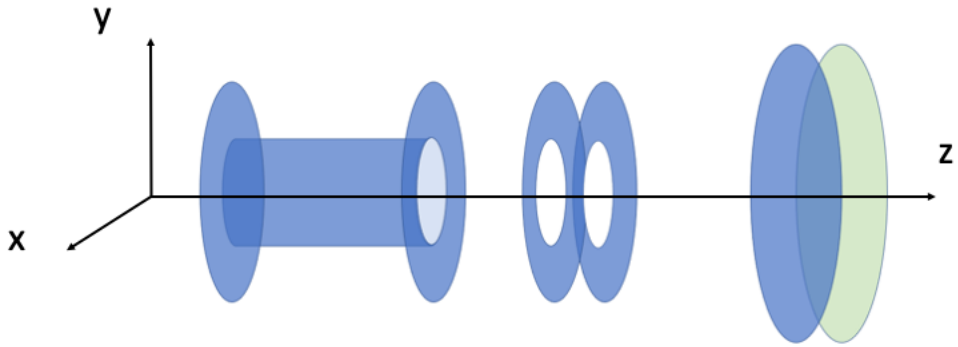

Figure 2.8: Schematic of the VMI apparatus and phosphor screen detector

the repeller plate is also the end of the re-referencing tube and is set to -4 kV and the extractor plate is set to -2811 V to obtain the desirable voltage ratio. Each plate is separated from the previous by 1.5 cm. The final positional detector, placed 60 cm from the interaction region (between the repeller and extractor plates), consists of two 70mm chevron stacked MCP plates coupled to a phosphor screen.

The voltages of the repeller and extractor plate will determine the magnification of the image on the detector and therefore the detectable range of electron kinetic energies. The regular operating voltages for the VMI setup are chosen so that ions of different mass are cleanly isolated and electrons with a few eV of kinetic energy are imaged.

The VMI assembly images all negatively charged particles passing through the instrument, but the signal from photoelectrons is of primary interest. Given the difference in mass and therefore flight time for electrons and atomic or molecular ions, signals from these species may be deconvoluted by amplifying the signal at the phosphor screen assembly only at particular times relative to the laser pulses. To this end, the voltage applied to the front imaging MCP is pulsed with the second MCP held at ~1.6 kV and the phosphor screen held at ~4 kV, with the precise voltages adjusted to obtain the best possible image. In general, the front MCP is held at 700 V and the signal amplification is minimal. As photoelectrons arrive at the detector, the voltage on the front MCP drops to ground, increasing the voltage differential across the MCPs and therefore the signal amplification.

Electrons impinging on the detector at the correct arrival time will generate an amplified signal via the MCP plates which causes phosphorescence of the phosphor screen. The image on the phosphor screen is captured by a charge-coupled device (CCD) camera and read by a LabView data acquisition program on a laboratory computer. An electron kinetic energy spectrum can be generated using Basis Set Expansion (BASEX)[17] reconstruction methods and the photoelectron angular distribution by Polar Onion Peeling (POP).[18, 19] Details of the implementation of this software is described in the theses of Margaret Yandell[20] and Sarah King.[21]

The energies imaged by the VMI can be calibrated by the two lowest energy spin-orbit states of I^-. The known binding energies are 3.06 eV for the $^2P_{3/2}$ state[22] with a spin-orbit splitting for $^2P_{1/2}$ state of 0.94 eV (or 4.00 eV).[23]

References

1. M. T. Zanni, *Photodissociation and charge transfer dynamics of negative ions studied with femtosecond photoelectron spectroscopy*. (University of California, Berkeley, 1999).
2. B. J. Greenblatt, *Femtosecond photoelectron spectroscopy: a new tool for the study of anion dynamics*. (University of California, Berkeley, 1999).
3. A. V. Davis, *Time-resolved phototelectron spectroscopy and imaging studies of anion dynamics*. (University of California, Berkeley, 2002).
4. A. E. Bragg, *Excited-state dynamics of molecular and cluster anions studied with time-resolved photoelectron spectroscopy and imaging*. (University of California, Berkeley, 2004).
5. A. V. Davis, R. Wester, A. E. Bragg and D. M. Neumark, The Journal of Chemical Physics **118** (3), 999-1002 (2003).
6. A. E. Bragg, J. R. R. Verlet, A. Kammrath, O. Cheshnovsky and D. M. Neumark, Journal of the American Chemical Society **127** (43), 15283-15295 (2005).
7. U. Even, J. Jortner, D. Noy, N. Lavie and C. Cossart-Magos, The Journal of Chemical Physics **112** (18), 8068-8071 (2000).
8. S. Y. T. van de Meerakker, H. L. Bethlem and G. Meijer, Nature Physics **4** (8), 595-602 (2008).
9. A. Amirav, U. Even and J. Jortner, Chemical Physics **51** (1-2), 31-42 (1980).
10. J. M. Hayes and G. J. Small, Analytical Chemistry **55** (4), 565A-574A (1983).
11. W. Wiley and I. H. McLaren, Rev. Sci. Instrum. **26** (12), 1150–1157 (1955).
12. L. A. Posey, M. J. Deluca and M. A. Johnson, Chemical Physics Letters **131** (3), 170-174 (1986).
13. S. Akturk, M. Kimmel, P. O'Shea and R. Trebino, Opt. Express **11** (1), 68-78 (2003).
14. P. O'Shea and R. Trebino, presented at the Ultrafast Phenomena, Charleston, South Carolina, 2000 (unpublished).
15. A. T. J. B. Eppink and D. H. Parker, Review of Scientific Instruments **68** (9), 3477-3484 (1997).
16. D. H. Parker and A. T. J. B. Eppink, The Journal of Chemical Physics **107** (7), 2357-2362 (1997).
17. V. Dribinski, A. Ossadtchi, V. A. Mandelshtam and H. Reisler, Rev. Sci. Instrum. **73** (7), 2634–2642 (2002).
18. C. Bordas, F. Paulig, H. Helm and D. Huestis, Review of scientific instruments **67** (6), 2257-2268 (1996).
19. G. Roberts, J. Nixon, J. Lecointre, E. Wrede and J. Verlet, Review of Scientific Instruments **80** (5) (2009).
20. M. A. Yandell, *Charge accommodation dynamics of cluster and molecular anions produced by photo-initiated intracluster charge transfer*. (University of California, Berkeley, 2014).
21. S. B. King, *Time-resolved radiation chemistry: dynamics of electron attachment to nucleobases and small molecules*. (University of California, Berkeley, 2015).
22. R. J. Peláez, C. Blondel, C. Delsart and C. Drag, J. Phys. B: At. Mol. Opt. Phys. **42**, 125001 (2009).
23. C. E. Moore, *Atomic energy levels as derived from the analyses of optical spectra*. (US Department of Commerce, National Bureau of Standards, 1949).

Chapter 3

Electron transfer dynamics of iodide-2-thiouracil clusters

Adapted from M. Koga, M. Asplund, and D. M. Neumark, "Electron attachment dynamics following UV excitation of iodide-2-thiouracil complexes", J. Chem. Phys. 156, 244302 (2022)

3.1 Abstract

The dynamics of low energy electron attachment to the thio-substituted uracil analog 2-thiouracil are investigated using time-resolved photoelectron spectroscopy (TRPES) of iodide·2-thiouracil (I –·2TU) binary clusters. In these experiments, the anions are excited at pump energies of 4.16 and 4.73 eV, and the ensuing dynamics are probed by photodetachment at 1.59 and 3.18 eV. Upon excitation near the vertical detachment energy (4.16 eV), dipole bound (DB) and valence bound (VB) anion signals appear almost instantaneously, and the DB state of the 2TU anion undergoes ultrafast decay (~50 fs). At 4.73 eV, there is no evidence for a DB state, but features attributed to two VB states are seen. The transient negative ions formed by photoexcitation decay by autodetachment and I– fragmentation. The I– dissociation rates and their dependence on excitation energy agree reasonably well with Rice-Ramsperger-Kassel-Marcus calculations. Notable differences with respect to TRPES of the related iodide-uracil anion are observed and discussed.

3.2 Introduction

The role of radiation in causing DNA strand cleavage has long been known, and in the past few decades it has become clear that indirect interactions via low-energy electrons (LEEs) contribute significantly to this process.[1] During electron capture, an excess electron can occupy an unoccupied valence orbital of a nucleobase to form a valence-bound (VB) anionic state, but it can also be captured by a sufficiently large dipole moment on the base to form a diffuse dipole-bound (DB) state.[2] This DB state is proposed to serve as a "doorway" to electron capture.[3, 4] However, since the interaction of LEEs with nucleobases is diffusion-controlled in the condensed phase, the primary processes of electron attachment at the moment of electron capture have been difficult to characterize.

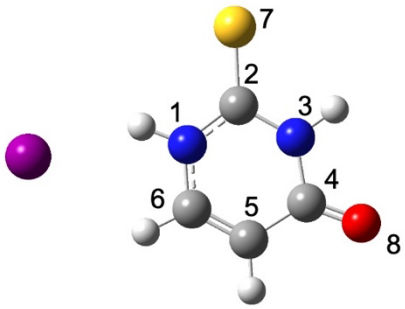

Figure 3.1: Ground-state structure of the iodide-2TU cluster obtained at MP2/aug-cc-pVDZ(-pp) level of theory. Atom numbering of 2TU is also shown.

To elucidate the dynamics of electron capture of nucleobases in the gas phase, we have previously studied the photoinduced dynamics of iodide-nucleobase cluster anions,[5] such as I^-·thymine[6-8], I^-·adenine[9], I^-·uracil[6, 8, 10, 11], and I^-·uracil·H_2O[12, 13] by means of femtosecond time-resolved photoelectron spectroscopy (TRPES).[14] In these experiments, an ultraviolet pump pulse photoexcites the complex, triggering electron transfer from the iodide to the nucleobase and forming a transient negative ion (TNI) whose dynamics can be probed by a second laser pulse that induces photodetachment. Complementary experiments on the photodepletion of several of these species have been carried out by Dessent and co-workers.[15-17]

The nature and dynamics of the TNI depend on the energy of the excitation pulse. In the I^-·uracil (I^-·U) cluster, which is one of the more intensively investigated systems, excitation near the vertical detachment energy (VDE) gives rise to both DB and VB states immediately after photoexcitation. The appearance timescales of these TNIs suggest partial DB → VB conversion on a timescale ca. 200 fs. The partial conversion reflects the fact that in uracil, the DB anion is slightly lower in energy than the VB anion.[18, 19] Moreover, different dynamics are observed when I^-·U is excited around 4.7 eV, which is well above the cluster VDE. In this case, the VB state is generated immediately and there is no evidence for the formation of the DB state.[11, 13] Quantum chemical calculations suggest that the oscillator strength for optical charge transfer of the excess electron of I^- to the vacant π* orbital of the nucleobase is negligibly small at this excitation energy; it was thus proposed that ultrafast population of the VB state of the nucleobase arises $\pi\pi^*$ excitation of the nucleobase followed by charge transfer from the I^-.[11] A global discussion of the excitation and decay mechanisms of iodide-nucleobase complexes was presented by Kunin et al,[5] but several open questions remain.

In this study, we carry out TRPES experiments on the I^-·2TU cluster (Figure 3.1), replacing uracil with 2-thiouracil (2TU) in which the oxygen bonded to carbon C2 is substituted with sulfur. Thiosubstituted nucleobases play essential roles in medical applications, especially in light and radiation chemotherapy, so understanding electron capture dynamics of these species is desirable.[20-23] Dessent[24] has investigated the one-photon photodepletion and photofragmentation spectra of I^-·2TU and finds that it exhibits two pronounced features: a distinct peak at 4.1 eV and

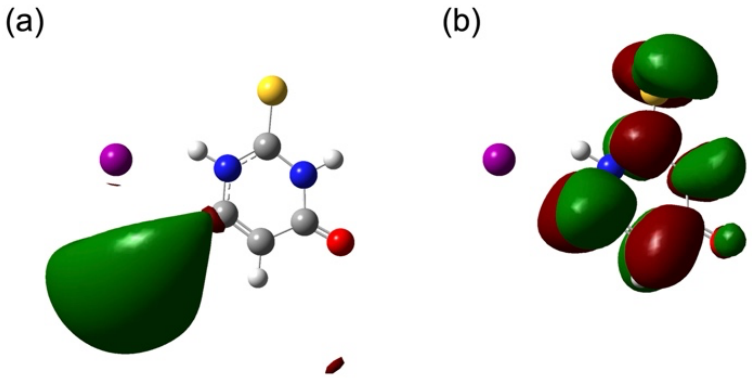

Figure 3.2: Schematic of singly occupied orbitals of (a) DB state and (b) VB state of 2TU anion in I^-2TU.

Table 1. Adiabatic and vertical electron affinities (AEA, VEA) of U and 2TU anions (in meV)

	DB state	**VB state**	
Species	AEA	AEA	VEA
U[a]	93	40	-572
2TU[b]	---	174	-173

[a] ref 18,19, [b] ref 29

a rather flat region above 4.6 eV. The peak at 4.1 eV was assigned to a charge transfer transition from iodide to a diffuse DB orbital of 2TU (Figure 3.2a), as had been seen in I^-·U. Excitation at >4.6 eV was attributed to a combination of direct detachment and a $\pi\pi^*$ transition localized on the thiouracil, an assignment consistent with the electronic spectroscopy of this species.[25] Other relevant experiments include measurements of dissociative electron attachment to 2TU[26, 27] and anion photoelectron spectroscopy of the related species $4TU^-$ and $2,4TU^-$.[28]

Ortiz and co-workers[29] have carried out electronic structure calculations on $2TU^-$, obtaining results for the adiabatic (AEA) and vertical (VEA) electron affinities for 2TU and the vertical detachment energy (VDE) of the anion; these values are 0.26, -0.17, and 0.71 eV, respectively. These numbers apply to the VB state of $2TU^-$ in which the lowest π^* orbital (Figure 3.2b) is occupied, although a DB state is also expected owing to the high dipole moment of 2TU (4.20 D). Since the diffuse electron in a DB state is typically bound by 0.1 eV or less, the calculations suggest that, in contrast to the uracil anion (see Table 1), the VB state of $2TU^-$ lies below its DB state. As a result, the dynamics of DB to VB conversion in photoexcited I^-·2TU might be expected to differ from those seen in I^-·U, motivating in part the work presented here.

The TRPES experiments on I^-·2TU described herein are carried out at two pump energies: 4.16 eV, which is near the VDE of the cluster, and 4.73 eV, which is in the range of one or more $\pi\pi^*$ transitions on the 2TU chromophore. As in previous studies, a 1.57 eV pulse is used as a probe for the observation of DB and VB state dynamics, and a 3.18 eV pulse probe for monitoring other transient species and products related to the deactivation of VBS. In particular, a 3.18 eV probe pulse enables electron photodetachment of dissociated iodide, which has an eBE of 3.06 eV and is expected to be one of the major products following UV irradiation.

Our experiments reveal rapid formation of DB and VB anions upon near VDE excitation. The DB state undergoes nearly complete ultrafast (<100 fs) conversion to the VB state and the resulting VB signal decays in ca. 10 ps. Excitation at 4.73 eV gives rise to the VB state and as well as a higher-lying π^* state that also plays a role in the TNI dynamics. Following excitation with either pump energy, I^- signal grows in within ~10 ps, which is notably faster than for other I^- nucleobases we have studied[11, 13] and in fact agrees with the calculated time scale for statistical dissociation of energized I^-·2TU). This agreement indicates that dissociation to I^- proceeds without the dynamic bottlenecks seen in previous systems.

3.3 Methods

Experimental The TRPES setup has been described in detail elsewhere.[14, 30, 31] Briefly, iodide-2 thiouracil clusters are formed by flowing 300 kPa of argon over a reservoir containing iodomethane and through a cartridge containing the solid 2-thiouracil sample (Aldrich >97%). This cartridge is housed within an Even-Lavie pulsed valve operating at 500 Hz and heated to 220º C to achieve volatilization. The pulsed valve produces a supersonic expansion of the gas mixture into vacuum that passes through a ring ionizer, generating charged species by secondary electron attachment. Ions are then extracted perpendicularly into a Wiley-McLaren mass spectrometer,[32] and iodide-2-thiouracil ion clusters are mass-selected for interaction with laser pulses.

TRPES employs a pump-probe scheme of femtosecond laser pulses to first excite the ion clusters and then photodetach electrons for detection. A laser system comprising a KM Griffin Oscillator and Dragon Amplifier operating at 1 kHz generates ~40 fs laser pulses centered at 780 nm (1.59 eV) with 2 mJ/pulse. To generate a pump pulse at 4.16 eV, a portion of this output is sent to a TOPAS-C optical parametric amplifier (OPA), which generates 596-nm light that is subsequently doubled in a beta-barium borate (BBO) crystal to form an excitation pulse at 298 nm (4.16 eV). Pump pulses at 4.73 eV are generated by frequency-tripling the 780 nm pulse. Two probing schemes are also employed, one using the fundamental of the output from the KM amplifier (1.59 eV), and the second utilizing a frequency doubled pulse at ~390 nm (3.18 eV).

Detached electrons are detected using a chevron mounted pair multi-channel plates coupled to a phosphor screen and imaged using a charge-coupled device (CCD) camera. The basis set expansion (BASEX) method was used to reconstruct the kinetic energies of the imaged photoelectrons.[33]

Computational The Gaussian 16 computing package[34] was used to generate the potential energy surface for the dissociation of $I^-\cdot 2TU$ to I^- + 2TU at the MP2 level with an augmented Dunning basis set aug-cc-pVDZ for C, H, O, and N, and an additional set of diffuse functions (aug-cc-pVDZ-pp) for I.[35] Geometry optimization and vibrational frequency calculations were performed as a function of I-N1 distance with steps of 0.25 Å far from the transition state, and 0.1 Å within 1 Å of the transition state. The resulting potential energy curve and geometries at several characteristic points are shown in Supporting Information (S.I.)

3.4 Results

Figure 3.3 shows one-photon photoelectron spectra of the $I^-\cdot 2TU$ binary complex recorded at photon energies of 4.16 and 4.73 eV. The spectrum taken at 4.73 eV has two prominent features. The peak at an electron kinetic energy (eKE) of ~0.62 eV arises from direct detachment to the $^2P_{3/2}$ spin-orbit state of complexed iodine and yields vertical detachment energy (VDE) of 4.11 eV (i.e. 4.73-0.62 eV) for the cluster. From this we can determine that solvation by 2TU stabilizes the I^- anion by about 1 eV, given that EA(I)=3.06 eV. This solvent shift is similar to that found for $I^-\cdot U$ complex.[8] The width of this peak is approximately 0.2 eV and is much broader than that of

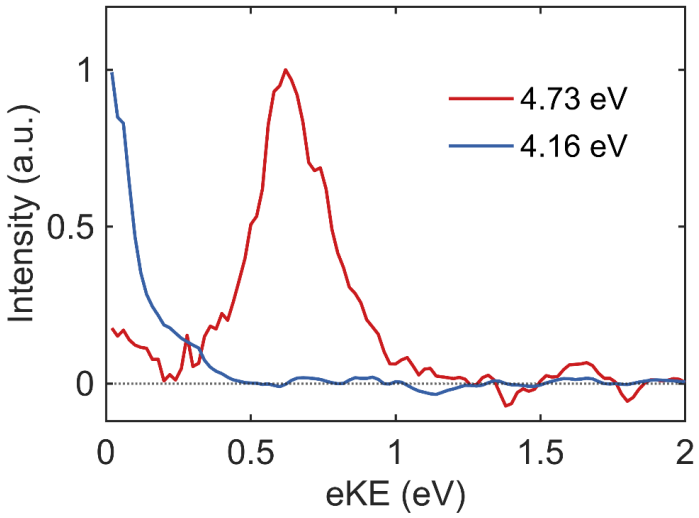

Figure 3.3: One photon photoelectron spectra of $I^-\cdot$2TU with the photon energies of 4.73 eV (red) and 4.16 eV (blue).

$I^-\cdot$U at the corresponding excitation energy.[11] This suggests a greater geometric displacement of the $I^-\cdot$2TU complex from the corresponding neutral species than for I^-U. The second, smaller feature of the photoelectron spectrum occurs at nearly zero kinetic energy, and is attributed to autodetachment from the transient negative ion, which is known to produce low energy electrons from these systems.[11-13, 36] The spectrum shows that direct detachment dominates at 4.73 eV, consistent with the results of Dessent.[24]

At. 4.16 eV, which lies just 50 meV above the VDE, only the ~0 eV feature is seen. Although it is tempting to ascribe all signal intensity to autodetachment, direct cluster detachment also leads to low kinetic energy electrons, so one cannot readily distinguish between electrons produced by the two mechanisms.

3.4.1 TRPES with the 1.59-eV probe

Figure 3.4 shows a contour plot of the TRPE spectrum of $I^-\cdot$2TU excited at 4.16 eV and detached with a 1.59 eV probe pulse. According to Dessent,[24] excitation at this energy accesses a DB state of the anion. This spectrum is plotted as a function of electron binding energy (eBE = hν – eKE). In Figure 3.4, two distinctive features appear immediately following excitation: a sharp peak centered at around 0.1 eV (feature A) and a broad signal with an intensity maximum at ~0.7 eV (feature B). Based on its low binding energy and narrow width, feature A is assigned to the DB transient negative ion.[10] Feature B, with a higher eBE and greater spectral breadth, is then attributable to signal from the VB transient negative ion. These assignments are in agreement with previous investigations of iodide-nucleobase complexes,[5] and with the theoretically predicted VDE of the VB canonical anion (0.71 eV).[29] Feature A decays within ~100 fs, losing its characteristic narrow shape. The broad feature B also appears rapidly following excitation, before

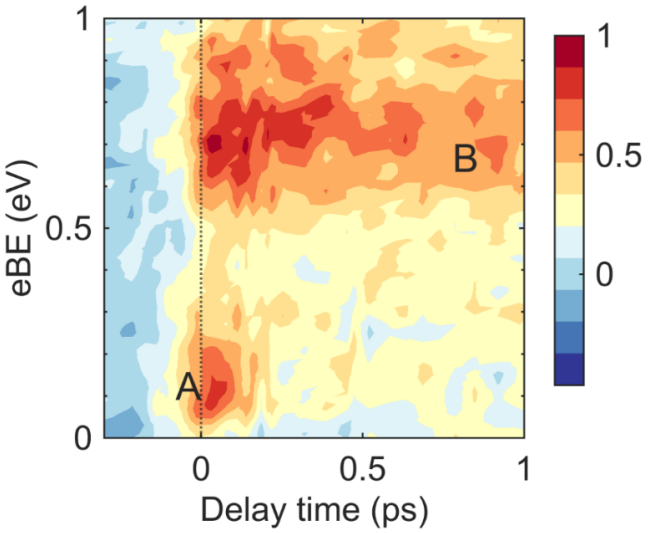

Figure 3.4: Contour plot of TRPE spectra of I^-·2TU with excitation and probe pulses of 4.16 eV and 1.59 eV, respectively

decaying within several picoseconds. The analysis in Section IV suggests that the persistent residual signal in the energy range of Feature A is from the low energy tail of feature B.

Figure 3.5 shows the TRPE spectrum for I^-·2TU excited at 4.73 eV and probed at 1.59 eV. Signal with eBE >0.85 eV is excluded from the figure because of large intensity fluctuations in the direct detachment signal caused by the pump pulse. In contrast to Figure 3.4, here there is no sharp, strong feature at around 0 eV. Instead, a broad feature is seen rapidly following photoexcitation, with the greatest intensity from 0.6 eV to 0.8 eV, a range very similar to that of the VB state observed with 4.16 eV excitation. This result strongly indicates that the DB state does not form at 4.73 eV but that the VB state is populated shortly after excitation, giving rise to the strong signal at around 0.7 eV (feature B). A second, relatively strong photoelectron feature is observable at 0-0.45 eV, especially at early time scales (feature B').

3.4.2 TRPES with the 3.18-eV probe

Figure 3.6 a and b show TRPE spectra probed by 3.18 eV. In each plot, the most prominent feature, feature C, is located at 3.06 eV and grows in intensity over tens of ps. Based on its binding energy and spectral shape, this feature is clearly from photodetachment of atomic iodide produced by photofragmentation of I–·2TU. In addition, Figure 3.6 b exhibits a broad and very weak feature D at 1.3-2.2 eV which appears within 1 ps and then slowly decays within ca. 10 ps leaving a small offset component at 60 ps. This feature is negligibly small in Figure 3.6 a.

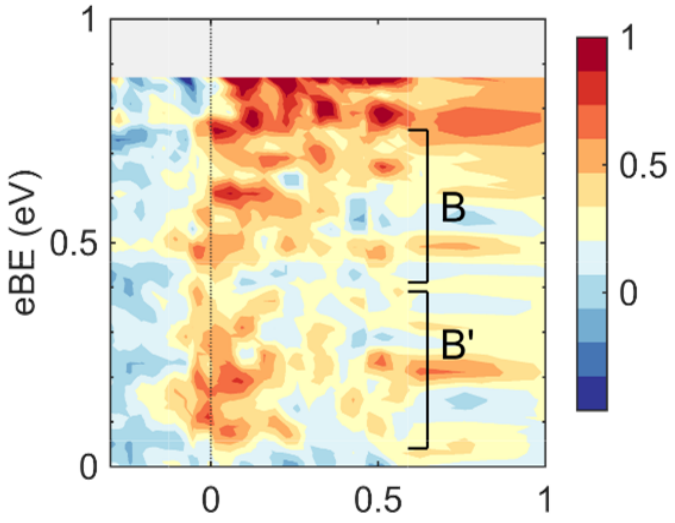

Figure 3.5: Contour plot of TRPE spectra of I^-·2TU at excitation and probe energies of 4.73 eV and 1.59 eV.

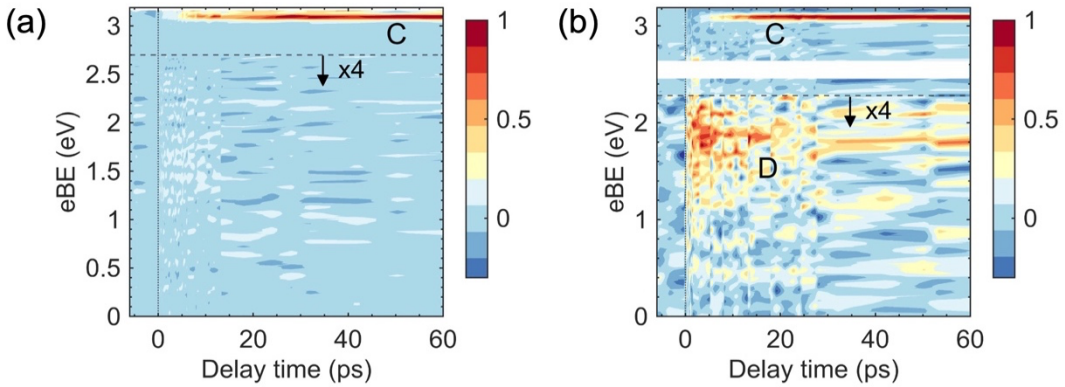

Figure 3.6: Contour plots of TRPE spectra of I^-·2TU photodetached by 3.18 eV with excitation energies of (a) 4.16 eV and (b) 4.73 eV. The signal intensities below 2.7 eV in (a) and 2.28 eV in (b) are magnified by a factor of 4.

3.5 Analysis

To gain a more quantitative understanding of our results, the signal intensity of each feature in Figures 3.4-3.6 is integrated over a specified eBE range (see Tables 2 and 3) for each pump-probe delay. Results for pump energies of 4.16 and 4.73 eV are shown in Figures 3.7 and 3.8, respectively, for a probe energy of 1.59 eV. As in previous work, these time-dependent integrated distributions

are fit to the convolution of a Gaussian experimental response function with a sum of exponential functions using Eq. (1).

$$I(t) = \frac{1}{\sigma_{CC}\sqrt{2\pi}} \exp\left(-\frac{t^2}{2\sigma_{CC}^2}\right) \cdot \begin{cases} I_0\,, & t < 0 \\ I_0 + \sum_i A_i \exp\left(\frac{-t}{\tau_i}\right), & t \geq 0 \end{cases} \quad (1)$$

I_0 represents a constant offset, and the dot indicates convolution over time. σ_{CC} is the Gaussian cross correlation width of pump and probe pulses, determined to be 72 fs for 4.16 eV excitation and 70 fs for 4.73 eV. The free parameters of the fit are A_i and τ_i, the amplitudes and the time constants of the decays, respectively.

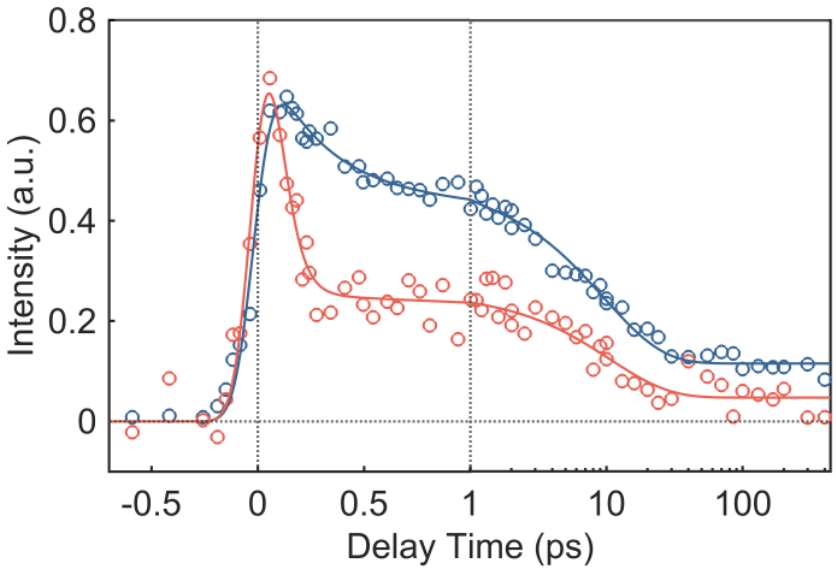

Figure 3.7: Time evolution of the photoelectron intensity of feature A (red) and feature B (blue) as open circles. The time axis is linear up to 1ps and logarithmic afterward. The results of the convolution fittings are also displayed as solid lines.

Table 2. Fit parameters that reproduce the time evolution in Figure 3.8

	eBE (eV)	τ_1 (fs)	τ_2 (ps)	A_1	A_2
Feature A	0 – 0.20	55 ± 25	10.6 ± 4.4	0.89[a]	0.11
Feature B	0.5 – 1.0	260 ± 90	9.6 ± 1.5	0.46	0.54

[a] All amplitudes shown here are normalized by the sum of the decay amplitudes.

The integrated signals and fits for the data in Figure 3.4 are shown in Figure 3.8, and the fit parameters are shown in Table 2. With these values, Eq (1) accurately reproduces the time evolution of both features. The rise times of features A and B lie within the instrumental response function, and both features then undergo bi-exponential decay. Most of feature A decays with a time constant of 55 fs. The faster decay of feature B is slower than this (260 fs), while the slower time constants for the two features are both around 10 ps, and there is a nonzero offset that extends beyond 400 ps. A preliminary interpretation of these results, discussed in more detail in Section V, is that the DB state (feature A) decays to the VB state on a 55 fs time scale, and much of the VB state subsequently decays within 10 ps. The VB feature is quite broad and probably extends into the energy range of feature A, which is why both features exhibit the same 10 ps decay.

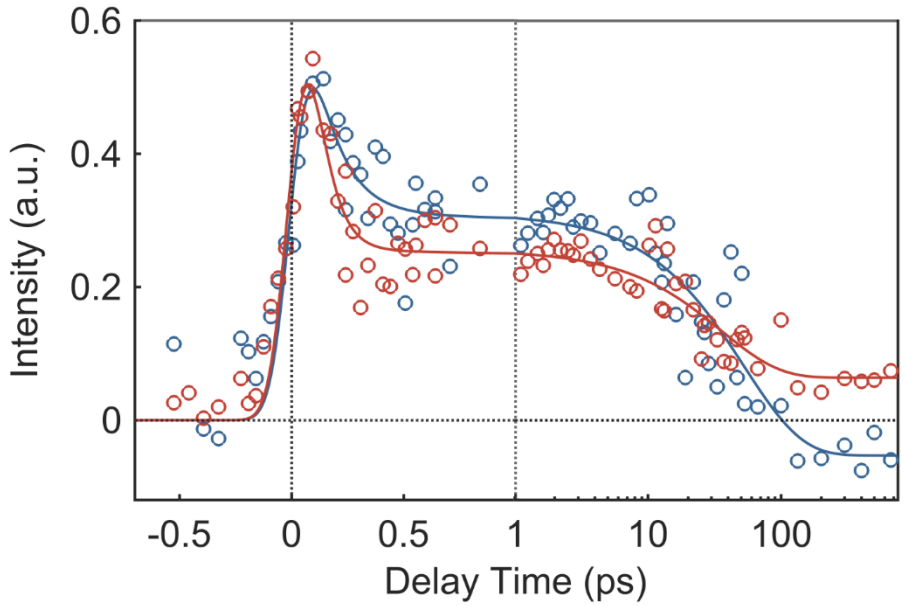

Figure 3.8: Time evolution of integrated signal intensities of feature B (blue) and B' (red) in the TRPE spectra with 4.73 eV excitation.

Table 3. Time constants necessary to reproduce the time evolution in Figure 3.8.

	eBE (eV)	τ_1 (fs)	τ_2 (ps)	A_1	A_2
Feature B'	0 – 0.4	70 ± 20	35.6 ± 15.5	0.84[a]	0.16
Feature B	0.4 – 0.75	125 ± 65	52.8 ± 19.5	0.58	0.42

[a] All amplitudes shown here are normalized by the sum of the decay amplitudes.

At 4.73 eV excitation, the broad signal in Figure 3.5 is divided into two regions, 0.4 – 0.75 eV (feature B) and 0 – 0.4 eV (feature B'). As discussed previously, the breadth and binding energy of both features suggest that they correspond to VB anion states. Their time evolution together with the curve fitting results by Eq. (1), are plotted in Figure 3.8, and the time constants required to reproduce the data are displayed in Table 3.

Both features exhibit rise times within the IRF followed by biexponential decay. The fast decay constants for features B and B' are 125 and 70 fs, respectively, lying between the values of the faster time constants for features A and B in Table 2. On the other hand, the slower time constants of 53 and 36 ps for B and B', respectively, are considerably larger than the 10 ps long-time decays for features A and B at 4.16 eV excitation. The decay channels responsible for these dynamics are discussed in Section 3.6.

Additional insight into the decay dynamics is provided by the 3.18 eV probe. Figure 3.9 shows the time evolution of feature C at both pump energies as well as feature D with 4.73 eV excitation. The timescales of these curves are analyzed with a sum of exponential functions as shown in Eq. (2),

$$I(t) = \begin{cases} 0, & t < 0 \\ I_{off} + \sum_i A_i \exp\left(\frac{-t}{\tau_i}\right), & t \geq 0 \end{cases} \qquad (2)$$

where I_{off} is the offset at a long delay time. The resultant time constants are summarized in Table 4. At 4.16 eV, feature C shows a gradual rise, which is reproduced by the single-exponential function with a time constant of 13.9 ps, whereas at 4.73 eV it exhibits depletion in sub-picosecond

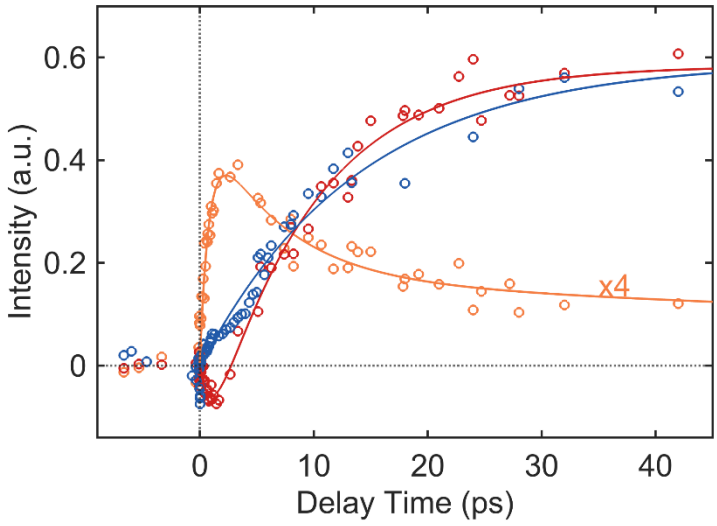

Figure 3.9: Time evolution of feature C (3.03-3.09 eV) with 4.16-eV excitation (blue), that with 4.73-eV excitation (red) and feature D (1.40-2.30 eV, orange) with 4.73-eV excitation. The intensity of feature D is magnified by a factor of 4

Table 4. Timescales describing feature C (3.03-3.09 eV) and D (1.40-2.30 eV) for different excitation energies

hν (eV)	Feature	τ_1 (ps)	τ_2 (ps)	τ_3 (ps)	A_1	A_2	A_3
4.16	C	---	13.9± 1.6	---		1.0[a]	
4.74	C	0.98± 0.5	9.0± 1.2	---	0.40[a]	-1.4	
	D	0.84± 0.27	6.6± 3.4	180 ± 85	-0.105	0.065	0.040

[a] All amplitudes at each excitation energy are normalized by the offset values (I_{off}) of feature C at a long time delay.

timescale before the appearance of positive signal with a rise time of 9 ps. Feature D at 4.73 eV exhibits a sub-picosecond rise and subsequent double-exponential decay with time constants of 6.6 and 180 ps.

3.6 Discussion

In this section, we discuss the excitation and decay processes responsible for the observed dynamics in I^-·2TU. From our previous work on iodide-nucleobases, particularly I^-·U, several pathways and channels are expected to be energetically accessible as summarized in Scheme 1.[5]

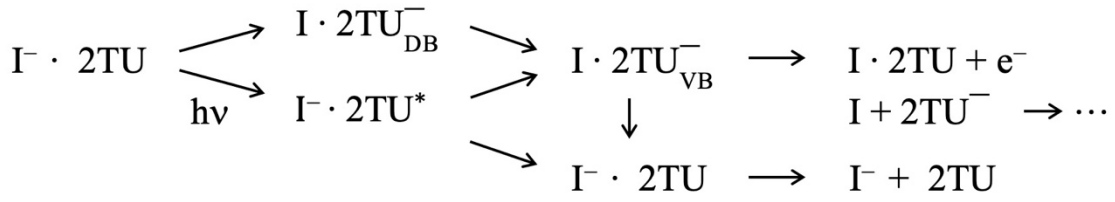

Scheme 1.

This array of possible channels provides the context for the remainder of the discussion in this section.

3.6.1 Excitation at 4.16 eV

According to Dessent[24], excitation near the VDE results in transfer of an electron from the iodide to a DB state of 2TU, according to Equation (3),

$$I^- \cdot 2TU \xrightarrow[\text{near-VDE}]{} I \cdot 2TU^-_{DB} \rightarrow I \cdot 2TU^-_{VB} \quad (3)$$

This is consistent with the presence of feature A in Figure 3.4 just after excitation. The DB state exhibits a rapid decay of 55 fs, and the most plausible explanation for this decay is conversion to the lowest VB state of $2TU^-$. From this assignment, one might expect to see a corresponding delayed onset for the VB state. However, feature B appears almost simultaneously with feature A. Nonetheless, within the IRF, even if we analyzed the time evolution of VB state with a triple-exponential function based on the assumption that there is also a ~50-fs rise component, the fitting curve is almost identical with that with a double-exponential function (see S.I.) Therefore, it is reasonable to assign the 55 fs decay to DB → VB conversion.

The calculated electron affinity to form the VB anion[29], 0.174 eV, places it approximately 0.1 eV below the DB state (Figure 3.10), enabling facile DB → VB conversion. Our assignment of the spectral features suggests that this conversion is essentially complete within 55 fs. This situation differs from I^-·U, in which DB → VB conversion occurs rapidly but the DB signal persists for many ps, indicating only partial conversion to the VB state,[5, 10] a consequence of the DB state of U^- lying below the VB state.[18] As another point of reference, the 55 fs decay is shorter than the DB → VB conversion time of 400 fs seen in I^-·CH_3NO_2, which has the same relative ordering of DB and VB states as I^-·2TU and demonstrates near complete interconversion of the TNIs.[37]

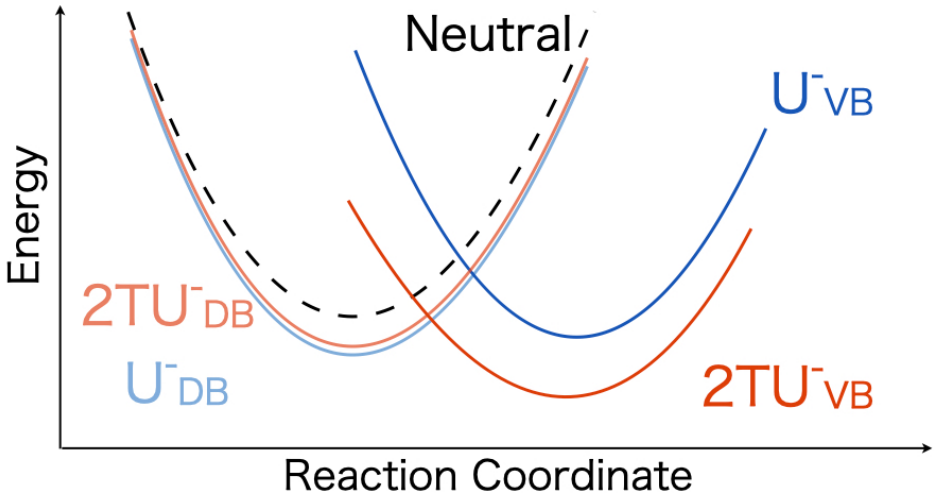

Figure 3.10: Schematic diagram of the energy levels of the neutral, dipole bound anion, and valence bound anion for 2TU (red) and U (blue).

Once the VB state is populated, it undergoes bi-exponential decay with time constants of 260 fs and 9.6 ps, with a residual constant signal seen at >100 ps. The main deactivation pathways for this state are represented by Eqs. (3) and (4),

$$I \cdot 2TU^{-}_{VB} \xrightarrow[\text{Back electron transfer}]{} I^{-} \cdot 2TU \rightarrow I^{-} + 2TU \quad (3)$$

$$I \cdot 2TU^{-}_{VB} \xrightarrow[\text{Autodetachment}]{} I \cdot 2TU + e^{-} \quad (4)$$

As reported in photofragment mass spectroscopy[24] and observed here in Figure 3.6, iodide is the main dissociative photoproduct (Eq. (3)), which strongly indicates back electron transfer to the I atom takes place as a primary deactivation channel of the VB state. In addition, autodetachment is reasonably expected as a decay channel of the VB anion, given that the excitation energy is ca. 50 meV higher than the VDE of the cluster (4.11 eV). $I{\cdot}2TU^{-}_{VB}$ can dissociate to $I + 2TU^{-}$, and this fragment anion may be responsible for the long-lived signal seen in Figure 3.7 since its photoelectron spectrum is expected to be very similar to that of $I{\cdot}2TU^{-}_{VB}$. However, $2TU^{-}$ was not observed in the photofragment mass spectrum measured by Dessent, so it may be formed here only as a long-lived transient species. Previous mass spectroscopy has also detected the H-atom loss from the 2TU anion as a minor channel,[24] but the deprotonated anion cannot be detected in this experiment due to its large VDE (3.82 eV).[38]

The experiments at 3.18 eV probe energy clearly show that fragmentation to I^{-} (feature C in Figure 3.6 a) occurs with a rise time of ~14 ps. To elucidate the I^{-} dissociation kinetics in detail, we calculated the dissociation rate based on the Rice-Ramsperger-Kassel-Marcus (RRKM) model.[39, 40] In this calculation, energies and frequencies obtained by MP2 calculations were used to determine the density of states by the Beyer-Swinehart direct count algorithm with the Stein-Rabinovitch modification.[41, 42] The in-plane rocking mode and out-of-plane twisting mode are treated as hindered rotors because their frequencies decrease notably as the N1-I length increases. Further description of this calculation is found in the S.I. We calculate a dissociation rate constant of 4.80×10^{10} s^{-1} (20.8 ps), which is in reasonable agreement with the experimental value. Assuming the 260 fs decay constant of feature B includes back-electron transfer, this process would re-form $I^{-}{\cdot}2TU$ with sufficient vibrational energy to fragment to I^{-}, so agreement with the RRKM result is not surprising. On the other hand, this result differs notably from $I^{-}{\cdot}U$ where the time constant for I^{-} production is much longer than the RRKM prediction; possible reasons are discussed in Section VC.

3.6.2 Excitation at 4.73 eV

When $I^{-}{\cdot}2TU$ is excited at 4.73 eV, VB state signal appears within the cross-correlation of the laser while DB signal is notably absent. This matches the results observed for $I^{-}{\cdot}U$ at a similar excitation energy.[8, 10] Various mechanisms have been proposed for the near instantaneous production of the VB state in $I^{-}{\cdot}U$,[10, 11] but the most plausible is that it arises via localized $\pi\pi^{*}$ excitation of uracil followed by ultrafast excess electron transfer from iodide into the hole created by this excitation, as given by Eq. (5).

$$I^- \cdot 2TU \xrightarrow[\pi\pi^*]{} I^- \cdot 2TU^* \rightarrow I \cdot 2TU^-_{VB} \quad (5)$$

In $I^-\cdot 2TU$, two broad bands (features B and B') appear within the IRF and decay bi-exponentially. The faster decay time constants are 125 fs for feature B and 70 fs for feature B'. Although these time constants are within error, the distinct additional feature B' and its faster decay rate suggest that two VB states are present. This interpretation is consistent with the UV spectrum of 2-thiouracil,[43] in which excitation at 4.73 eV can access two overlapped excited states comprising the $\pi_s\pi_6^*$ and, at higher energy, the $\pi_s\pi_2^*$ transitions, with the π^* orbitals localized around C6 and C2, respectively (see Figure 3.2). Hence, the mechanism in Eq. (5) can initially result in two VB anion states corresponding to the excess electron residing in either the π_6^* or π_2^* orbitals, leading to feature B or B' in the TRPE spectrum. The 70 fs decay constant for B' can represent a combination of internal conversion to the lower VB state, autodetachment, and back-electron transfer to the I atom. The 125 fs decay time for the lower VB state is attributed to the latter two processes.

The rise of the iodide peak (feature C) in 4.74 eV pump is significantly faster (9 ps) than that in 4.16 eV (14 ps). As with 4.16 eV excitation, the rate calculated with RRKM theory is in reasonable agreement at the higher excitation energy: calculations predict that I^- should appear in 11.8 ps. This indicates that the excited states of $I^-\cdot 2TU$ decay to the ground state rapidly enough for iodide to dissociate with timescales statistically determined by the excitation energies.

At this higher excitation energy, re-formation of the ground state with sufficient vibrational energy for I^- dissociation is possible not only by back electron transfer, but also via internal conversion from excited states localized on the chromophore, as was seen in uracil (Eq. (6)),

$$I^- \cdot 2TU \xrightarrow[h\nu]{} I^- \cdot 2TU^* \rightarrow I^- \cdot 2TU \rightarrow I^- + 2TU \quad (6)$$

Ullrich and coworkers reported the $\pi\pi^*$ (S_2) and $n\pi^*$ (S_1) states of 2TU decay within 1 ps for excitation energies ranging from 4.25 to 4.98 eV[43]. Due to this rapid re-population of the ground state with considerable vibrational energy, the overall rate for iodide dissociation can still be determined by statistical decay of the ground state. Although the calculated dissociation rates are near the limit where RRKM may fail owing to incomplete intramolecular vibrational redistribution (IVR) is not complete, the agreement between the calculated and experiment lifetimes at two excitation energies suggests that RRKM is an appropriate vehicle for the interpretation of our results.

The slower time constants for decay of the VB states in 4.73 eV excitation are longer than 10 ps. Since this is longer than the timescale for iodide release, this slow decay does not contribute to the back electron transfer leading to the iodide dissociation. It is possible that these decays reflect disappearance of the VB state via deprotonation; we note that deprotonation of 2TU occurs via dissociative electron attachment at electron energies of 0.6 eV,[27] close to the difference between the 4.73 eV photon energy and the VDE of $I^-\cdot 2TU$. Moreover, the deprotonated anion cannot be photodetached at 3.18 eV.[38] Deprotonation is likely to be much less efficient at 4.16 eV excitation, so a portion of VB anions remains at relatively long time delays, giving rise to the offset component in the TRPE spectrum and to the low photofragmentation yields observed by mass spectroscopy.[24]

Feature D is relatively weak signal which only appears with higher energy excitation. Previous computational work on 2TU tautomers with coupled cluster singles and doubles with perturbative triples correlations (CCSD(T)) suggested that the tautomer R15, where a proton is

transferred from N1 to C5, is more stable than the canonical form of 2TU, and has a VDE of 1.66 eV.[29] This is almost identical to the eBE of Feature D, which is centered around 1.7 eV, providing evidence for a tentative assignment of feature D as the tautomer.

3.6.3 Comparison with $I^-\cdot U$

In photoexcited $I^-\cdot U$, the measured rise times for fragmentation to I^- are 86 ps and 36 ps for near-VDE and 4.7 eV excitation, respectively. These values are noticeably slower than those found here for $I^-\cdot 2TU$, namely 14 ps and 9 ps at the analogous excitation energies. The two rise times for $I^-\cdot 2TU$ are relatively consistent with RRKM values for the dissociation of vibrationally excited $I^-\cdot 2TU$, whereas those for $I^-\cdot U$ are considerably larger than calculated RRKM values (8.6 and 4.4 ps). Hence, there appears to be a bottleneck to the formation of energized $I^-\cdot U$ that is absent in $I^-\cdot 2TU$.

For near VDE excitation of $I^-\cdot U$, the DB and VB states persist considerably longer than those seen here, with bi-exponential decay constants of 5 and 500 ps for the DB state and 5 and 80 ps for the VB state. Assuming that back electron transfer to the iodine is reflected in these decays, then this process, which is necessary for the formation of energized $I^-\cdot U$, is much slower than in $I^-\cdot 2TU$, and this may account for the slower iodide fragmentation channel in $I^-\cdot U$. As discussed above, the VB anion of $2TU^-$ lies below the DB anion, in contrast to canonical uracil, resulting in substantially more complete DB $\rightarrow$ VB conversion in photoexcited $I^-\cdot 2TU$. When only a small portion of the DB state can convert to the VB state, this may cause a bottleneck for I^- production and decrease the rate at which transient states can decay. It seems likely that the rate of back electron transfer from the VB state is also key to understanding these dynamics, although further investigation will be necessary to elucidate all factors.

At the higher excitation energy, which is assigned primarily to $\pi\pi^*$ excitation in both $I^-\cdot U$ and $I^-\cdot 2TU$, internal conversion of the chromophore back to its ground electronic state will produce an energized complex that would be expected to undergo statistical decay, and this indeed appears to be the case in $I^-\cdot 2TU$. However, there is experimental and theoretical evidence that the bright S_2 $\pi\pi^*$ state in uracil relaxes to the dark S_1 $n\pi^*$ state where it can remain for many ps before reaching the ground state;[44, 45] this process may be the dynamical bottleneck that results in the slower-than-statistical fragmentation to $I^- + U$. Ulrich and co-workers[43] find that the excited singlet states of 2TU relax within 1 ps, so the analogous bottleneck is not expected to play a role in the fragmentation of $I^-\cdot 2TU$. We note, however, that back-electron transfer from the VB anion is also expected to play a role in fragmentation to I^- at 4.73 eV excitation, so the overall mechanism for this process is complex and worthy of further investigation in both systems.

3.7 Conclusions

TRPES with the combination of two different excitation (4.16 and 4.73 eV) and probe (1.59 and 3.18 eV) energies has been applied to $I^-\cdot 2TU$ clusters to observe the dynamics of low energy

electron attachment to 2TU. The DB anion of 2TU is accessed immediately after near-VDE excitation, then decays to the VB state on a timescale of ca. 55 fs. This indicates that the DB state of 2TU acts as a "doorway" to form the VB state. The energy gap between DB and VB states in 2TU is anticipated to be the driving force of this ultrafast internal process. We find that the interconversion of DB and VB anion is much more complete in I^-·2TU than I^-·U. This result is attributed to the VB anion of 2TU lying below its DB state, in contrast to the analogous species for U where the ordering is reversed. For 4.73 eV excitation, the DB feature is not observed and, in addition to the expected VB state, a higher-lying π^* anion forms before being rapidly (70 fs) deactivated.

At both excitation energies, we observe by means of a 3.18 eV probe pulse a strong feature that is clearly ascribable to dissociated I^-. The excitation energy-dependent dissociation dynamics are found to be in good agreement with those predicted by RRKM theory, suggesting the vibrationally excited ground state I^-·2TU is prepared without a dynamic bottleneck. Formation of the vibrationally excited I^-·2TU is attributed to back electron transfer from the VB state at both excitation energies and, at 4.73 eV, to $\pi\pi^*$ excitation followed by internal conversion of the 2TU to its ground state. The ~10 ps time scales for I^- formation are in contrast to the much slower dissociation rates seen in previous TRPES experiments on I^-·U.

3.8 Supporting Information

3.8.1 Theoretical estimation of the rate constant of the iodide dissociation

Rice-Ramsperger-Kassel-Marcus (RRKM) model transition state treatment was used to calculate microcanonical rate constants for I^- dissociation The rate of a reaction is given by eq. (2)

$$k(E) = \frac{\int_0^{E-E_0} G(E - E_0)}{h\, N(E)} \tag{2}$$

Where E is the energy provided for the reaction (here taken to be the excitation pulse energy), E_0 is the zero point energy (ZPE) corrected energy barrier between the reactant species and the transition state, h is Planck's constant, G is density of states for the transition state, and N is the density of states for the reactant. Energies and frequencies obtained by MP2 calculations were used to calculate the density of states by the Beyer-Swinehart direct count algorithm with the Stein-Rabinovitch modification. The in-plane rocking mode and out-of-plane twisting mode are treated as hindered rotors because their frequencies are particularly decreased as the I–N1 bond length increases.

Because dissociation is expected to occur as a barrierless transition, the transition state is determined variationally as the point in I^- dissociation when the constant k(E) is lowest. For this cluster, this occurs with an I-N1 distance of about 8.3 Å. With all frequencies treated harmonically, this yields RRKM constants of 2.51×10^{11} s^{-1} with 4.73 eV excitation and 1.38×10^{11} with 4.16 eV excitation, corresponding to dissociation times of 4.00 ps and 7.20 ps respectively.

Two frequency modes of the transition state, the in plane rocking mode and out of plane twisting mode, have particularly low frequencies, particularly as the bond length between N1 and I increases. These vibrations may be better treated as hindered rotors.–With this correction, we calculate dissociation rate constants of $8.62\times^{11}$ s^{-1} (11.80 ps) with 4.73 eV excitation and 4.80×10^{10} s^{-1} (20.8 ps) with 4.16 eV excitation, results that are in good agreement with the experimentally determined rate constants for feature C, which grows in with time constants of 9 ps for 4.73 eV excitation and 14 ps for 4.16 eV excitation.

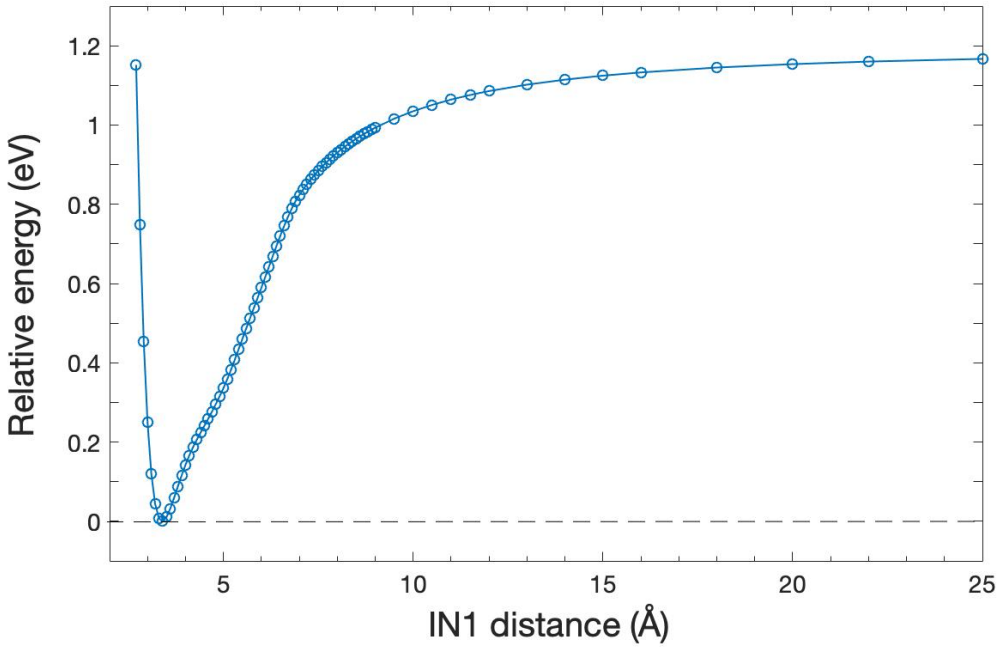

Figure 3.S1: Potential energy curve calculated by geometric optimization at fixed I–N1 distances. Energies are calculated at MP2/aug-cc-pVDZ-(pp) level of theory.

3.8.2. Fitting results in 4.16 eV excitation under the convolved triple-exponential function

Table S1. Fitting results for feature B under the convolved triple- and double-exponential functions.

	τ_1 (fs)	τ_2 (fs)	τ_3 (ps)	A_1	A_2	A_3
3exp	34 ± 33	390 ± 294	10.1 ± 2.0	-0.515[a]	0.387	0.613
2exp	---	260 ± 90	9.6 ± 1.5	---	0.46	0.54

[a]All amplitudes shown here are normalized by the sum of the decay amplitudes.

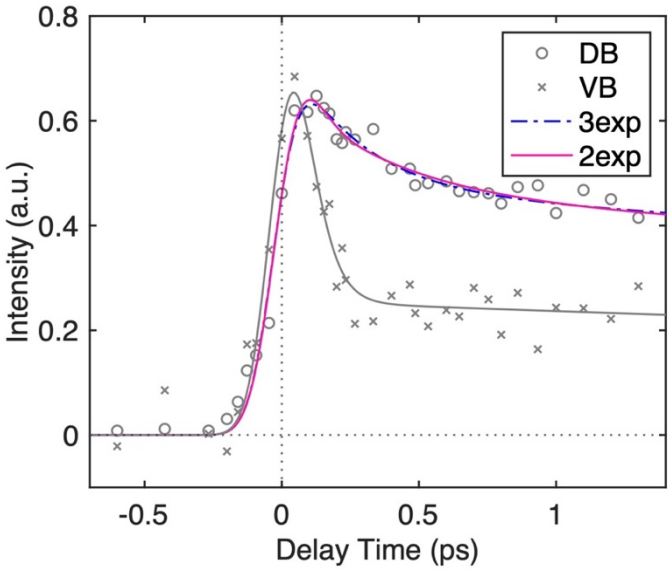

Figure 3.S2: Time evolutions of the photoelectron intensities of DB (feature A: 0 – 0.2 eV) and VB (feature B: 0.5 – 1.0 eV) regions under 4.16-eV excitation and 1.59-eV probe. The convolved double-exponential fitting results for DB feature is plotted as a black solid line, while the fitting results for VB state are shown as a purple line for a double-exponential fit and a blue dash-dotted line for a triple exponential fit.

References

1. B. Boudaïffa, P. Cloutier, D. Hunting, M. A. Huels and L. Sanche, Science **287**, 1658–1660 (1998).
2. P. Burrow, G. A. Gallup, A. M. Scheer, S. Denifl, S. Ptasinska, T. Mark and P. Scheier, J. Chem. Phys. **125** (12), 124310 (2006).
3. J. Gu, J. Leszczynski and H. F. Schaefer, Chem. Rev. **112** (11), 5603–5640 (2012).
4. J. N. Bull, C. W. West and J. R. Verlet, Chem. Sci. **7** (8), 5352–5361 (2016).
5. A. Kunin and D. M. Neumark, Phys. Chem. Chem. Phys. **21** (14), 7239–7255 (2019).
6. S. B. King, M. A. Yandell and D. M. Neumark, Faraday Discuss. **163**, 59–72 (2013).
7. S. B. King, A. B. Stephansen, Y. Yokoi, M. A. Yandell, A. Kunin, Y. Takayanagi and D. M. Neumark, J. Chem. Phys. **143** (2), 024312 (2015).
8. M. A. Yandell, S. B. King and D. M. Neumark, J. Am. Chem. Soc. **135** (6), 2128–2131 (2013).
9. A. B. Stephansen, S. B. King, Y. Yokoi, Y. Minoshima, W.-L. Li, K. A., T. Takayanagi and D. N. Neumark, J. Chem. Phys. **143** (10), 104308 (2015).
10. S. B. King, M. A. Yandell, A. B. Stephansen and D. M. Neumark, J. Chem. Phys. **141** (22), 224310 (2014).
11. W.-L. Li, A. Kunin, E. Matthews, N. Yoshikawa, C. E. Dessent and D. M. Neumark, J. Chem. Phys. **145** (4), 044319 (2016).
12. A. Kunin, W.-L. Li and D. M. Neumark, J. Chem. Phys. **149** (8), 084301 (2018).
13. A. Kunin, V. S. McGraw, K. G. Lunny and D. M. Neumark, J. Chem. Phys. **151** (15), 154304 (2019).
14. A. Stolow, A. E. Bragg and D. M. Neumark, Chem. Rev. **104** (4), 1719–1758 (2004).
15. E. Matthews, R. Cercola, G. Mensa-Bonsu, D. M. Neumark and C. E. Dessent, J. Chem. Phys. **148** (8), 084304 (2018).
16. R. Cercola, E. Matthews and C. E. H. Dessent, Mol. Phys. **21**, 3001–3010 (2019).
17. R. Cercola, K. O. Uleanya and C. E. H. Dessent, Mol. Phys. **118** (12), e1662128 (2020).
18. J. H. Hendricks, S. A. Lyapustina, H. L. d. Clercq, J. T. Snodgrass and K. H. Bowen, The Journal of Chemical Physics **104** (19), 7788-7791 (1996).
19. R. A. Bachorz, W. Klopper and M. Gutowski, The Journal of Chemical Physics **126** (8), 085101 (2007).
20. G. W. Anderson, I. Halverstadt, W. H. Miller and R. O. Roblin Jr, J. Am. Chem. Soc. **67** (12), 2197–2200 (1945).
21. P. Ajitkumar and J. D. Cherayil, Microbiol. Rev. **52** (1), 103–113 (1988).
22. M. Pollum, S. Jucusch and C. E. Crespo-Hernandez, J. Am. Chem. Soc. **136** (52), 17930–17933 (2014).
23. J. Cohen, American Assocation for the Advancement of Science (2021).
24. K. O. Uleanya and C. E. Dessent, Phys. Chem. Chem. Phys. **23** (2), 1021–1030 (2021).
25. A. Khvorostov, L. Lapinski, H. Rostkowska and M. J. Nowak, J. Phys. Chem. A **100** (34), 7700–7707 (2005).
26. J. Kopyra, H. Abdoul-Carime, F. Kossoski and M. d. N. Varella, Phys. Chem. Chem. Phys. **16** (45), 25054–25061 (2014).
27. J. Kopyra, K. K. Kopyra, H. Abdoul-Carime and D. Branowska, J. Chem. Phys. **148** (23), 234301 (2018).
28. X. Li, J. Chen and K. H. Bowen, J. Chem. Phys. **134** (7), 074304 (2011).
29. O. Dolgounitcheva, V. Zakrzewski and J. Ortiz, J. Chem. Phys. **134** (7), 074305 (2011).

30. A. V. Davis, R. Wester, A. E. Bragg and D. M. Neumark, The Journal of Chemical Physics **118** (3), 999-1002 (2003).
31. A. E. Bragg, J. R. R. Verlet, A. Kammrath, O. Cheshnovsky and D. M. Neumark, Journal of the American Chemical Society **127** (43), 15283-15295 (2005).
32. W. Wiley and I. H. McLaren, Rev. Sci. Instrum. **26** (12), 1150–1157 (1955).
33. V. Dribinski, A. Ossadtchi, V. A. Mandelshtam and H. Reisler, Rev. Sci. Instrum. **73** (7), 2634–2642 (2002).
34. M. J. Frisch, G. W. Trucks, H. B. Schlegel, G. E. Scuseria, M. A. Robb, J. R. Cheeseman, G. Scalmani, V. Barone, G. A. Petersson, H. Nakatsuji, X. Li, M. Caricato, A. V. Marenich, J. Bloino, B. G. Janesko, R. Gomperts, B. Mennucci, H. P. Hratchian, J. V. Ortiz, A. F. Izmaylov, J. L. Sonnenberg, D. Williams-Young, F. Ding, F. Lipparini, F. Egidi, J. Goings, B. Peng, A. Petrone, T. Henderson, D. Ranasinghe, V. G. Zakrzewski, J. Gao, N. Rega, G. Zheng, W. Liang, M. Hada, M. Ehara, K. Toyota, R. Fukuda, J. Hasegawa, M. Ishida, T. Nakajima, Y. Honda, O. Kitao, H. Nakai, T. Vreven, K. Throssell, J. Montgomery, J. A., J. E. Peralta, F. Ogliaro, M. J. Bearpark, J. J. Heyd, E. N. Brothers, K. N. Kudin, V. N. Staroverov, T. A. Keith, R. Kobayashi, J. Normand, K. Raghavachari, A. P. Rendell, J. C. Burant, S. S. Iyengar, J. Tomasi, M. Cossi, J. M. Millam, M. Klene, C. Adamo, R. Cammi, J. W. Ochterski, R. L. Martin, K. Morokuma, O. Farkas, J. B. Foresman and D. J. Fox, *Gaussian 16, Rev. A.03*. (Gaussian, Inc.: Wallingford, CT, 2016).
35. K. A. Peterson, B. C. Shepler, D. Figgen and H. Stoll, J. Phys. Chem. A **110** (51), 13877–13883 (2006).
36. A. Kunin, W.-L. Li and D. M. Neumark, Phys. Chem. Chem. Phys. **18**, 33226 (2016).
37. M. A. Yandell, S. B. King and D. M. Neumark, J. Chem. Phys. **140** (18), 184317 (2014).
38. K. O. Uleanya, R. Cercola, M. Nikolova, E. Matthews, N. G. K. Wong and C. E. Dessent, Molecules **25** (14), 3157 (2020).
39. T. Baer, W. L. Hase and L. William, *Unimolecular reaction dynamics: theory and experiments*. (Oxford University Press on Demand, 1996).
40. R. G. Gilbert and S. C. Smith, *Theory of unimolecular and recomination reactions*. (Publishers' Business Services, 1990).
41. T. Beyer and D. Swinehard, Communications of the ACM **16** (6), 379 (1973).
42. S. E. Stein and B. Rabinovitch, J. Chem. Phys. **58** (6), 2438–2445 (1973).
43. J. A. Sánchez-Rodríguez, A. Mohamadzada, S. Mai, B. Ashwood, M. Pollum, P. Marquetand, L. González, C. E. Crespo-Hernández and S. Ullrich, Phys. Chem. Chem. Phys. **19** (30), 19756–19766 (2017).
44. P. J. Hare, C. E. Crespo-Hernández and B. Kohler, Proc. Natl. Acad. Sci. U.S.A. **104** (2), 435–440 (2007).
45. S. Ullrich, T. Schultz, M. Z. Zgierski and A. Stolow, Phys. Chem. Chem. Phys. **6**, 2796-2801 (2004).

Chapter 4

Electron Transfer Dynamics of Iodide-4-Thiouracil Cluster

Adapted from M. Asplund, M. Koga, Y.J. Wu, and D.M. Neumark "Time resolved photoelectron spectroscopy of iodide-4-thiouracil cluster: the ππ state as a doorway for electron attachment" J. Chem. Phys. 160, 054301 (2024)*

4.1 Abstract

The photophysics of thiobases — nucleobases in which one or more oxygen atoms are replaced with sulfur atoms — have been shown to vary greatly depending on the location of sulfonation. Not only are direct dynamics of the neutral thiobase impacted, but also the dynamics of excess electron accommodation. In this work, time resolved photoelectron spectroscopy (TRPES) is used to measure binary anionic clusters of iodide and 4-thiouracil, I^-·4TU. We investigate charge transfer dynamics driven by excitation at 3.88 eV, corresponding to the lowest $\pi\pi^*$ transition of the thiouracil, and 4.16 eV, near the cluster vertical detachment energy. The photoexcited state dynamics are probed by photodetachment with 1.55 eV and 3.14 eV pulses. Excitation at 3.88 eV leads to signal from the valence-bound ion only, indicating a charge accommodation mechanism that does not utilize the dipole-bound anion as an intermediate. Excitation at 4.16 eV rapidly gives rise to dipole-bound and valence-bound ion signals, with a second rise in valence-bound signal corresponding to the decay of the dipole-bound signal. The dynamics associated with the low energy $\pi\pi^*$ excitation of 4-thiouracil provide clear experimental proof for the importance of localized excitation and electron backfilling in halide-nucleobase clusters.

4.2 Introduction

The photophysics of natural nucleobases have been studied extensively owing to their biological significance and the role that fast non-adiabatic relaxation plays in their high photostability.[1-8] In contrast, single atom substitutions, such as the replacement of one or both nucleobase oxygens with sulfur atoms, have been shown to have profound impacts on relaxation pathways following photoexcitation.[9-17] These nucleobase derivatives are of interest owing to their potential for pharmacological applications such as phototherapy where they can act as photosensitizers.[9-11, 18, 19] For example, upon photoexcitation of sulfur substituted nucleobases, the quantum yield for relaxation to the triplet manifold nears unity, resulting in increased reactivity compared to canonical nucleobases.[7, 9, 11, 14, 16] It is also of interest to contrast the interactions of natural and thio-substituted nucleobases with low energy electrons, since this interaction is also important in radiation chemistry and biology. This latter consideration motivates the present study, which examines the dynamics of photoexcited I^-·4-thiouracil (I^-·4TU) cluster anions and builds on our previous work on I^-·2-thiouracil (I^-·2TU) to elucidate the effects of sulfonation on charge transfer mechanisms.

Within a cell, DNA damage may occur via direct or indirect interactions between photons and a DNA strand. In particular, indirect interactions via low energy electrons have been implicated as a significant contributor to strand breakages.[20, 21] These considerations have motivated electron scattering and photoionization studies of gas phase canonical and modified nucleobase species,[22] as the nucleobase is predicted to be the initial site of electron attachment.[23-26] Dissociative electron attachment (DEA) measurements show that the major product of interactions of nucleobases and low energy (<3 eV) electrons is H loss from the base via NH bond ruptures.[27-31] DEA studies of 2-thiouracil (2TU) similarly show that NH bond cleavage accounts for the majority of dissociation products,[32-34] though equivalent results have not been published for 4-thiouracil.

Electron scattering experiments are complemented by photoelectron spectroscopy (PES) of nucleobase anions. These experiments demonstrate that during electron capture, a low energy electron may become associated with a nucleobase as either a dipole-bound (DB) or valence-bound (VB) anion, which are readily distinguished by their spectroscopic signals.[35-37] DB anions can only form for a molecule with a sufficiently large dipole moment,[38, 39] as they are the result of association between an excess electron and a molecular dipole. DB anions are generally weakly bound, with a geometry relatively unperturbed relative to the neutral. An excess electron may also be captured by one of the unoccupied valence (usually anti-bonding) orbitals of the molecule, forming a VB anion. In nucleobases, the VB anion forms by population of the π^* orbital, causing a ring puckering distortion of the molecule.[40, 41] PES of uracil anions shows features from both DB and VB anions, with an intense, sharp feature at low binding energy, corresponding to a DB anion, as well as a broader feature associated with a rare tautomer valence anion.[35, 36]

Photoelectron spectroscopy of the 4-thiouracil and dithiouracil anions,[42] supported by computational work,[43] demonstrates that both thiobases can form stable valence-bound anions in their canonical forms. These data show no evidence for stable dipole-bound anions for either thiobase. However, DEA of 2TU implicates a DB state in facilitating dissociative electron attachment to the thiobase,[32] indicating the possible importance of transient DB anions in these systems.

The dynamics of electron capture have been investigated for several nucleobases by time-resolved photoelectron spectroscopy (TRPES)[41] and one-photon photodepletion spectroscopy of iodide-nucleobase clusters.[44] In TRPES experiments, the halide anion acts as an electron donor, with charge transfer instigated by a femtosecond UV pump pulse. The resultant transient negative ions of the nucleobase are probed by a second femtosecond laser pulse that detaches the excess electron. We have previously carried out experiments on iodide-nucleobase clusters, including

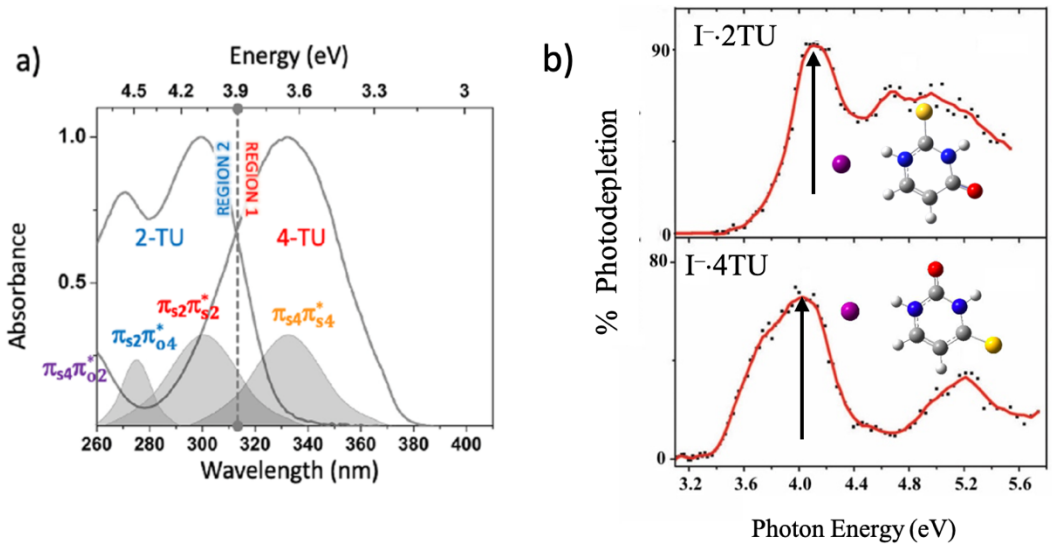

Figure 4.1: a)Absorption spectra of 2TU and 4TU in carbon tetrachloride solution with bands assigned to specific $\pi\pi^*$ transitions adapted from Mohamadzade et al[10] b) Gas phase photodepletion spectra of I^-2TU and I^-4TU adapated from Uleanya et al[42] with optimized geometries for both clusters and arrows representing the VDE of each cluster.

iodide-uracil,[45-47] iodide-thymine,[47, 48] iodide-adenine,[49] iodide-uracil H_2O,[50, 51] and iodide-2-thiouracil[52], while photodepletion measurement have been applied to clusters of iodide with all of the canonical DNA and RNA nucleobases,[44, 46, 53] as well as iodide-2-thiouracil, iodide-4-thiouracil, and iodide-2,4-thiouracil.[54, 55]

In each of the systems measured by TRPES, the DB anion is formed when the cluster is excited near its vertical detachment energy (VDE, near 4 eV for these clusters), exciting the excess electron into a DB state of the complex. One also observes rapid formation of VB states upon near-VDE excitation, although direct excitation of an electron into the VB state is not generally favorable. In measurements where the cluster is excited near its VDE, DB signal arises more quickly than VB signal, suggesting that the DB state acts as a gateway state. However, VB signal is also observed in experiments with higher energy excitation (4.7 eV), wherein there is no evidence of DB ion formation. Although we originally proposed that photoexcitation directly transferred an electron from the I^- into a VB state of the nucleobase, subsequent work suggested an alternate mechanism in which the UV pump pulse excites the strong $\pi\pi^*$ absorption of the nucleobase followed by electron transfer from the I^- into the π vacancy.[46] Thus far, however, direct experimental evidence for either mechanism has been elusive.

The cluster I^-·4TU offers an opportunity to examine how VB chromophore ions can form without the involvement of a DB state. As shown in Figure 4.1, the isolated thiobase 4TU has a particularly low energy $\pi\pi^*$ excitation relative to other nucleobases such as uracil or 2TU,[16] and photodepletion measurements of the I^-·4TU cluster[55] show an electronic absorbance below the VDE of the cluster (Figure 4.1, right panel). This presents an opportunity to isolate the potential impact of $\pi\pi^*$ excitation while minimizing the contributions of higher energy electron scattering mechanisms. Additionally, as I^-·4TU DB anions are easily distinguished from localized excitations by TRPES, a short-lived DB anion signal for the cluster can in principle be separated from the broad shoulder at ~3.8 eV observed by photodepletion spectroscopy.

In this study, we use TRPES of the iodide-4-thiouracil cluster to investigate its dynamics following excitation of a $\pi\pi^*$ transition below the cluster VDE, as well as higher energy excitation near the cluster VDE. Our results at the lower excitation energy isolate dynamics following $\pi\pi^*$ excitation, providing empirical evidence for the VB formation mechanism previously postulated wherein $\pi\pi^*$ chromophore localized excitation allows the excess electron to occupy a π orbital vacancy. This mechanism can proceed without a DB anion intermediate. At excitation near the cluster VDE, we confirm the existence of a transient DB state and characterize formation of the VB anion with two rise times, with the first caused by chromophore excitation and the second by DB anion to VB anion conversion.

4.3 Methods

The TRPEI setup has been described in other publications,[56, 57] but a brief summary will be provided here. An inert carrier gas, in this case argon, flows over a reservoir of methyl iodide and through a cartridge containing the solid 4-thiouracil sample (97%, Alfa Aesar). An Even-Lavie pulsed valve heated to 220° C and operating at 500 Hz generates a gas pulse that passes through an ionizing filament. Iodide anions are produced from dissociative electron attachment to CH_3I,

which then cluster to gas phase 4-thiouracil to make the species of interest. Ions in the pulsed beam are extracted perpendicularly by a Wiley McLaren time-of-flight mass spectrometer[58] that includes a mass gate to selectively pass iodide-4-thiouracil clusters.

In the interaction region, pump and probe laser pulses intersect with the cluster packets within a velocity-map imaging assembly. The photodetached electrons are detected by a pair of chevron-stacked microchannel plates coupled to a phosphor screen. The phosphor screen is read by a CCD camera, and the raw data images are processed using BASEX[59] to generate the kinetic energy spectra and angular distributions of the photoelectrons.

Laser pulses are generated by KM Griffin Oscillator and KM Dragon Amplifier, producing ~2 mJ/pulse at 1000 Hz repetition rate, with the fundamental centered at 1.55 eV and a pulse duration of approximately 35 fs. To generate the pump pulse, a portion of this output is directed into a TOPAS-C optical parametric amplifier to generate tunable visible light, which is subsequently doubled by a BBO crystal to obtain the final UV excitation wavelength. The remainder of the laser pulse serves as the probe (detachment) pulse. It can be directed into a delay stage and used to trace the time evolution of transient anion species of the chromophore. Alternatively, it can be frequency doubled by a BBO and the subsequent 3.14 eV probe pulse can photodetach free atomic I^-, one of the major dissociation products for the cluster. The cross-correlation of the pump and probe pulses sets the instrumental response time at about 80fs.

Dissociation of the I^-·4TU cluster to I^- and 4TU was modeled using the Gaussian 16 computing package[60] at the MP2 level of theory with an augmented Dunning basis set aug-cc-pVDZ for C, H, O, and N, and an additional set of diffuse functions (aug-cc-pVDZ-pp) for I.[61]

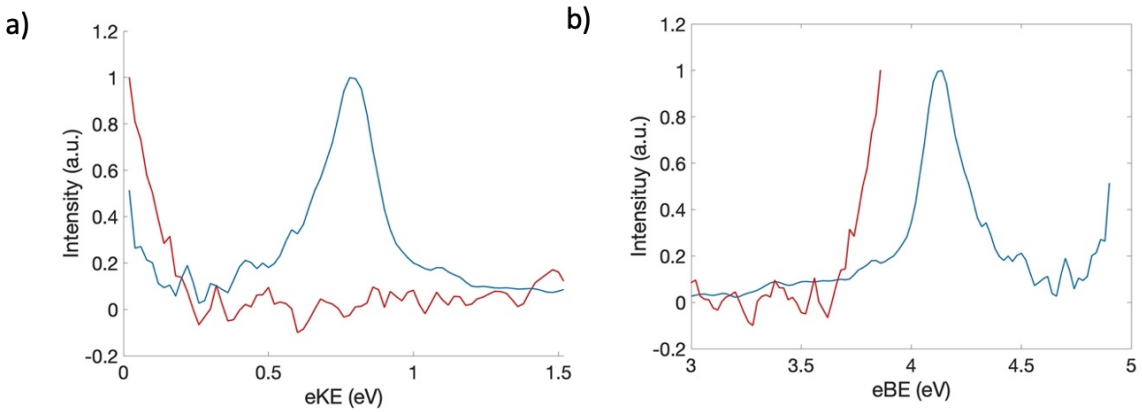

Figure 4.2: One color spectra of I-4TU collected with 4.92eV (blue) and 3.88eV (red) excitation plotted in electron kinetic energy eKE (a) and electron binding energy eBE(b)

4.4 Results

Figure 4.2 shows one color photoelectron spectra collected at hυ=3.88 eV and 4.92 eV, just under and well above the expected cluster VDE of 4 eV based on photodepletion spectroscopy.[55] The most intense feature of the spectrum at 4.92 eV excitation is a peak centered at an electron kinetic energy (eKE) of 0.74 eV, or a binding energy of 4.18, with binding energy defined as eBE= hυ-eKE. Based on previous work on related systems,[41] this feature is assigned to direct detachment to the I($^2P_{3/2}$) ·4TU spin-orbit state of the neutral cluster. This places the measured VDE of the cluster reasonably close to the calculated value given by Uleanya, et al (4.32eV),[55] as well as the VDE values for iodide-thymine, iodide-uracil, and iodide-thiouracil clusters.[41, 45, 47, 48, 52] A second, less intense feature is seen near 0 eKE and corresponds to resonant excitation of the cluster followed by electron autodetachment, as previously determined for similar clusters.[47, 48, 51]

The spectrum collected with 3.88 eV excitation of the cluster has a single feature at low eKE. This excitation is below the VDE of the cluster, so the signal is due to autodetachment or direct detachment below the VDE.

Figure 4.3 shows contour plots of time-resolved photoelectron spectra at shorter (a) and longer (b) pump-probe delays at a pump photon energy of 3.88 eV, corresponding to the low energy $\pi\pi^*$ excitation of the chromophore, and a 1.55 eV probe pulse. There are two primary features apparent in Figure 4.3. The first, labeled feature C in the right panel, is very intense and occurs mainly between 1.5 and 1.55 eBE, corresponding to near-zero (0-0.05 eV) kinetic energies. This is the energy range expected for autodetachment and it appears that this signal is enhanced at positive pump-probe delays. The spectra also show a broad feature B from 0.8 to 1.4 eV, which corresponds well with the VDE of the 4TU valence-bound ion as measured by one photon photoelectron spectroscopy by Li et al (0.7–1.5 eV).42 The feature arises very quickly after t0 before losing most of its intensity within a few hundred femtoseconds.

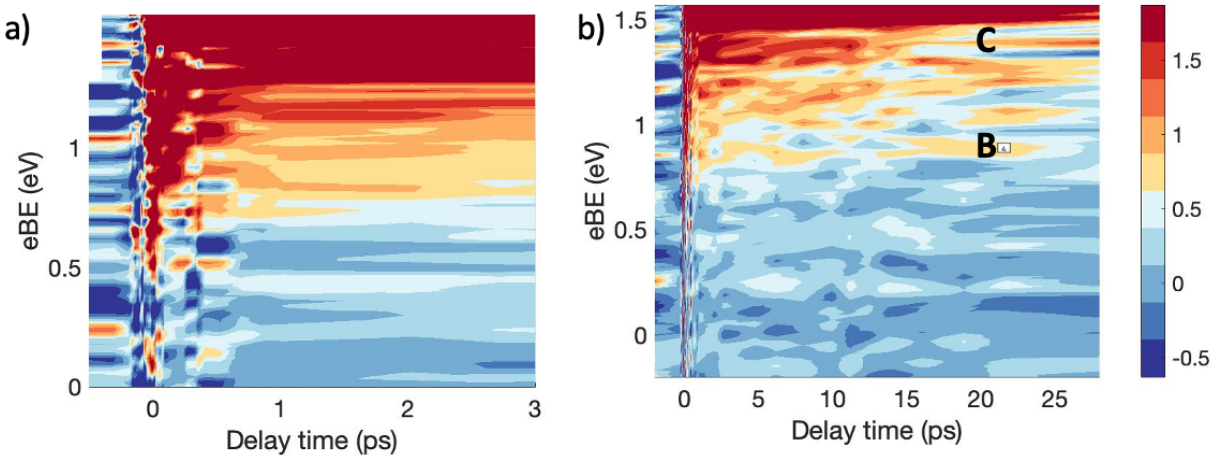

Figure 4.3: Contour plot of I^-·4TU TRPE spectra with 3.88eV pump and 1.55eV probe pulses at shorter (panel a) and longer (panel b) delay times.

Figure 4.4 shows the analogous contour plots of TRPEI measurements taken with 4.16 eV (near VDE) excitation and 1.55 eV probe and exhibits three distinct features. Near t0, two of these features look quite similar to features B and C in Figure 4.3 and are labeled accordingly. Notably, feature B is much longer lived in these spectra than the spectra with 3.88eV excitation. The third feature in Figure 4.4, feature A, is distinct from any feature in Figure 4.3. It covers 0-0.3eV, and has a much narrower spectral profile than feature B. In previous measurements of iodide-chromophore clusters, features similar to feature A have been ubiquitous in near VDE excitation measurements.[41, 46, 49-51, 62] Based on its narrow shape and low binding energy, feature A can be labeled as signal from a transient dipole-bound anion.

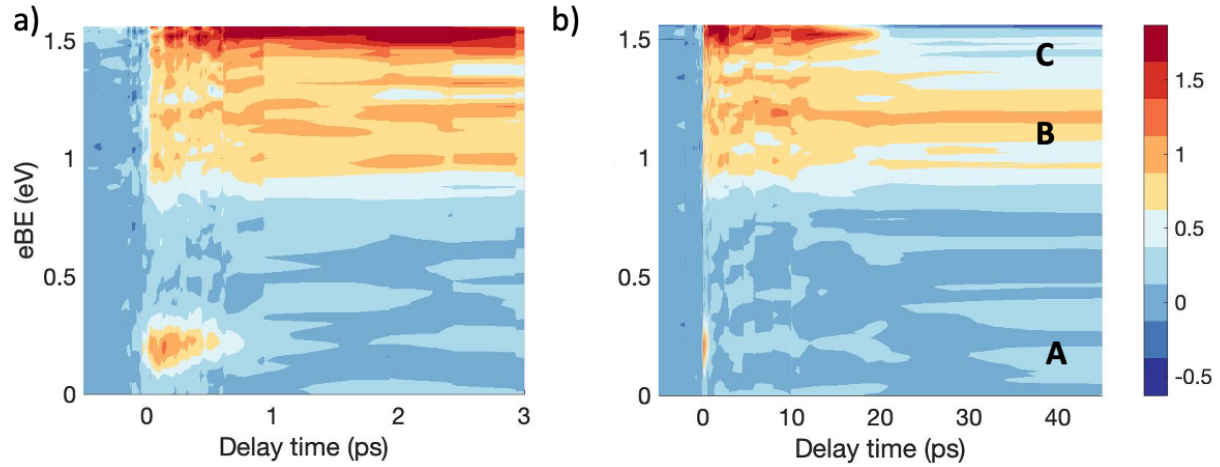

Figure 4.4: Contour plot of I^-·4TU TRPE spectra with 4.16 eV pump and 1.55 eV probe pulses at shorter (panel a) and longer (panel b) delay times

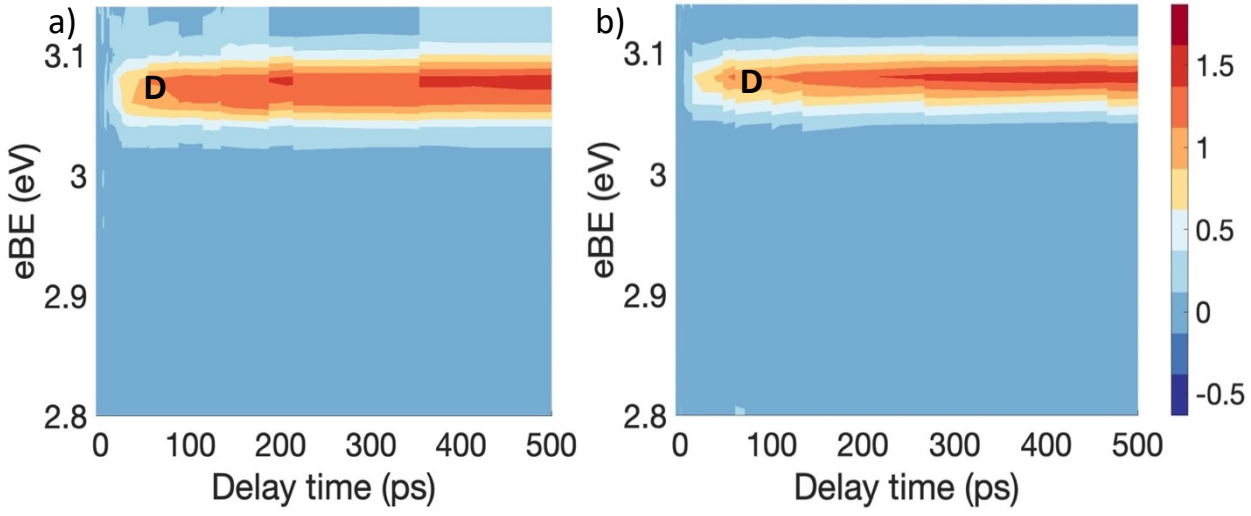

Figure 4.5: Contour plot of I^-·4TU TRPE spectra with 3.88eV (panel a) and 4.16 eV (panel b) pump and 3.14 eV probe pulses

Dynamics at both excitation energies were also probed at 3.14 eV. This energy is sufficient to just detach bare I^- to neutral iodine. Figure 4.5 shows the contour plots of measurements with a 3.14 eV probe pulse and 3.88 eV (a) or 4.16 eV (b) pump pulses. The spectra are dominated by a single feature (D) at eBE=3.06 eV, the electron affinity of atomic iodine. Feature D corresponds to photodetachment of the iodide fragment following dissociation of the photoexcited cluster to I^- + 4TU and has been seen in our previous studies of iodide-nucleobase complexes.[41, 46, 50, 63]

4.5 Analysis

The dynamics of this system are analyzed by integrating over features of the acquired spectra and then fitting the integrations to a convolution of a Gaussian experimental response function and a sum of exponential functions (Eq 1).

$$I(t) = \frac{1}{\sigma_{CC}\sqrt{2\pi}} \exp\left(-\frac{t^2}{2\sigma_{CC}^2}\right) \cdot \begin{cases} I_0\,, & t < 0 \\ I_0 + \sum_i A_i \exp\left(\frac{-t}{\tau_i}\right) + c\,, & t \geq 0 \end{cases} \quad (1)$$

In this equation, I_0 is a constant offset from background signal, σ_{CC} is the experimental response time of 80 fs, c is the signal offset at very long time delays, and A_i and τ_i are the intensity and time constant for the ith exponential function. The time evolution for several of these signals is complex, requiring multiple exponential terms to adequately fit the integrated plot. The integrated normalized intensities of features from the spectra collected with 3.88 eV excitation and 1.55 eV probe are plotted in Figure 4.6 with the corresponding parameters for Eq. 1 reported in Table 1. Integrated normalized intensities of features collected with 4.16 eV excitation and 1.55 eV probe are plotted in Figure 4.7 with fitting parameters reported in Table 2. In Figures 4.6 and 4.7, data are indicated by open circles and the fits by solid lines.

In Figure 4.6 a, signal from feature B rises within the experimental resolution of 80 fs, and decays biexponentially, with 80% of the signal decaying in $\tau 1$ =140 fs and an additional fraction decaying with $\tau 2$=9.4 ps. At later times, the signal reaches an asymptotic value with a significant offset. The signal from feature C rises within about $\tau 2$=200 fs and then decays gradually by a single exponential decay with $\tau 3$=18.4 ps.

Figure 4.7 shows the temporal evolution of the three features seen in Figure 4.4. In Figure 4.7 a, feature A (red, DB anion) rises within the experimental resolution before decaying with a single exponential component with τ_1=440fs. A small signal offset remains at long time delays attributed to background noise. The signal from feature B (blue, VB anion) requires three time constants to fit accurately. The signal rises within instrument resolution, decays partially (with time constant τ_1), undergoes a second rise (τ_2), then decays slowly (τ_3) before reaching an asymptotic offset. Qualitative examination of Figure 4.7, as well as known mechanisms for DB state mediated VB ion formation, suggests that depletion of the DB ion gives rise to the VB ion as the former state transitions into the latter. Accordingly, the rise τ_2 for the VB signal should be roughly equal to decay τ_1 for the DB signal. With three variable time constants, the precision of the fit is unacceptably low. If we fix τ_2 for the VB signal to 440 fs, i.e. τ_1 for feature A, we retrieve 47 fs for the initial VB decay constant τ_1. The signal continues to decay with τ_3 of 13.1 ps.

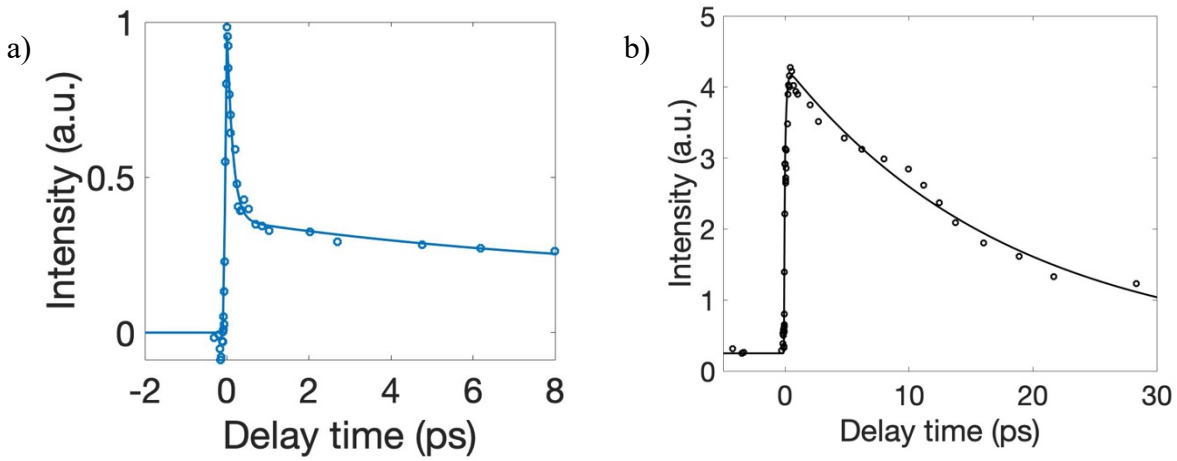

Figure 4.6: Time evolution of integrated features B (blue, VB, panel a) and C (black, AD, panel b) for 3.88eV excitation, 1.55eV probe . Signals are scaled from raw data to normalize the maximum intensity of feature B to 1.

Table 4.1. Fit parameters that reproduce the time evolution in Figure 6.

	eBE (eV)	τ_1 decay (fs)	τ_2 rise (fs)	τ_3 decay (ps)	A_1	A_2	A_3	c
Feature C	1.50–1.55	---	218 ± 93	18.4 ± 2.3	---	-0.51	1.0	·
Feature B	0.7–1.2	139 ± 36	---	9.4 ± 4.7	0.81[a]	---	0.19	0

Feature C in Figure 4.7 b has a rise time of τ_2=560 fs and decays with τ_3=16.2 ps. The fit for the AD signal is not as good as for the DB and VB signal, likely because of the narrow energy window for the integration, which is selected to minimize overlap with the VB feature.

The VDE of the DB ion shifts noticeably over the first picosecond following excitation. This can be better quantified by fitting feature C to a Gaussian function at each delay time and plotting the binding energy of the Gaussian peak over time, as shown in Figure 4.8. Because of the rapid decay of the DB state, these values are only extractable for the first 1-2 picoseconds following excitation, but over this time frame the VDE of the DB state increases by about 50 meV, following a trend observed in the DB VDE values observed for I^-U and $I^-U{\cdot}H_2O$.[45, 51]

a)

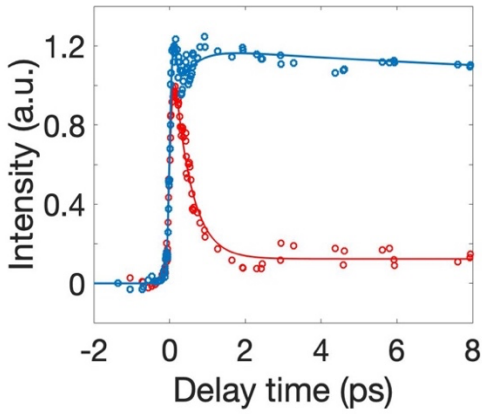

b)

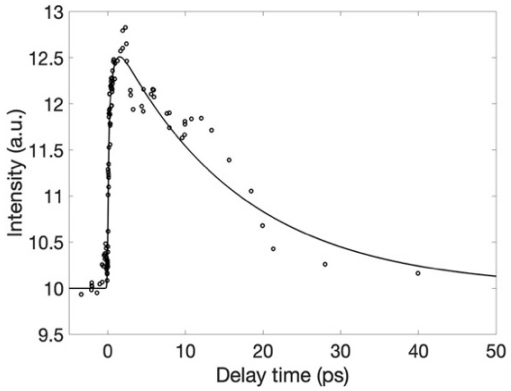

Figure 4.7: Time evolution of integrated feature A (red, DB), feature B signal (blue, VB) signal, and feature C (black, AD) for 4.16eV excitation, 1.55eV probe spectra. Feature A and B are normalized to maximum values of 1 and 1.2 respectively (panel a). Feature C is scaled using the normalization factors for feature A (panel b).

Table 4.2. Fit parameters that reproduce the time evolution in Figure 7.

	eBE (eV)	τ_1 (fs) decay	τ_2 (fs) rise	τ_3 (ps) decay	A_1	A_2	A_3	c
Feature C	1.50 – 1.55		560 ± 390	16.2 ± 3.8		-0.51	1.0	
Feature B	0.7 – 1.2	47.4 ± 6.3	442[b]	13.1 ± 9.9	0.96[a]	-0.07	0.04	0.83
Feature A	0 – 0.30	442 ± 50						

[a] All amplitudes shown here are normalized by the sum of the decay amplitudes.

[b] Value fixed using decay of DB signal

Figure 4.9 shows the integrated signal from feature D for both excitation energies probed at 3.14 eV. The rise of the feature is slow enough that the Gaussian term is unnecessary, and the data can be fit using a simple exponential rise and intensity offset, as in Eq 2.

$$I(t) = \begin{cases} 0, & t < 0 \\ I_{off} + A_i \exp\left(\frac{-t}{\tau_i}\right), & t \geq 0 \end{cases} \qquad \text{Eq. 2}$$

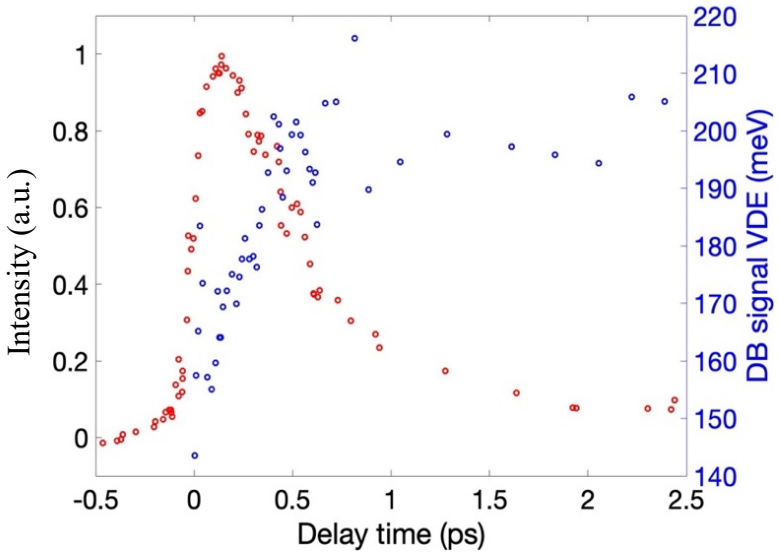

Figure 4.8: Vertical detachment energies and normalized signal intensity for Feature A (dipole-bound ion) up to 2.5 ps.

The rise time for I^- signal at each excitation energy is given in Table 3, as well as corresponding times measured for I-uracil (I^-·U) and I-2thiouracil (I^-·2TU). Higher energy excitation corresponds to a slightly faster dissociation, as we might anticipate from transition state theory, with 3.88eV excitation resulting in a 56 ps rise time and 4.16eV excitation resulting in a 41 ps rise time. For 4.16 eV, near-VDE excitation, the I^- rise time for I^-·4TU (41 ps) is a factor of ~3 longer than that of I^-·2TU (14 ps).

In the past, we have used Rice-Ramsperger-Kassel-Marcus (RRKM) theory[64, 65] to model the dissociation of I^-·N to I^-+N for various iodide nucleobase clusters, where N is the nucleobase.[46, 50, 51] The energy and vibrational frequencies of the I^-·4TU cluster were modeled at the MP2/aug-cc-pVDZ level, and the sum and density of states determined by the Beyer-Swinehart direct count algorithm with the Stein-Rabinovitch modification.[66, 67] As the transition state is loose, the reaction rate is determined variationally by modifying the N1–I distance to find the lowest calculated rate constant. With the low frequency in-plane rocking and out-of-plane twisting modes treated as hindered internal rotors, as described in greater detail elsewhere,[46, 52] we calculate dissociation time constants of 17.0 ps with 3.88 eV excitation and 11.5 ps with 4.16 eV excitation at the bond dissociation energy of 1.04 eV calculated using the level of theory given in Section II. The dependence of these values on small changes in the bond dissociation energy are discussed in Section 4.6

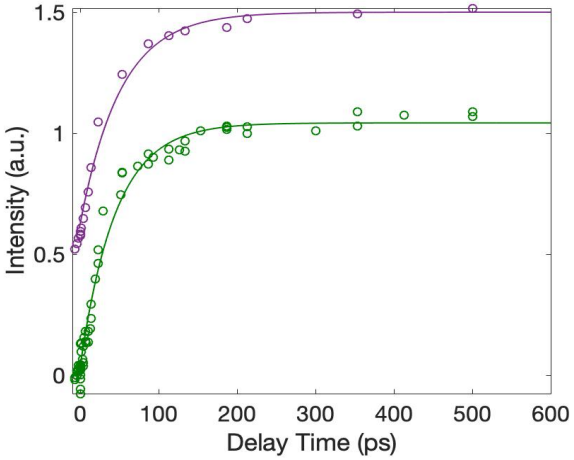

Figure 4.9: Time evolution of normalized, integrated Feature D for 4.16eV (green) or 3.88 eV (purple) excitation and 3.14 eV probe spectra. Plot at 3.88 eV is offset vertically by 0.5 a.u. to improve readability.

Table 3. Timescales describing rise time of feature D for different clusters and excitation energies

I^-·4TU		**I^-·2TU**	
hν (eV)	τ (ps)	hν (eV)	τ (ps)
3.88	56.2±9.4	---	---
4.16	40.9±7.6	4.16	13.9±1.6
---	---	4.74	9.0±1.2

4.6 Discussion

The results obtained provide several interesting insights into the general set of thiouracils and previously measured iodide-nucleobase clusters.

4.6.1 VB formation by 3.88 eV excitation

Excitation at 3.88 eV corresponds to a localized ππ* transition of 4TU, but is well below the VDE of the I⁻·4TU cluster as determined by our photoelectron spectrum. Spectra show no evidence for DB state formation, so such a state is not acting as a gateway to the observed VB anion state.

Previous iodide-nucleobase measurements have similarly resulted in spectra with VB signal but not DB signal, but these were all taken at excitation energies at 4.5-4.7 eV, well above the cluster VDE.[41, 45, 50] It was postulated, based primarily on computational results, that VB anions were formed by chromophore-localized $\pi\pi^*$ excitation followed by electron transfer from the halide to the hole in the chromophore π orbital, as shown in Eq. 3 with N as the nucleobase.[46]

$$I^- \cdot N(\pi^4\pi^{*0}) \xrightarrow{h\upsilon_{pump}} I^- \cdot N(\pi^3\pi^{*1}) \rightarrow I \cdot N(\pi^4\pi^{*1}) \quad \text{Eq. 3}$$

However, due to the high energy excitation, indirect electron scattering mechanisms involving capture of a photodetached electron from the I^- into the π* orbital, leading to the same final state, could not be ruled out.

The experimental results here provide strong empirical evidence for the $\pi\pi^*$ excitation scheme in Eq. 3. The generation of a π orbital vacancy makes charge transfer to the thiobase energetically favorable even at excitation below the cluster VDE. Our results further indicate that this process is sufficiently rapid to account for IRF limited (sub 80 fs) VB signal rise not only in this system but also in the previous above-VDE excitation energy measurements in which no DB signal was observed.

The rapid disappearance of this signal (τ_1=140 fs) is attributed to back electron transfer (BET) that results in reformation of iodide, as in previous studies of similar clusters (Eq 4a).[41, 46, 51, 52, 68] BET becomes less favorable if the iodine moves away from the valence-bound anion, a reasonable expectation given that the iodine/VB anion interaction potential will be quite different from the I^-·4TU potential. Once this happens, autodetachment (AD, Eq. 4b) can become the primary decay mechanism.

$$I \cdot 4TU^-_{VB} \xrightarrow{BET} I^- \cdot 4TU \quad \text{Eq. 4a}$$

$$I \cdot 4TU^-_{VB} \rightarrow I \cdots 4TU^-_{VB} \xrightarrow{AD} I + 4TU + e^- \quad \text{Eq. 4b}$$

The slower time constant, τ_2=9 ps, is then attributed to this latter process.

4.6.2 VB and DB dynamics with 4.16 eV excitation

Excitation of the cluster at 4.16 eV, near the experimentally determined VDE, results in both DB and VB transient anion signal, as we have seen in previous iodide-nucleobase

measurements.[41, 45, 47-50, 62] The presence of the DB anion of 4TU is notable, as photoelectron spectroscopy of $4TU^-$ [42] and photodepletion spectroscopy of $I^-\cdot 4TU$[55] did not detect this dipole-bound species.

The DB signal of $I^-\cdot 4TU$ decays in 440 fs, whereas measurements of the $I^-\cdot 2TU$ cluster show DB signal that arise and almost entirely decay within the instrument response time. This is a rather significant change in dynamics due to thionation position, with the conversion for $I^-\cdot 2TU$ remaining anomalously rapid compared to $I^-\cdot U$, $I^-\cdot 4TU$ and $I^-\cdot U\cdot H_2O$. It suggests that geometric concerns or the nearly degenerate $\pi\pi^*$ excitations of neutral 2TU may play a role in its unusual dynamics that bears further investigation.

The DB signal decays almost entirely within 2 ps, with a negligible signal offset at longer time delay. This result is similar to dynamics observed for $I^-\cdot 2TU$, and $I^-\cdot CH_3NO_2$, in which conversion from DB to VB is relatively complete. By comparison, DB signal from near-VDE excited $I^-\cdot U$ and $I^-U\cdot H_2O$ clusters exhibit bi-exponential decay, with a large portion of the signal remaining after several ps. The complete DB to VB conversion of the $I^-\cdot 4TU$, $I^-\cdot 2TU$, and $I^-\cdot CH_3NO_2$ clusters is consistent with a VB state lower in energy than the DB state.[35, 43, 69]

The VDE of the DB signal demonstrates a shift to higher binding energy over the first few ps following excitation (Figure 4.8). This shift has been attributed to motion of the neutral iodine, as increased distance between iodine and the DB anion reduces volume exclusion effects that destabilize the DB state at the shortest pump/probe delay times.[45, 51] Comparable measurements in $I^-\cdot U$ and $I^-\cdot U\cdot H_2O$ have shown that the VDE reaches an asymptote in 15–20 ps that agrees with that of the bare DB anion, suggesting that the iodine has fully dissociated from the cluster. Owing to the short-lived DB anion of $I^-\cdot 4TU$, we are unable to fully replicate this measurement. However, the VDE shifts in the first 1-2 ps suggest that initial iodine motion in $I^-\cdot 4TU$ is similar to the other clusters.

For VB signal formed by 4.16 eV excitation, an initial rise is seen within the experimental response time, followed by rapid decay (τ_1) and then a second signal rise (τ_2). The two distinct rise features indicate the likelihood of two VB formation mechanisms. The initial, IRF-limited rise can be attributed to the same mechanism underlying VB signal appearance with 3.88 eV excitation; the $\pi\pi^*$ excitation is accessible with a 4.16eV pump pulse, allowing for the transfer of the excess iodide electron to the π orbital vacancy. The second rise time τ_2 for the VB state can be fit well using the decay time for the DB state, indicating DB to VB conversion. The second rise τ_2 is absent for VB signal under 3.88 eV excitation, given that no DB population is formed. With 4.16 eV excitation, however, we are able to see both VB formation mechanisms contributing to the overall signal level.

The VB signal offset observed at long time delays is consistent with the calculated stability of the VB state of $4TU^-$ and its measurement as a photoproduct of $I^-\cdot 4TU$ in previous work.[43, 55] The VB signal generated at 4.16 eV retains most of its strength after 10 ps, in contrast to the VB signal from 3.88 eV excitation. This can be justified by considering the two VB formation mechanisms active at the higher excitation energy. The initial population of VB anions is depleted by rapid back electron transfer for both excitation energies, represented by decay constant τ_1. Only for near-VDE excitation does DB to VB formation contribute to VB signal strength after nearly 500 fs. As discussed above, the DB VDE shifts noticeably within this time frame, indicating that iodine has moved from its initial position in the anion ground state. This

inhibits back electron transfer compared to the initial cluster geometry, with bond-lengthened clusters likelier to undergo AD. Moreover, AD is the only possible decay mechanism once the I atom fully leaves the cluster.

4.6.3 Autodetachment dynamics

Autodetachment (AD) of the excess electron is apparent in the one color spectra in Figure 4.2 at both excitation energies. In previous time-resolved measurements of I^-·U and I^-·T, the AD signal exhibits a distinct depletion around t_0, as the probe pulse detaches transients that would otherwise undergo AD.[48] In I^-·4TU, as in I^-·U·H2O,[50] the depletion is not obvious, suggesting a VB state that is stabilized relative to AD.

Instead, the time-resolved spectra in Figures 4.3 and 4.4 show significant enhancement of low eKE signal at positive time delays up to ~20ps, "overshooting" the baseline level established at negative time delays. This suggests that the 1.55 eV pulse is not purely acting as a probe pulse, but produces a new state that can decay by AD. The autodetachment signal rise lags behind that of the VB by a few hundred femtoseconds, indicating that the new state may be an excitation of the VB anion, as shown in Eq 5.

$$\mathrm{I \cdot 4TU^-_{VB}} \xrightarrow{h\nu_{probe}} [\mathrm{I \cdot 4TU^-_{VB}}]^* \xrightarrow{AD} \mathrm{I \cdot 4TU} \quad + e^- \qquad \text{Eq. 5}$$

The existence of a higher-lying VB excited state was previously postulated based on measurements of the I^-·U·H_2O[41, 50] and I^-·U,[48] clusters which also show significant overshoot at positive time delays. However, I^-·T, which exhibits rapid, nearly mono-exponential decay of the VB state, lacks this AD enhancement.[48] The strongest predictor of the AD overshoot seems to be VB anion signal that lasts longer than ~5 ps, further strengthening the assignment of feature C to AD from an excited VB state.

The AD signal enhancement decays with time constants of ~18 ps and ~16 ps for 3.88 eV and 4.16 eV excitation respectively. For I^-·U and I^-U·H_2O, the intensity of the AD signal mirrors the decay of population of the VB state.[48, 50] This does not appear to be true for the I^-·4TU cluster. In particular, a very large fraction of VB signal remains at 100ps in the case of 4.16 eV excitation due to the stability of the VB anion, whereas the AD signal enhancement decays entirely. This discrepancy may arise from dynamics in the cluster that impact the accessibility of the $4TU^*_{VB}$ state but do not significantly alter the VB state itself, such as a change to solvation effects from neutral iodine motion.

4.6.4 Decay products

Photofragment product spectroscopy performed by Uleanya et al. indicate that I^-·4TU clusters excited at 4 eV produce atomic I^- as a major photofragment and the deprotonated thiobase

$[4TU\text{-}H]^-$ as a very minor photofragment.[55] Dissociation of I^- is directly measured in our setup with the 3.14 eV probe pulse, which shows a signal rising mono-exponentially with time constants of 56 ps for the 3.88 eV pump energy and 41 ps for the 4.16 eV pump energy. Iodide may be reformed by back electron transfer (Eq. 4a), and the vibrationally excited cluster can then dissociate, as shown in Eq 6.

$$I \cdot 4TU^-_{VB} \xrightarrow{BET} I^- \cdot 4TU \rightarrow I^- + 4TU \qquad \text{Eq. 6}$$

As discussed in Section IV, the experimental dissociation times are nearly four times larger than those calculated by RRKM, using the calculated bond dissociation energy of 1.04 eV. The calculated dissociation time of the $I^-{\cdot}2TU$ cluster, by contrast, is in good agreement with the experimental value.[52]

While one might attribute this discrepancy to a mechanistic difference between $I^-{\cdot}4TU$ and $I^-{\cdot}2TU$, the results of the RRKM calculation are highly dependent on the energy difference between the reactant and the calculated transition state. Figure 4.10 shows cluster dissociation time constants for $I^-{\cdot}4TU$ associated with different potential well depths with all other parameters equal.

The well depth itself is a calculated value involving a loose, barrierless transition state, and therefore somewhat uncertain. Increasing the well depth by about 15% results in a calculated time constant that agrees with the experimentally determined I^- rise time. Alternatively, the well depth can be approximated from experimental values as the difference between the cluster VDE and the electron affinity of atomic I, or 4.18 eV - 3.06 eV = 1.12 eV. Even this correction would

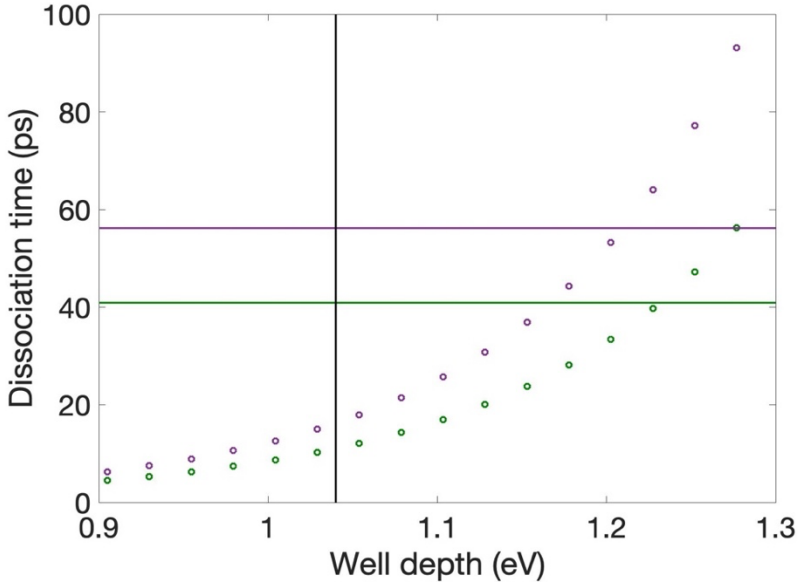

Figure 4.10: RRKM calculated dissociation time vs dissociation potential well depth for 3.88 eV (purple) and 4.16 eV(green) excitation. Experimental dissociation time constants are plotted as horizontal lines and the calculated depth given by the vertical line at 1.04 eV

be sufficient to bring the RRKM calculation dissociation time within a factor of 2 of the experimental value. It is therefore possible that the discrepancy between calculated and experimental dissociation times in I^-·4TU is caused by uncertainty of the well depth, and that the same mechanism for I^- production, Eq. 6, holds for I^-·4TU and I^-·2TU.

4.7 Conclusion

TRPES has been used to examine charge transfer dynamics of the I^-·4TU binary cluster. Excitation at 3.88 eV gives rise to VB signal without the mediation of a DB "gateway state". Rather, a localized $\pi\pi^*$ excitation of the chromophore allows for electron transfer to a vacancy in an energetically accessible π orbital of 4TU. The low energy $\pi\pi^*$ excitation of 4TU rules out other mechanistic possibilities, vindicating this pathway as a method of transient formation. Excitation at 4.16 eV leads to both VB and DB signal, with the transition between DB and VB states clear in the spectra taken with 1.55 eV probe.

At both excitation energies, the VB state decays by rapid back-electron transfer to the I atom and a slower process attributed to autodetachment. In addition, at positive pump-probe delays we observe enhanced slow photoelectron signal attributed to probe-pulse excitation (1.55 eV) of the VB state to a higher-lying state that undergoes autodetachment. Finally, with the 3.14 eV probe pulse, we find that dissociation to I^-+4TU occurs on a time scale of 10s of ps. This channel is attributed to back-electron transfer to form vibrationally excited I^-·4TU followed by statistical ground state dissociation.

References

1. S. Matsika, J. Phys. Chem. A **108**, 7584–7590 (2004).
2. C. E. Crespo-Hernández, B. Cohen, P. M. Hare and B. Kohler, Chem. Rev. **104**, 1977–2020 (2004).
3. A. Stolow, A. E. Bragg and D. M. Neumark, Chem. Rev. **104** (4), 1719–1758 (2004).
4. C. T. Middleton, K. de La Harpe, C. Su, Y. K. Law, C. E. Crespo-Hernández and B. Kohler, Annu. Rev. Phys. Chem. **60**, 217–239 (2009).
5. M. Barbatti, A. J. A. Aquino, J. J. Szymczak and H. Lischka, Proc. Natl. Acad. Sci. U.S.A. **107** (50), 21453–21458 (2010).
6. R. Improta, F. Santoro and L. Blancafor, Chem. Rev. **116** (6), 3540–3593 (2016).
7. H. Yu, J. A. Sánchez-Rodríguez, M. Pollum, E. Crespo-Hernandez, S. Mai, P. Marquetand, L. Gonzalez and S. Ullrich, Phys. Chem. Chem. Phys. **18**, 20168–20176 (2016).
8. L. Martínez-Fernández, G. Granucci, M. Pollum, C. E. Crespo-Hernandez, M. Persico and I. Corral, Chem. Eur. J. **23** (11), 2478–2728 (2016).
9. M. Pollum, S. Jockusch and C. E. Crespo-Hernandez, J. Am. Chem. Soc. **136**, 17930–17933 (2014).
10. M. Pollum and C. E. Crespo-Hernández, J. Chem. Phys. **140**, 071101 (2014).
11. M. Pollum, S. Jockusch and C. E. Crespo-Hernandez, Phys. Chem. Chem. Phys. **17**, 27851–27861 (2015).
12. S. Mai, P. Marquetand and L. González, J. Phys. Chem. Lett. **7** (11), 1978–1983 (2016).
13. S. Mai, M. Pollum, L. Martínez-Fernández, N. Dunn, P. Marquetand, I. Corral, C. E. Crespo-Hernández and L. González, Nat. Commun. **7**, 13077 (2016).
14. J. A. Sánchez-Rodríguez, A. Mohamadzada, S. Mai, B. Ashwood, M. Pollum, P. Marquetand, L. González, C. E. Crespo-Hernández and S. Ullrich, Phys. Chem. Chem. Phys. **19** (30), 19756–19766 (2017).
15. A. Mohamadzade, S. Bai, M. Barbatti and S. Ullrich, Chem. Phys. **515**, 572–579 (2018).
16. A. Mohamadzade, A. Nenov, M. Garavelli, I. Conti and S. Ullrich, J. Am. Chem. Soc. **145**, 11945–11958 (2023).
17. S. Ullrich, Y. Qu, A. Mohamadzade and S. Shrestha, J. Phys. Chem. A **126** (44), 8211–8217 (2022).
18. L. A. Ortiz-Rodrìguez and C. E. Crespo-Hernàndez, Chem. Sci. **11**, 11113–11123 (2020).
19. V.-H. Nguyen, S. Heo, C. W. Koh, J. Ha, G. Kim, S. Park and Y. Yoon, ACS Sens. **6** (9), 3462–2467 (2021).
20. B. Boudaïffa, P. Cloutier, D. Hunting, M. A. Huels and L. Sanche, Science **287**, 1658–1660 (1998).
21. J. Narayanan S J, D. Tripathi, P. Verma, A. Adhikary and A. K. Dutta, ACS Omega **8** (12), 10669-10689 (2023).
22. M. S. Robinson, M. Niebuhr and M. Gühr, Molecules **28**, 2354 (2023).
23. R. Barrios, P. Skurski and J. Simons, J. Phys. Chem. B **106**, 7991–7994 (2002).
24. J. Simons, Acc. Chem. Res. **39**, 772–779 (2006).
25. J. Berdys, I. Anuseiwicz, P. Skurski and J. Simons, J. Am. Chem. Soc **126**, 6441º6447 (2004).
26. F. Martin, P. D. Burrow, Z. L. Cai, P. Cloutier, D. Hunting and L. Sanche, Phys. Rev. Lett. **93**, 068101 (2004).
27. G. Hanel, B. Gstir, S. Denifl, P. Scheier, M. Probst, B. Farizon, M. Farizon, E. Illenberger and T. D. Märk, Phys. Rev. Lett. **90** (18) (2003).

28. S. Denifl, S. Ptasinska, M. Cingel, S. Matejcik, P. Scheier and T. D. Märk, Chem. Phys. Lett. **377**, 74–80 (2003).
29. H. Abdoul-Carime, M. A. Huels and E. Illenberger, Eur. Phys. J. D **35**, 399–404 (2005).
30. P. Burrow, G. A. Gallup, A. M. Scheer, S. Denifl, S. Ptasinska, T. Mark and P. Scheier, J. Chem. Phys. **125** (12), 124310 (2006).
31. D. Huber, M. Beikircher, S. Denifl, F. Zappa, S. Matejcik, A. Bacher, V. Grill and T. D. Märk, J. Chem. Phys. **125**, 084304 (2006).
32. J. Kopyra, H. Abdoul-Carime, F. Kossoski and M. d. N. Varella, Phys. Chem. Chem. Phys. **16** (45), 25054–25061 (2014).
33. J. Kopyra and H. Abdoul-Carime, J. Chem. Phys. **144**, 034306 (2016).
34. J. Kopyra, K. K. Kopyra, H. Abdoul-Carime and D. Branowska, J. Chem. Phys. **148** (23), 234301 (2018).
35. J. H. Hendricks, S. A. Lyapustina, H. L. d. Clercq, J. T. Snodgrass and K. H. Bowen, The Journal of Chemical Physics **104** (19), 7788-7791 (1996).
36. X. Li, K. H. Bowen, M. Haranczyk, R. A. Bachorz, K. Mazurkiewicz, J. Rak and M. Gutowski, J. Chem. Phys. **127** (17), 174309 (2007).
37. J. Schiedt, R. Weinkauf, D. M. Neumark and E. W. Schlag, Chem. Phys. **239**, 511–524 (1998).
38. J. Simons, J. Phys. Chem. A **112** (29), 6401–6511 (2008).
39. O. H. Crawford, Mol. Phys. **20** (4), 585–591 (1971).
40. R. A. Bachorz, W. Klopper, M. Gutowski, X. Li and K. H. Bowen, J. Chem. Phys. **129** (5), 054309 (2008).
41. A. Kunin and D. M. Neumark, Phys. Chem. Chem. Phys. **21** (14), 7239–7255 (2019).
42. X. Li, J. Chen and K. H. Bowen, J. Chem. Phys. **134** (7), 074304 (2011).
43. O. Dolgounitcheva, V. Zakrzewski and J. Ortiz, J. Chem. Phys. **134** (7), 074305 (2011).
44. E. Matthews, R. Cercola, G. Mensa-Bonsu, D. M. Neumark and C. E. Dessent, J. Chem. Phys. **148** (8), 084304 (2018).
45. S. B. King, M. A. Yandell, A. B. Stephansen and D. M. Neumark, J. Chem. Phys. **141** (22), 224310 (2014).
46. W.-L. Li, A. Kunin, E. Matthews, N. Yoshikawa, C. E. Dessent and D. M. Nuemark, J. Chem. Phys. **145** (4), 044319 (2016).
47. M. A. Yandell, S. B. King and D. M. Neumark, J. Am. Chem. Soc. **135** (6), 2128–2131 (2013).
48. S. B. King, M. A. Yandell and D. M. Neumark, Faraday Discuss. **163**, 59–72 (2013).
49. A. B. Stephansen, S. B. King, Y. Yokoi, Y. Minoshima, W.-L. Li, K. A., T. Takayanagi and D. N. Neumark, J. Chem. Phys. **143** (10), 104308 (2015).
50. A. Kunin, V. S. McGraw, K. G. Lunny and D. M. Neumark, J. Chem. Phys. **151** (15), 154304 (2019).
51. A. L. Kunin, W.-L.; Neumark, D. M., J. Chem. Phys. **149** (8), 084301 (2018).
52. M. Koga, M. Asplund and D. M. Neumark, J. Chem. Phys. **156**, 24302 (2022).
53. R. Cercola, E. Matthews and C. E. H. Dessent, Mol. Phys. **21**, 3001–3010 (2019).
54. K. O. Uleanya, R. Cercola, M. Nikolova, E. Matthews, N. G. K. Wong and C. E. Dessent, Molecules **25** (14), 3157 (2020).
55. K. O. Uleanya and C. E. Dessent, Phys. Chem. Chem. Phys. **23** (2), 1021–1030 (2021).
56. A. V. Davis, R. Wester, A. E. Bragg and D. M. Neumark, The Journal of Chemical Physics **118** (3), 999-1002 (2003).

57. A. E. Bragg, J. R. R. Verlet, A. Kammrath, O. Cheshnovsky and D. M. Neumark, Journal of the American Chemical Society **127** (43), 15283-15295 (2005).
58. W. Wiley and I. H. McLaren, Rev. Sci. Instrum. **26** (12), 1150–1157 (1955).
59. V. Dribinski, A. Ossadtchi, V. A. Mandelshtam and H. Reisler, Rev. Sci. Instrum. **73** (7), 2634–2642 (2002).
60. M. J. Frisch, G. W. Trucks, H. B. Schlegel, G. E. Scuseria, M. A. Robb, J. R. Cheeseman, G. Scalmani, V. Barone, G. A. Petersson, H. Nakatsuji, X. Li, M. Caricato, A. V. Marenich, J. Bloino, B. G. Janesko, R. Gomperts, B. Mennucci, H. P. Hratchian, J. V. Ortiz, A. F. Izmaylov, J. L. Sonnenberg, D. Williams-Young, F. Ding, F. Lipparini, F. Egidi, J. Goings, B. Peng, A. Petrone, T. Henderson, D. Ranasinghe, V. G. Zakrzewski, J. Gao, N. Rega, G. Zheng, W. Liang, M. Hada, M. Ehara, K. Toyota, R. Fukuda, J. Hasegawa, M. Ishida, T. Nakajima, Y. Honda, O. Kitao, H. Nakai, T. Vreven, K. Throssell, J. Montgomery, J. A., J. E. Peralta, F. Ogliaro, M. J. Bearpark, J. J. Heyd, E. N. Brothers, K. N. Kudin, V. N. Staroverov, T. A. Keith, R. Kobayashi, J. Normand, K. Raghavachari, A. P. Rendell, J. C. Burant, S. S. Iyengar, J. Tomasi, M. Cossi, J. M. Millam, M. Klene, C. Adamo, R. Cammi, J. W. Ochterski, R. L. Martin, K. Morokuma, O. Farkas, J. B. Foresman and D. J. Fox, *Gaussian 16, Rev. A.03*. (Gaussian, Inc.: Wallingford, CT, 2016).
61. K. A. Peterson, B. C. Shepler, D. Figgen and H. Stoll, J. Phys. Chem. A **110** (51), 13877–13883 (2006).
62. S. B. King, A. B. Stephansen, Y. Yokoi, M. A. Yandell, A. Kunin, Y. Takayanagi and D. M. Neumark, J. Chem. Phys. **143** (2), 024312 (2015).
63. A. Kunin, W.-L. Li and D. M. Neumark, J. Chem. Phys. **149** (8), 084301 (2018).
64. T. Baer, W. L. Hase and L. William, *Unimolecular reaction dynamics: theory and experiments*. (Oxford University Press on Demand, 1996).
65. R. G. Gilbert and S. C. Smith, *Theory of unimolecular and recomination reactions*. (Publishers' Business Services, 1990).
66. T. Beyer and D. Swinehard, Communications of the ACM **16** (6), 379 (1973).
67. S. E. Stein and B. Rabinovitch, J. Chem. Phys. **58** (6), 2438–2445 (1973).
68. A. Kunin, W.-L. Li and D. M. Neumark, Phys. Chem. Chem. Phys. **18**, 33226 (2016).
69. R. A. Bachorz, W. Klopper and M. Gutowski, The Journal of Chemical Physics **126** (8), 085101 (2007).

Chapter 5

UV Probe Measurements of Nucleobase Excited Iodide-Thymine Clusters

Megan Asplund, Alice Kunin, Katharine Lunny, Ying Jung Wu, Daniel Neumark

5.1 Abstract

Electron attachment dynamics are studied by time-resolved photoelectron spectroscopy (TRPES) of the iodide-thymine (I^-·T) binary cluster. Excitation of the cluster at 4.74 eV causes transfer from the halide to the nucleobase, facilitating the formation of valence bound (VB) anionic nucleobase species, as shown in previous experiments with 1.56 eV probe pulse. Utilization of a higher energy (3.16 eV) probe pulse replicates the dynamics associated with the VB state, but also permits measurement of more tightly bound anionic species, including major decay product I^- and anionic tautomers of thymine, which have been observed in one color PES studies and are predicted to have high stability. The rise time of dissociated I^- is found to be remarkably slow for I^-·T compared to similar clusters, which is incongruous with the rapid and complete decay of the VB anion. I^- signal rise is seen to be in reasonable agreement with the decay of a transient feature with vertical detachment energy (VDE) around 1.5 eV, tentatively assigned to anionic thymine tautomer R15. This suggests that although autodetachment is the primary the decay mechanism for the canonical VB anion, increased stability of the anion tautomer relative to the canonical anion decreases the dominance of autodetachment and permits the reformation of I^- as a competitive decay mechanism.

5.2 Introduction

Ultraviolet (UV) irradiation of genetic material DNA and RNA leads to strand breakages by a variety of mechanisms, including direct and indirect interactions between photon and strand. Theoretical treatment of these mechanisms indicates that indirect interactions account for ~60% of this damage,[1] as energy from a direct excitation can often be safely dissipated by efficient non adiabatic relaxation processes.[2-6] UV photons impinging on the aqueous cellular matrix can generate electrons, radicals, and ions, all of which can cause covalent bond cleavage upon interaction with the nucleic acid strand.[7, 8] A mechanism of particular interest is the attachment of low energy electrons, which has been shown to result in double and single strand breakages.[9] Theoretical treatment indicates that these electrons are able to attach efficiently to nucleobases, generating transient ionic species that cause fragmentation along the nucleic acid backbone.[8, 10, 11]

Dissociative electron attachment (DEA),[12-18] photoelectron spectroscopy (PES),[19-24] and Rydberg electron transfer[25-27] studies have provided a wealth of information about nucleobase anions. Valence bound (VB) ions are formed if the excess electron is accommodated by an unoccupied molecular orbital of the molecule. In nucleobases, the lowest unoccupied molecular orbital (LUMO) is generally a π^* orbital with anti-bonding type character. Population of this orbital results in puckering of the nucleobase ring relative to the neutral.

In addition to ion formation, low energy electron attachment can cause H abstraction as transient ions couple to σ^* and π^* states of the nucleobase.[12] H abstraction occurs primarily at NH sites and is possible even at electron energies lower than 1 eV, as evidenced by DEA studies.[14, 15, 17] H abstraction and reattachment has been invoked previously to explain the appearance of VB anion signals in PES spectra with vertical detachment energies (VDEs) much higher than predicted for the corresponding canonical nucleobase anions but in reasonable agreement with the VB anions of nucleobase tautomers.[19, 20, 28, 29] However, because these were one color PES studies, any

ionization or tautomerization takes place well before measurement of the anion and so dynamics or mechanisms associated with this process remain largely theoretical.

Time-resolved photoelectron spectroscopy (TRPES) of halide nucleobase clusters has been very effective in probing the dynamics of anion formation and interconversion following electron attachment.[30] Within this experimental setup, binary iodide nucleobase clusters are excited by a UV pulse to induce charge transfer from the halide to the nucleobase and resultant metastable anions are probed by a second laser pulse which detaches the excess electron. This method has been used to investigate electron accommodation dynamics of I^-·uracil,[31-33] I^-·adenine,[34] I^-·2-thiouracil,[35] I^-·4-thiouracil,[36] I^-· H_2O·uracil,[37, 38] and I^-·T.[32, 39] I^-·T was one of the first clusters characterized by TRPES and demonstrates VB ion formation dynamics in two excitation energy ranges, one near the cluster vertical detachment energy (VDE) and one well above the VDE. In previous work, dynamics are probed with a near-IR (1.56 eV) probe pulse capable of detaching anions of the canonical nucleobases. Subsequent measurements of I^-·uracil,[31-33] I^-·2-thiouracil,[35] I^-·4-thiouracil,[36] and I^-· H_2O·uracil[37, 38] have demonstrated that a UV probe pulse (3.16 eV) can provide key details of the mechanism following cluster excitation which cannot be obtained with the lower energy probe. However, the UV probe has not previously been used to characterize decay products of iodide-thymine (I^-·T).

Within the cluster, the iodide primarily serves to donate an excess electron to the nucleobase. However, the iodine cannot be considered a fully passive bystander; rather, it continues to participate in dynamics of the nucleobase after charge transfer, e.g. by impacting the stability of the dipole bound ion, as seen in chapter 4.[31, 39] In particular, our studies of iodide nucleobase clusters, in addition to photofragmentation studies by Dessent and coworkers, have shown that a major decay pathway of the valence bound anion is back electron transfer to iodine and the dissociation of reformed iodide.[30, 33, 40]

This paper builds on the work previously published on the I^-·T cluster[32, 39] by introducing a higher energy probe pulse capable of detaching electrons from more stable anionic forms and the key decay product I^-. We find that the dissociation of I^- is anomalously slow for the cluster I^-·T compared to similar clusters despite the cluster's short-lived VB ion, indicating the presence of some other intermediate state. TRPES measurements of the cluster also display intensity at a binding energy not easily assigned to any of the features described in previous experiments on I^-·T clusters. Based on its binding energy and dynamics, the signal is tentatively assigned to the VB ion of a stable tautomer. A possible tautomer formation mechanisms is also discussed.

5.3 Methods

The TRPEI experimental setup has been described elsewhere[41, 42] and is summarized here. Argon buffer gas flows over a reservoir of methyl iodide, volatilizing methyl iodide due to its high vapor pressure. The gas mixture then passes through a cartridge heated to 220° C that contains solid thymine before passing through an Even-Lavie pulsed valve operating at 500 Hz. The output of the valve undergoes a supersonic expansion to generate vibrationally cool molecules which are prone to cluster. The gaseous mixture is ionized by dissociative electron attachment to methyl iodide, leaving I^- clustered with the nucleobase. Anionic clusters are extracted perpendicularly to

a Wiley McLaren time of flight mass spectrometer,[43] and subsequently mass selected to isolate the species of interest in the interaction region.

The clusters interact with ultrafast UV laser pulses generated by a KM Griffin oscillator and KM Dragon amplifier. The output of the KM Dragon is 2mJ/pulse laser light at 1 kHz centered at 795 nm or 1.56 eV with a temporal duration of ~40 fs. The IR laser light passes through a 50/50 beam splitter, with half the light going to form the pump laser beam and half to form the probe laser beam. The light for the pump beam is frequency tripled by a series of BBO non-linear crystals with a half wave plate between to account for polarization rotation in the frequency doubling step. The resultant beam has an energy of 4.74 eV. The light for the probe beam may be used as is for 1.56 eV probe or may be frequency doubled by a BBO crystal to generate 3.16 eV UV light. The cross-correlation of the pump and probe beam is $\sigma \approx 85$ fs. A TTL pulse generated by the KM Dragon is used to trigger the ion electronics. Because the pulse valve is unstable running at 1 kHz, the TTL pulse frequency is halved to 500 Hz.

When the laser pulses interact with the anionic clusters, electrons are detached and detected by a phosphor screen coupled to chevron-stacked multichannel plates by a velocity map imaging(VMI) assembly. The phosphor screen is imaged by a CCD camera and the electron kinetic energy spectra are reconstructed using BASEX reverse Abel transform.[44]

5.4 Results

Figure 5.1 a shows the false color contour plot for time-resolved photoelectron spectra of $I^-\cdot T$ taken with 4.74 eV excitation and 3.16 eV probe. This plot and others in this paper are plotted in terms of binding energy eBE, which may be found from the directly measured photoelectron kineticenergy eKE by eBE=hν-eKE, where hν is the energy of the detaching laser pulse. A dominant feature, feature A, grows in slowly in intensity over a couple hundred ps. Feature A is centered at 3.06 eV electron binding energy, and is narrow and intense. We can assign this feature as atomic I^- resulting for the dissociation of the $I^-\cdot T$ cluster.

Figure 5.1 b shows the lower binding energy range . Several features are apparent in the plot, listed here by increasing electron binding energy. Feature B is a very short-lived signal with most of its intensity falling between 0.2 and 1 eV. The breadth of the feature is characteristic of a valence bound anion, with a VDE in agreement with theory prediction for the VB anion of thymine.[29] The characteristics of this feature are also in agreement with the VB anion signal seen in our previous measurements of $I^-\cdot T$.[32]

Feature C appears in the binding energy range of 1–2 eV. It appears to have two intensity maxima in time, the first at time delays <1 ps and the second at 10 ps or so. The dynamics of the first maximum are in excellent correspondence with that of Feature B, as discussed in Section IV, so it is likely that this is a tail of that feature rather than a contribution from a distinct signal. The assignment of feature C will be discussed in greater detail in Section 5.6.

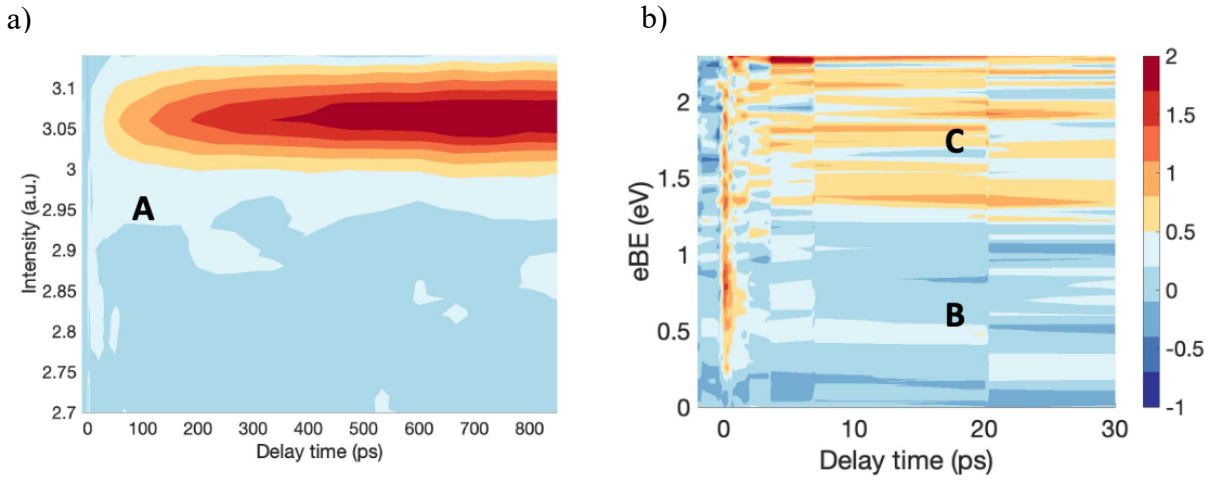

Figure 5.1: Contour plots of I^-·T cluster excited with 4.7 eV and probed with 3.16 eV plotted for higher (a) and lower (b) binding energies. The intensity of panel b is scaled up by a factor 20 to increase feature visibility.

The highest eBE feature, Feature D, lies in the region 3.12–3.16 eV. This signal is likely from cluster autodetachment, consistent with the results of other studies of iodide nucleobase clusters.[30, 35, 36] The signal shows intensity bleaching at short time delays, consistent with depletion of autodetaching electrons due to direct detachment from transient ion species.

Figure 5.2 shows a contour plot of the I^-·T cluster excited at 4.74 eV and probed at 1.56 eV. This measurement is taken with parameters equivalent to results previously measured,[30, 32, 39] but results of the same measurement are included here for ease of comparison. Feature B, assigned to the VB anion, is again evident in the binding energy range 0–1 eV. Overlapped energetically with Feature B is a weak band bound by 0.7–0.9 eV. Comparison to one-color PES shows that this signal comes from fluctuations in the direct detachment signal of the cluster by the excitation

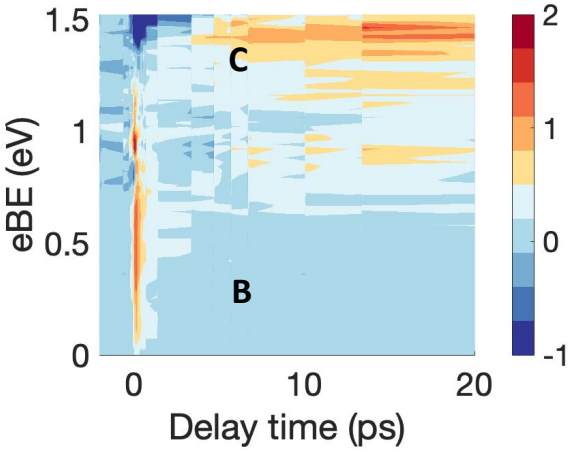

Figure 5.2: TRPE spectra of I^-·T cluster excited at 4.7 eV and probed at 1.56 eV

pulse.[32] Although this signal seems to evolve in time, the background noise level for is relatively high (S.I. Figure 1), so this is likely not a true time dependence.

At the highest binding energies (1.3–1.56 eV), the spectrum shows signal bleaching in the first ps as previously observed in the autodetachment signal of this cluster.[32] Based on the eBE range of signal C in Figure 5.1 b, the equivalent peak would overlap with both cluster direct detachment and autodetachment signal from relatively intense, single photon processes, leaving signal C somewhat obscured. Nevertheless, a low intensity signal C is visible in the binding energy region from 1-1.3 eV.

5.5 Analysis

The dynamics of the system may be investigated in greater detail by considering changes in the integrated intensity of each signal in time. The evolution of Feature A can be fitted by a simple exponential function for $t > 0$, giving a rise time constant of 124 $\pm$ 11 ps (Figure 5.3).

Features B and C evolve significantly within the first few ps following excitation, growing in rapidly before decaying over a ps or more. These signals may be fit using a convolution of the instrumental response function Gaussian and a sum of exponential decay terms, as in Equation 1.

$$I(t) = \frac{1}{\sigma_{cc}\sqrt{2\pi}} \exp\left(-\frac{t^2}{2\sigma_{CC}^2}\right) \cdot \begin{cases} I_0, & t < 0 \\ I_0 + \sum_i A_i \exp\left(-\frac{t}{\tau_i}\right) & t \geq 0 \end{cases} \quad \text{Eq. 1}$$

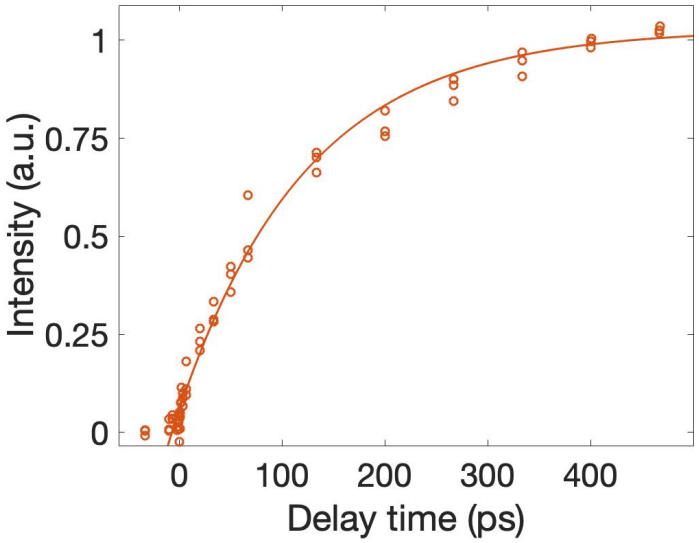

Figure 5.3: Integrated signal intensity from Feature A of I^-·T excited at 4.7 eV and probed at 3.16 eV. Integrated signal is shown as open circles, and the exponential fit (τ=124 ps) shown as a solid line .

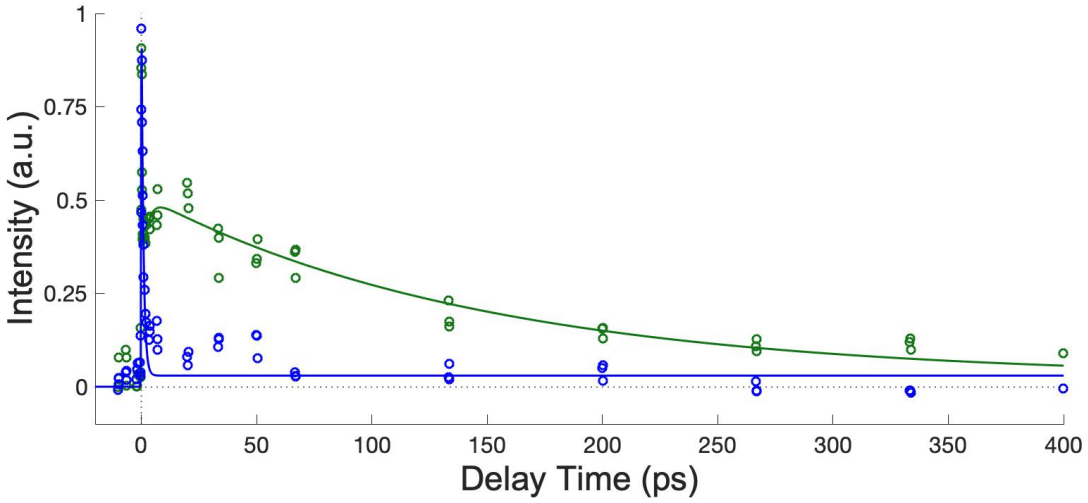

Figure 5.4: Integrated signal intensity of signal B (blue) and signal C (green) of $I^-{\cdot}T$ cluster excited at 4.7 eV and probed at 3.16 eV

In Eq. 1, I_0 is a constant signal offset, σ_{CC} is the cross-correlation of the pump and probe pulses, and A_i and τ_i are the intensity and time constant associated with the ith contribution to the time variant signal.

Figure 5.4 shows the evolution of features B and C in time, with open circles representing data points and the fits shown as solid lines. Table 1 gives the parameters for Equation 1 to reproduce the fit for features B and C. Feature B is well fit with by a cross-correlation limited rise and a single exponential decay of 860 fs. Feature C includes a sharp spike in intensity around t_0, with cross-correlation limited rise and rapid decay (τ_1=310 fs) of the signal. At later time delays, feature C shows a slower rise with τ_2=2.4 ps and a long decay time constant of τ_3=147 ps.

At very short time delays, feature B and C have very similar dynamics (Figure 5.5). From Figures 5.1 b and 5.2, the energy binding extent of feature B is unclear, and it is possible that intensity from this feature has binding energy as high at 1.6 eV. This would make the signal rather broad, but not out of keeping for the breadth of valence bound anion features in PES measurements of weakly solvated nucleobases.[24] It is reasonable to conclude that the initial spike in intensity from 1-1.6 eV is caused by Feature B rather than Feature C, and may be excluded from discussion Feature C specifically.

Table 1: Fitting parameters required to reproduce the fit of Feature B and Feature C in Figure 5.4

	eBE (eV)	τ_1	τ_2	τ_3	A_1	A_2	A_3
Feature B	0–1		0.86 ± 0.18		1		
Feature C	1–2	0.31 ± 0.15	2.4 ± 2.0	147 ± 39	0.68	-0.16	0.32

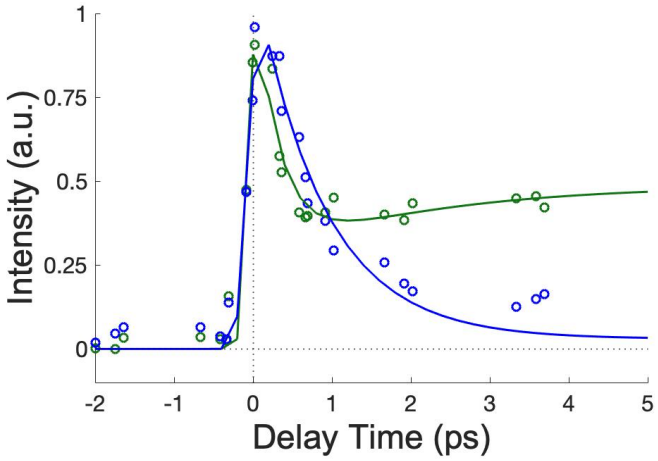

Figure 5.5: Integrated signal intensity of feature B (blue) and C (green) for I^-·T excited with 4.7 eV and probed with 3.16 eV at short time delays.

Figure 5.6 shows the relative evolution of signals B and D at the early times. As in previous measurements, there is excellent correspondence between the two signal intensities with the rise of B quite similar to the decay of C and vice versa.[32] This result is nicely replicated with the higher energy probe pulse.

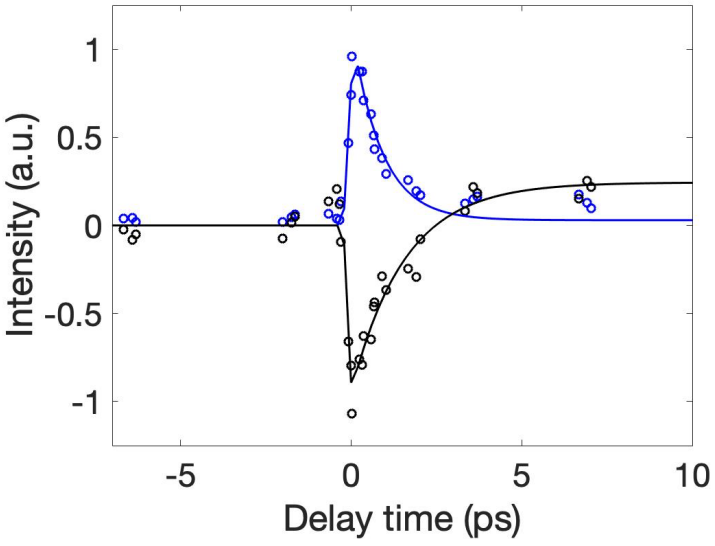

Figure 5.6: Integrated intensity of features B (blue) and D (black) for I^-·T excited with 4.7 eV and probed with 3.16 eV at early time delays

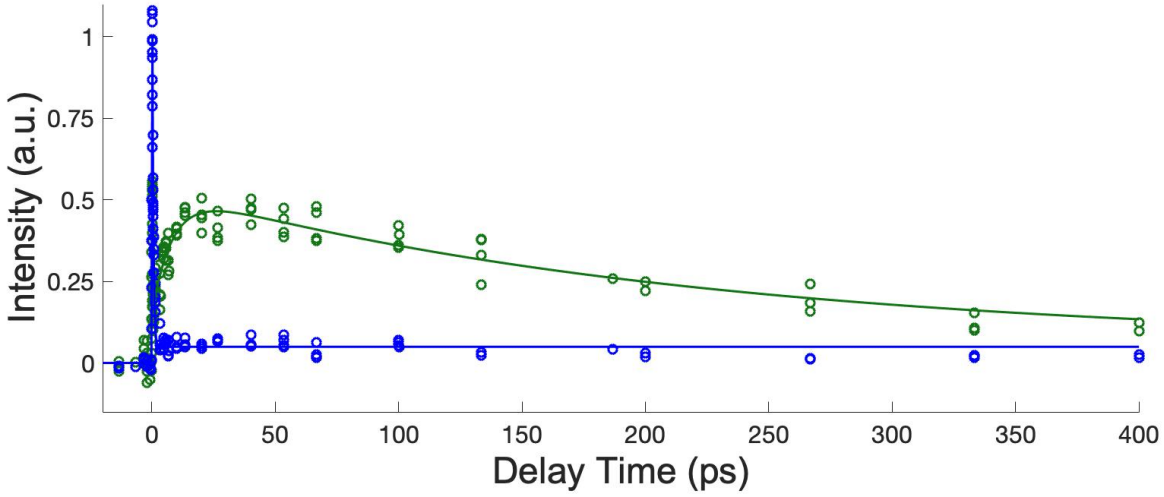

Figure 5.7: Integrated signal intensity from signal B and signal C excited with 4.7 eV and probed with 1.56 eV.

Equivalent features B and C are present in the spectra obtained with 1.56 eV probe, although overlap of the transient anion peaks with direct detachment and autodetachment features requires integration over a somewhat smaller eBE range. The evolution in time is very similar to what is measured with the higher energy probe, with cross-correlation limited rise and rapid decay of Feature B. The rise of feature C is somewhat slower in this case, and the relative uncertainty lower due to a higher density of data points near t_0. The decay time is within the fit uncertainty of what is determined with 3.16 eV probe.

5.6 Discussion

Feature A, representing the dissociation of the cluster to form free iodide, is fit by a rise time of τ = 124 ps. This is noticeably slower than the dissociation time scales observed in similar clusters, as seen in Table 3.[30, 35] For the other clusters, I^- rise is associated with iodide reformation by decay of the VB anion, with the time constant fitting I^- rise in reasonable agreement with one of the decay time constants of the VB signal. The $I^-\cdot T$ cluster is also characterized by a notably rapid and complete decay of the canonical valence bound anion, so it is somewhat surprising that iodide

Table 2: Fitting parameters required to reproduce the fit of Feature B and Feature C in Figure 5.7

	eBE (eV)	τ_1	τ_2	τ_3	A_1	A_2	A_3
Feature B	0 – 0.5		0.419 ± 0.037		1		
Feature C	1 – 1.3	0.068 ± 0.029	8.4 ± 2.1	226 ± 99	0.75	-0.20	0.25

Table 3: I^- signal rise times for various iodide nucleobase clusters excited at $\pi\pi^*$ resonant energies

Cluster	Excitation energy (eV)	I^- rise time
I^- uracil	4.7	36 ps
I^- 2-thiouracil	4.73	8 ps
I^- thymine	4.74	124 ps

dissociation time is so slow. This suggests that the canonical anion is unlikely to be the direct precursor to reformed iodide; instead, agreement between I^- time constant τ=124 ps and feature C decay τ_3=147 ps suggests that feature C is the precursor to I^- reformation.

The VDE of feature C from Figure 5.1 b (~1.5 eV) is in reasonable agreement with a previously reported rare tautomer of thymine, where a hydrogen is abstracted from N1 and attached to C5, which we will here refer to as R15. Computational results suggest R15 has a VDE of 1.25 eV and is stabilized by ~2 kcal/mol relative to the canonical tautomer.[29] A third relatively stable tautomer, called R35 in similar fashion, has a VDE of 2.25 eV and an adiabatic energy close to that of the canonical tautomer anion. One photon photoelectron spectra of thymine have previously shown evidence for anionic tautomer signal, with Li et al. measuring a spectrum dominated by signal from R35, with a low intensity secondary peak is centered at ~1.2 eV corresponding to R15.[20] The relative strength of VB signals from these tautomers has been attributed to the ionization method.[19, 20] In Li's measurement, thymine is volatilized by laser vaporization, which is likely to introduce excess energy which facilitates the tautomerization process. The comparatively

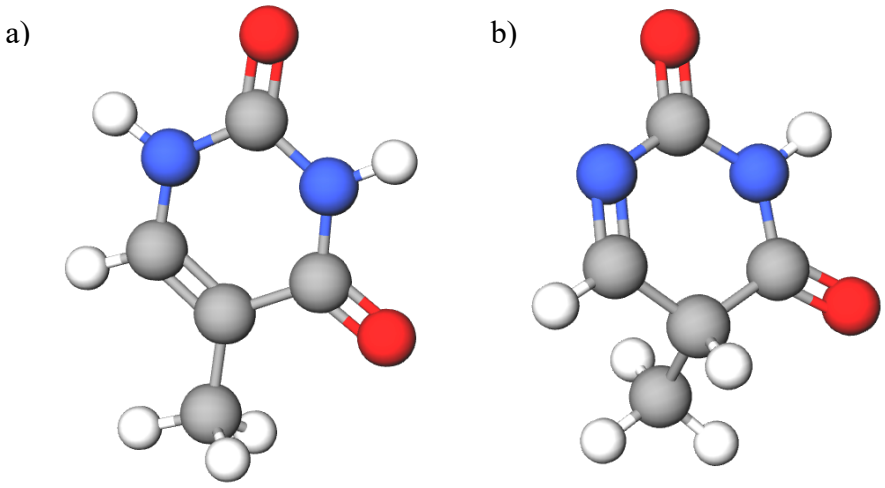

Figure 5.8: Structure of canonical thymine (a) and the R15 rare tauromer (b)

soft ionization method used in this work generates far more signal from the lower VDE canonical thymine anion. However, the appearance of signal C indicates that tautomerization may still be able to occur.

In the gas phase, tautomerization reactions of thymine anion are hindered due to a transition state barrier of about 40 kcal/mol; however, Mazurkiewicz et al identified an alternative mechanism to tautomerization in uracil and thymine.[20, 29] In this mechanism, the nucleobase is dehydrogenated by dissociative electron attachment and the tautomer is formed by hydrogen re-attachment.

$$T_{Rcan} + e \rightarrow T^{*-}_{N1H} \rightarrow [T-H]^{-} + H^{\cdot}$$

$$[T-H]^{-} + H^{\cdot} \rightarrow T^{-}_{R15}$$

Hydrogen attachment is predicted to be a barrierless reaction,[29] so hydrogen abstraction is the limiting step. Märk and coworkers have shown via dissociative electron attachment that H radical abstraction can occur with electron energies below 1 eV, including a noticeable shoulder in the T-H ion efficiency curve at 0.7 eV.[16, 17] If we assume that the attaching electron is directly excited into a scattering type state, it would have an energy of $h\nu_{pump} - VDE$ or ~0.7 eV, in reasonable agreement with a known resonance associated with H loss from NH bonds in thymine. It is unclear what the impact of the neutral iodine would be on this process, although it is likely that it would help to stabilize the abstracted H radical. It therefore seems reasonable to assume that this mechanism might take place, yielding the R15 tautomer. The rise in the corresponding feature is several picoseconds, lagging behind formation of the canonical valence bound anion. This is reasonable given the H rearrangement process that must take place for the signal to appear.

The VB signal from $I^{-}{\cdot}T_{canonical}$ is remarkable among the VB signals we have seen in that its decay is monoexponential and rapid. There is also an excellent correlation between the evolution of the VB signal and cluster autodetachment, indicating that autodetachment is a highly effective decay pathway for this nucleobase in particular. The autodetachment process itself need not be rapid, but the ~1 ps recovery of the bleached signal indicates that nearly all decay of VB signal associated with canonical thymine eventually results in autodetachment.

The rise and decay times of Signal C are noticeably slower than the feature B decay or the autodetachment signal recovery time. This suggests that autodetachment is likely not a major decay mechanism for this species. Instead, the decay time is within the fit uncertainty for the I^{-} rise. If the R15 tautomer decay is primarily by cluster dissociation, this suggests that the tautomer is stabilized with respect to autodetachment to the extent that I^{-} reformation is a competitive mechanism. This may perhaps by understood from the perspective of the relative stability of each tautomer anion. The canonical anion, which has a calculated energy near or even slightly above that of the canonical neutral, is able to readily couple from vibrational levels of the anion to vibrational levels of the neutral, facilitating thermionic emission of an electron. In contrast, the R15 tautomer is stabilized by a few kcal/mol, decreasing the ease with which the anion can couple to the neutral.

5.7 Conclusion

TRPES with 4.74 eV excitation and 3.16 eV probe has been applied to $I^-{\cdot}T$ in order to better understand decay mechanisms from the excited cluster. The slow appearance of I^- signal suggests temporally hindered reformation of iodide despite rapid decay of the VB anion of the canonical form of thymine. The appearance of a signal with VDE ~1.5 eV suggests tautomerization of thymine by electron attachment induced hydrogen abstraction. The decay time of this signal is in reasonable agreement with the rise time of dissociated I^-, suggesting that the tautomer ion may be the precursor for reformed iodide

5.8 Supplemental Material

Figure 5S.1 Time evolution of features B, C, and D (plotted in their respective panels) in addition to the direct detachment intensity fluctuations of the direct detachment peak (plot A), plotted without background subtraction. The error of the background signal level is shown as a translucent blue box plotted from a signal level of $\mu - 3 * \sigma_{background}$ to $\mu + 3 * \sigma_{background}$. Features B, C and D have noticeable signal levels above baseline noise, direct detachment fluctuations fall almost entirely within the noise level, suggesting that there is no meaningful evolution of this feature in time.

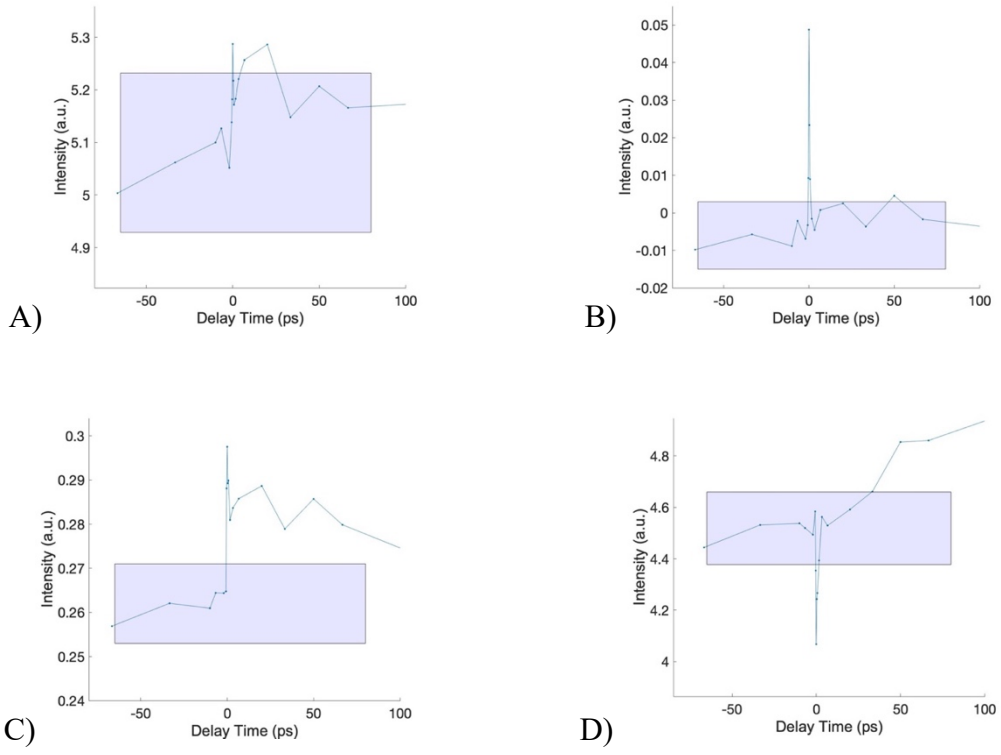

References

1. E. Alizadeh and L. Sanche, Chem. Rev. **112** (11), 5553–6214 (2012).
2. S. Matsika, J. Phys. Chem. A **108**, 7584–7590 (2004).
3. C. E. Crespo-Hernández, B. Cohen, P. M. Hare and B. Kohler, Chem. Rev. **104**, 1977–2020 (2004).
4. H. Yu, J. A. Sánchez-Rodríguez, M. Pollum, E. Crespo-Hernandez, S. Mai, P. Marquetand, L. Gonzalez and S. Ullrich, Phys. Chem. Chem. Phys. **18**, 20168–20176 (2016).
5. R. Improta, F. Santoro and L. Blancafor, Chem. Rev. **116** (6), 3540–3593 (2016).
6. M. Barbatti, A. J. A. Aquino, J. J. Szymczak and H. Lischka, Proc. Natl. Acad. Sci. U.S.A. **107** (50), 21453–21458 (2010).
7. J. Narayanan S J, D. Tripathi, P. Verma, A. Adhikary and A. K. Dutta, ACS Omega **8** (12), 10669-10689 (2023).
8. J. Simons, Acc. Chem. Res. **39**, 772–779 (2006).
9. B. Boudaïffa, P. Cloutier, D. Hunting, M. A. Huels and L. Sanche, Science **287**, 1658–1660 (1998).
10. R. Barrios, P. Skurski and J. Simons, J. Phys. Chem. B **106**, 7991–7994 (2002).
11. J. Berdys, I. Anuseiwicz, P. Skurski and J. Simons, J. Am. Chem. Soc **126**, 6441º6447 (2004).
12. P. Burrow, G. A. Gallup, A. M. Scheer, S. Denifl, S. Ptasinska, T. Mark and P. Scheier, J. Chem. Phys. **125** (12), 124310 (2006).
13. D. Huber, M. Beikircher, S. Denifl, F. Zappa, S. Matejcik, A. Bacher, V. Grill and T. D. Märk, J. Chem. Phys. **125**, 084304 (2006).
14. G. Hanel, B. Gstir, S. Denifl, P. Scheier, M. Probst, B. Farizon, M. Farizon, E. Illenberger and T. D. Märk, Phys. Rev. Lett. **90** (18) (2003).
15. S. Denifl, S. Ptasinska, M. Cingel, S. Matejcik, P. Scheier and T. D. Märk, Chem. Phys. Lett. **377**, 74–80 (2003).
16. S. Denifl, S. Ptasinska, M. Probst, J. Hrusak, P. Scheier and T. D. Märk, J. Phys. Chem. A **108** (31), 6562–6569 (2004).
17. S. Ptasinska, S. Denifl, B. Mròz, M. Probst, V. Grill, E. Illenberger, P. Scheier and T. D. Mark, J. Chem. Phys. **123**, 124302 (2005).
18. H. Abdoul-Carime, M. A. Huels and E. Illenberger, Eur. Phys. J. D **35**, 399–404 (2005).
19. R. A. Bachorz, W. Klopper, M. Gutowski, X. Li and K. H. Bowen, J. Chem. Phys. **129** (5), 054309 (2008).
20. X. Li, K. H. Bowen, M. Haranczyk, R. A. Bachorz, K. Mazurkiewicz, J. Rak and M. Gutowski, J. Chem. Phys. **127** (17), 174309 (2007).
21. X. Li, J. Chen and K. H. Bowen, J. Chem. Phys. **134** (7), 074304 (2011).
22. J. H. Hendricks, S. A. Lyapustina, H. L. d. Clercq, J. T. Snodgrass and K. H. Bowen, The Journal of Chemical Physics **104** (19), 7788-7791 (1996).
23. J. H. Hendricks, S. A. Lyapustina, H. L. de Clercq and K. H. Bowen, J. Chem. Phys. **108**, 8–11 (1998).
24. J. Schiedt, R. Weinkauf, D. M. Neumark and E. W. Schlag, Chem. Phys. **239**, 511–524 (1998).
25. C. Desfrançois, S. Carles and J. P. Schermann, Chem. Rev. **100** (11), 3943–3962 (2000).
26. C. Desfrançois, H. Abdoul-Carime and J. P. Schermann, J. Chem. Phys. **104**, 7792 (1996).
27. C. Desfrançois, V. Periquet, Y. Bouteiller and J. P. Schermann, J. Phys. Chem. **102**, 1274 (1998).

28. R. A. Bachorz, J. Rak and M. Gutowski, Phys. Chem. Chem. Phys. **7** (10), 2116–2125 (2005).
29. K. Mazurkiewicz, R. A. Bachorz, M. Gutowski and J. Rak, J. PHys. Chem. B **110** (48), 24696–24707 (2006).
30. A. Kunin and D. M. Neumark, Phys. Chem. Chem. Phys. **21** (14), 7239–7255 (2019).
31. S. B. King, M. A. Yandell, A. B. Stephansen and D. M. Neumark, J. Chem. Phys. **141** (22), 224310 (2014).
32. S. B. King, M. A. Yandell and D. M. Neumark, Faraday Discuss. **163**, 59–72 (2013).
33. W.-L. Li, A. Kunin, E. Matthews, N. Yoshikawa, C. E. Dessent and D. M. Nuemark, J. Chem. Phys. **145** (4), 044319 (2016).
34. A. B. Stephansen, S. B. King, Y. Yokoi, Y. Minoshima, W.-L. Li, K. A., T. Takayanagi and D. N. Neumark, J. Chem. Phys. **143** (10), 104308 (2015).
35. M. Koga, M. Asplund and D. M. Neumark, J. Chem. Phys. **156**, 24302 (2022).
36. M. Asplund, M. Koga, Y. J. Wu and D. M. Neumark, J. Chem. Phys. **160** (5) (2024).
37. A. Kunin, V. S. McGraw, K. G. Lunny and D. M. Neumark, J. Chem. Phys. **151** (15), 154304 (2019).
38. A. Kunin, W.-L. Li and D. M. Neumark, J. Chem. Phys. **149** (8), 084301 (2018).
39. S. B. King, A. B. Stephansen, Y. Yokoi, M. A. Yandell, A. Kunin, Y. Takayanagi and D. M. Neumark, J. Chem. Phys. **143** (2), 024312 (2015).
40. K. O. Uleanya and C. E. Dessent, Phys. Chem. Chem. Phys. **23** (2), 1021–1030 (2021).
41. A. V. Davis, R. Wester, A. E. Bragg and D. M. Neumark, The Journal of Chemical Physics **118** (3), 999-1002 (2003).
42. A. E. Bragg, J. R. R. Verlet, A. Kammrath, O. Cheshnovsky and D. M. Neumark, Journal of the American Chemical Society **127** (43), 15283-15295 (2005).
43. W. Wiley and I. H. McLaren, Rev. Sci. Instrum. **26** (12), 1150–1157 (1955).
44. V. Dribinski, A. Ossadtchi, V. A. Mandelshtam and H. Reisler, Rev. Sci. Instrum. **73** (7), 2634–2642 (2002).